Computations of Atmospheric Entry Gas Dynamics in Shock-tube Experiments

A DISSERTATION
SUBMITTED TO THE FACULTY OF THE GRADUATE SCHOOL
OF THE UNIVERSITY OF MINNESOTA
BY

Durgesh Chandel

IN PARTIAL FULFILLMENT OF THE REQUIREMENTS
FOR THE DEGREE OF
DOCTOR OF PHILOSOPHY

Advisor: Graham V. Candler

December, 2019

Acknowledgements

I am grateful to several people for their support during the course of this research.

First, I would like to thank my advisor, Prof. Graham Candler, who gave me the right opportunities, guidance and freedom to make this dissertation possible. The zeal and competency in his workstyle creates a naturally motivational research environment. His contributions in shaping me as a researcher are immeasurable. Thanks to Dr. Aaron Brandis, my mentor at NASA Ames Research Center; his careful attention to detail and experimental insight constantly bolstered my understanding and solution approach. Thanks to Prof. Thomas Schwartzentruber, Prof. Ellen Longmire and Prof. Peter Bruggeman for providing additional feedback as part of the graduate committee. I am also thankful to Dr. Ioannis Nompelis for his valuable critiques and suggestions throughout this project. Thanks to Dr. Heath Johnson for continuous support on code improvements and debugging.

The mentorship and guidance I received from my colleagues at NASA Ames Research Center, has been truly enriching. My interactions with Drs. Khalil Bensassi, Brett Cruden, Michael Barnhardt, Dinesh Prabhu, Jeffrey Hill, Joseph Schulz, Joseph Brock, Ethiraj Venkatapathy and David Saunders expanded my vision and helped in understanding several minor details in this project. Thanks to Dr. Michael Wright for periodic feedbacks and continued funding support as a project manager on this research.

My colleagues at Minnesota have been extremely helpful and encouraging. Special thanks to John Thome, John Reinert and Anthony Knutson for their constant friendly support. Thanks to Narendra Singh, Ross Chaudhry, Prakash Shrestha, Olivia Schroeder and Erik Torres for lending an ear in times of need. Thanks to all labmates and departmental colleagues for making my stay enjoyable. Finally, I would like to express my deep gratitude to my mom and dad, who gave their all to help me reach my dreams, and my younger brother Abhishek, for showing me things in a different light.

I am fortunate to have such inspirational and supportive mentors, friends and family. Thanks for being a part of my life.

This research was funded by Entry Systems Modeling (ESM) project at NASA Ames Research Center through contracts 80NSSC18K0211 and NNA15BB15C to Analytical Mechanics Associates Inc. Thanks to the computational support provided by Hyperion cluster at University of Minnesota and Pleiades supercomputer in NASA Advanced Supercomputing (NAS) division at NASA Ames Research Center. The views and conclusions contained herein are those of the authors and should not be interpreted as necessarily representing the official policies or endorsements, either expressed or implied, of the funding agencies or the U.S. Government.

To Mom & Dad

Abstract

A computational approach is developed to simulate high enthalpy shock propagation under strong nonequilibrium conditions, with application to atmospheric entry flows in shock tubes. Numerical simulations are performed for 6-11 km/s atmospheric entry shock experiments conducted in the Electric Arc Shock Tube (EAST) facility at NASA Ames Research Center. The simulation strategy developed here involves simplifications of the EAST facility and optimization of computational methods to make numerical calculations tractable. Shock tube flow evolution is mathematically represented by a system of time-varying, strongly hyperbolic partial differential equations (PDEs) with stiff source-terms. An 11-species weakly ionized air model is used to capture the real-gas behavior with reaction rates from Park (1990) and Huo (2015). Species mass- diffusion fluxes are calculated assuming a self-consistent effective binary diffusion (SCEBD) in conjunction with Gupta-Yos (1990) collision-integral data.

Starting from simple one-dimensional wave propagation problems, the computational modeling is systematically improved for two-dimensional axisymmetric simulations of EAST flow, pertinent to Earth and Titan entry conditions. The unsteady, linearized system of conservation laws is solved in a moving-frame of reference with active shock tracking to reduce the computational cost by three orders of magnitude relative to that of fixed-frame calculations on a uniform grid. This approach enables first-ever predictions of gas behavior at EAST test-section in a time-accurate yet computationally feasible manner.

Numerically computed shock-deceleration and post-shock electron number densities are compared against EAST measurments. CFD data qualitatively captures the nonequilibrium gas behavior observed in the experiments despite some discrepancies due to factors such as modeling assumptions, simplifications of the experimental process, limitations of gas physical and chemistry models under high-enthalpy strong nonequilibrium conditions, etc. Shock deceleration in CFD is about 40 to 100 times smaller and post-shock electron densities are lower than that measured in EAST. CFD data is further used to understand shock start-up process at different shock speeds. Useful quantities such as boundary layer thickness and growth rate, and radial variation of gas properties are also studied, these are crucial for radiative heating calculations but cannot be directly measured in the experiments.

Contents

List of Figures

List of Tables

Chapter 1

Introduction

1.1 Motivation

Spacecraft atmospheric entries occur at near-orbital or superorbital speeds, typically on the order of ten kilometers per second. Such high speeds result in extreme gas environments around the vehicle which makes the entry phase critical to safety. Depending upon the mission trajectory, entry speeds can be from 5 to 50 times faster than the local acoustic speed. Hence, the spacecraft reaches to an upstream location much before the acoustic flow-field information can, not leaving enough time for the flow to adjust itself. This leads to the formation of strong *shock waves* – the spacecraft as it moves, acts like a fast moving piston, compressing the surrounding gas into an extremely thin layer across which gas properties change drastically.

Shock waves convert the directed kinetic energy of the flow into random thermal motion. Atmospheric gases are rapidly heated within the shock layer, and various energy modes of gas molecules, such as translational, rotational, vibrational, electronic and electron modes, are excited to higher energy levels. Due to the rarefied conditions during initial entry trajectory, gas molecular collision rates are small; therefore, the excitation, exchange and relaxation processes between different energy modes occur over finite-times, similar to those of the flow convective time scales [3]. As a result, the shock-heated gas mixture contains energetically excited molecules, dissociated atoms, ions and free electrons, up to significant distances behind the shock front. The interaction of these highly reactive and radiative gas species with the spacecraft surface leads to large heat-flux and ablation rates. For instance, the Apollo Earth entry from Lunar return mission started at a speed of 11.2 km/s, from an altitude of about 120 km. The total specific enthalpy of the shock-heated air was approximately 60 MJ/kg, raising the gas temperature beyond 25,000 K and heat-shield surface temperature up to 2,500 K. Stagnation point peak-heating rates for 11-13 km/s Earth entry missions, such as Apollo, Stardust and Fire II, reached up to 1,400

W/cm^2 (see Ref. [4]) whereas the Galileo probe recorded up to 40,000 W/cm^2 during entry to Jupiter at 50 km/s [4]. The accumulated heat loads during a spacecraft entry, descent and landing (EDL) phase are large – the survival of the vehicle during entry relies heavily on the performance of its heat-shield. Future space missions require higher entry speeds in various planets, natural satellites and asteroids, increasing the demand for a detailed understanding of high-enthalpy flow physics over a range of atmospheric conditions.

A combined approach is usually adopted to understand atmospheric entry flow behavior using flight tests, ground-based experiments, and numerical computations. Flight testing and numerical analyses on space vehicles, such as Apollo [5–7], Stardust [8, 9], Hayabusa [10], have provided useful insight into entry aerothermodynamics and heat-shield material response. Organizations like NASA [11, 12], California Institute of Technology [13], CUBRC [14, 15], Von Karman Institute [16], JAXA [17], University of Oxford [18], University of Queensland [19], have developed a range of advanced high-enthalpy testing capabilities using shock tubes, shock tunnels, arc-jets, expansion tubes, etc., to replicate the extreme conditions during atmospheric entry. Recently, solar based entry heating facilities are developed at Sandia national laboratories [20] and Ecole Polytechnique Fédérale de Lausanne (EPFL) [21]. All these facilities help understanding specific aspects of entry flow physics but none of them can replicate real flight behavior in a complete manner. There is a large volume of experimental data available for a variety of missions but the interpretation of measured quantities must be complemented with high-fidelity numerical simulations and/or flight tests. The goal of the current research is to develop an efficient computational approach for time-accurate predictions of atmospheric entry flows in shock tubes.

Shock tube experiments are fundamental tools to study the shock-heated gas behavior and identify key thermochemical processes for numerical studies. The Electric-Arc Shock Tube (EAST) facility at NASA Ames Research Center consists of a 10.16 cm dia. shock tube and a 76 cm dia. shock tunnel, as shown in Fig. 1.1. Experiments in the blow-down type EAST shock tube are designed to study hot gas dynamics during entry to various planets and natural satellites, such as Earth, Mars, Titan, Venus, etc. [22–26]. High-speed shock waves in EAST are generated by creating a large pressure difference between an electrically heated driver gas and a relatively cold test gas, initially separated by a thin diaphragm. When the diaphragm is ruptured, a strong discontinuity propagates into the test gas, forming a shock wave and heating it to desired test conditions. A range of thermochemical excitation and relaxation processes is studied by analyzing the shocked gas behavior. As the shock propagates, its arrival-times are recorded at different axial locations (see details in Appendix A). This data is used to calculate the local shock speed and deceleration. The test-section is located about 8 m downstream of the diaphragm where the shocked gas is spectroscopically imaged in different wavelength regimes, ranging from

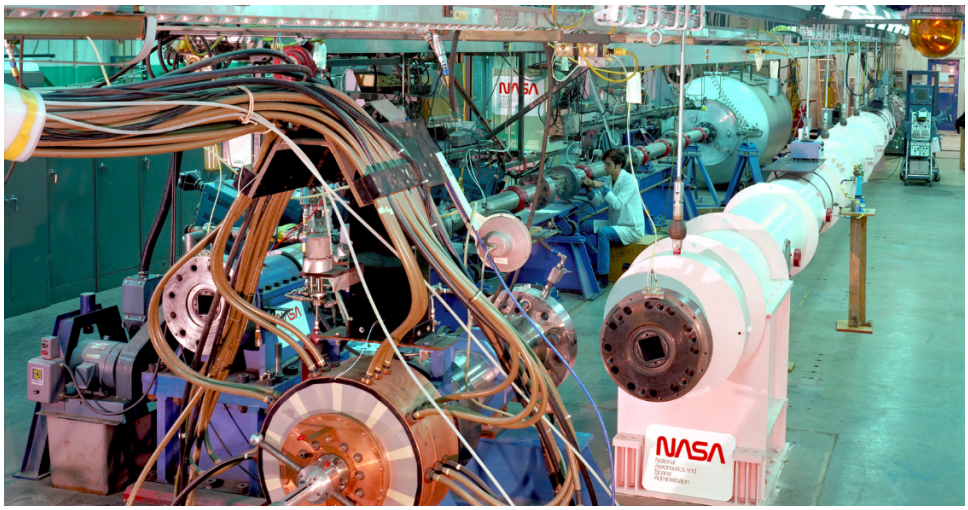

Figure 1.1: EAST facility at NASA Ames Reaserch Center; the shock-tube is on the left.

deep Vacuum Ultra Violet (VUV) to Infra Red (IR). Since each thermochemical process emits a unique thermal radiation, the spectroscopic data can be used to validate radiative heating rates and inform gas kinetic models in CFD. More details about the instrumentation, data collection and benchmarking process can be found in Refs. [22, 23, 27].

Numerical simulations of high enthalpy shock tube flows such as in EAST, are deceptively challenging. The flow geometry and initial conditions seem trivial but the multi-physics phenomena occuring over a huge range of length- and time-scales complicate the computational modeling. Several physical mechanisms observed in the shock tubes are merely an artifact of the experimental process but the test gas dynamics is significantly influenced by these shock-tube effects. For instance, the driver gas is heated by an electric-arc in a time-varying, three-dimensional manner. An accurate knowledge of driver gas properties is desired to set-up the initial conditions in CFD, which would require time-accurate solutions to complex magnetohydrodynamics (MHD) equations. As driver gas pressure is increased, the diaphragm starts expanding to initiate a rupturing mechanism which is a finite-time process involving three-dimensional fluid-structure interaction. During the diaphragm rupture, compression waves travel from the driver gas region into the test gas and coleasce together to form a shock wave. These start-up mechanisms introduce weak nonuniformities in the flow which govern the shock start-up speed, its planarity, and formation of any secondary shocks. At most test conditions, shock start-up effects are significantly diminished after 10-20 tube diameters of shock travel, beyond which a fully developed, almost planar shock wave propagates towards the test-section. EAST test-section is located about 80 tube diameters downstream the primary diaphragm, hence, the influence of start-up

mechanisms on gas behavior at the test section can be considered as minimal.

Some shock-tube effects sustain during the entire experimental process. For example, as the shock front propagates downstream, it grows a boundary layer at the walls which interacts with the high-speed core flow and causes a deceleration and curving of the shock front. Another source of shock deceleration is the energy loss due to thermal radiation which is an important factor at speeds greater than 13 km/s [24–27]. Since shock strength is directly related to the shock speed, the test gas at increasing axial distances from the diaphragm is shocked with decreasing shock strength, resulting in spatially varying post-shock gas state. Hence, the post-shock gas properties away from the shock front can be significantly different from corresponding equilibrium values just behind the shock. In addition, the boundary layer region is subsonic relative to the shock, therefore, any flow perturbations in this region can amplify and feed back into the upstream flow to distort the shock structure. Apart from this, factors such as irregularities in the tube-inner geometery due to instrumental probes and their role in flow transition to turbulence, the interaction of reflected expansion waves with the shock front, the background radiation due to impurities and wall-ablation products, etc., can have minor effects on test gas kinetics and radiation. Some of these processes were studied in an isolated manner by the researchers in the past [28–31].

Modeling all shock-tube effects together is difficult. EAST measurements show a continuous deceleration of the shock along the tube, and the post-shock electron number densities increase behind the shock [32], suggesting that the impact of wall boundary layer on the inviscid core flow is prominent and persistent throughout the shock travel. Computational efforts have been made for meaningful interpretation, validation and benchmarking of EAST experiments [24–27, 32, 33], but post-shock nonequilibrium behavior could not be understood completely. Full-facility based computations of EAST flow are required for a complete understanding of shock tube data. Recent efforts have been focusing on capturing wall-boundary layer effects on test gas dynamics.

1.2 Challenges and previous research

Hot gases in EAST exhibit multiscale flow physics at high temperatures. The rarefied gas in the freestream goes through a strong compression across the shock and then it expands behind the shock front. The driver gas, initially kept at high pressure, expands as the shock wave is formed and propagates downstream. Hence, the local mean-free path, λ, changes vastly in various regions of the shock-tube flow, and the Knudsen number, $Kn = \frac{\lambda}{\lambda_\infty}$, varies from the free-molecular to continuum flow regimes. Regions with large viscous gradients are confined to the shock front and boundary layer within a thickness of several millimeters whereas the shock front travels approximately 8 m along the tube to reach at the test-

section. Shocked gas slows down in the near-wall region which causes a deceleration and curving of the shock-front and introduces non-uniformities in the inviscid core flow. Post-shock gas temperatures are well above the gas dissociation and ionization temperatures. For typical Earth entry conditions, the electron-impact excitation and ionization processes are significant, resulting into an avalanche of free electrons in the shock-heated gas mixture.

From a computational perspective, capturing all dominant processes and resolving key length- and time-scales is challenging. The high-speed propagation of shock waves on the computational grid is prone to numerical errors due to factors such as poorly resolved gradients across the shock and the boundary layer, the shock mis-alignment relative to the grid, the amplification and feed back of numerical stabilities in the subsonic boundary layer region, etc. Numerical predictions are also susceptible to the choice of the shock capturing method, the flux reconstruction scheme, and the distribution of the numerical dissipation in different regions of the shock tube flow. Kitamura et al. [34, 35] showed that the numerical flux functions must be shock-stable, and the boundary layer must be accurately resolved for multi-dimensional, viscous, hypersonic problems. Liou and Steffen [36] proposed a new family of flux-splitting schemes using advection upstream splitting method (AUSM) for accurate predictions on supersonic blunt body problems. Wada and Liou [37] adjusted the numerical dissipation in Van-Leer-type flux-vector splitting to remove the numerical overshoot behind steady shock waves, and produced exact solutions for systems with a single, fast moving contact discontinuity. Liou [38] and MacCormack [39] showed that the shock induced multi-dimensional anomalies, such as, the carbuncle effect, can completely distort the numerically predicted shock structure when numerical schemes are not chosen carefully.

Early attempts to solve the 2D axisymmetric EAST flow were started by McCorkle et al. [40] using the data parallel line-relaxation (DPLR) CFD solver [41]. The numerical shock front could only be propagated until 0.3 m along the tube, after which numerical oscillations polluted the CFD solution. Yee et al. [42] and Kotov et al. [43] investigated the behavior of high-order shock-capturing schemes in strongly reactive flows with fast moving discontinuities. They observed that the numerically predicted wave speeds strongly depended on the order of accuracy and dissipative nature of the flux-reconstruction method. Also, the numerical errors increased drastically with increasing stiffness in reaction-kinetics. It was concluded that obtaining a stable solution across strong discontinuities requires higher-order shock-capturing methods with a gradient-based filtering of the numerical dissipation for retaining the small scale flow-features in the boundary layer, while dissipating the numerical errors near the shock front. Based on these findings, Kotov et al. [44] computed a representative EAST flow in a 8.5 m long, 2D channel using high-order numerical schemes with well-balanced numerical dissipation. A simplified form of the governing equations was

employed using Strang-splitting and a one-temperature chemistry model to obtain a stable but computationally expensive solution (about 7 days run-time on 2000 CPUs) for 2 m of shock travel. The numerical solutions showed a dependence on the computational grid and the flux reconstruction scheme. They also predicted significant amplitudes of Tollmien-Schilichting (TS) type instabilities near the shock tube walls. Higdon et al. [45] used Direct Simulation Monte Carlo (DSMC) methods to compute the flow physics for 10.28 km/s shock in air. This fluid dynamic data used as an input to NASA's Non-EQuilibrium AIr Radiation (NEQAIR) code predicted a radiation behavior similar to the test, however, several areas of improvements were identified.

Recently, Bensassi and Brandis [46] attempted 2D axisymmetric calculations for 10 km/s Earth entry experiments. They used second-order accurate backward-difference time-integration schemes along with state-of-the-art gas thermochemical models in the COOLFluiD [47] flow solver. These full-tube simulations took about 4 months on 500 CPU cores on NASA Pleiades[1] cluster. However, the predictions at the test-section were dominated by numerical instabilities, possibly due to an improper handing of the axisymmetric source terms; the simulation strategy needed further investigation. Thus, the EAST flow solutions obtained so far have suffered from numerical anomalies, and turned out to be computationally expensive. Additionally, the computational models for nonequilibrium gas chemistry, and species physical and molecular transport properties, etc., are still developing [48–55], therefore, the flow physics could not be modeled with desired level of accuracy.

In the absence of physics-based predictions, EAST experimental data have been interpreted using blunt-body flow simulations such as flow over a cylinder [27, 33]. The flow conditions are adjusted for desired shock speeds and a large nose radius is used to have large stand-off distance which can fully accomodate the width of the shock layer in the experiments. Gas properties at the stagnation streamline are compared against those at the shock tube centerline. However, the evolution of gas dynamics is fundamentally different between these flow configurations. The shocked gas behind the steady bow-shock in blunt-body flow quickly attains a thermochemical equilibrium whereas fast moving shock waves in EAST are decelerated by the boundary layer, leading to a strongly nonequilibrium gas behavior. Thus, the numerical predictions of EAST flow with simplified blunt-body approach are not appropriate in the conditions where nonequilibrium effects dominate, such as for Earth entry speeds of 8-10 km/s [32]. Sharma et al. [56] used a one-dimensional approach to simulate the wall-bounded shock propagation in EAST while the mass, momentum and energy losses in the boundary layer were modeled by including additional source/sink terms in the governing equations. They matched the shock-deceleration observed in EAST by using scaling parameters on boundary layer growth rate. However, different test conditions

[1]Pleiades cluster system is a part of NASA's High-End Computing Capability (HECC) at NASA Ames Research Center. (`https://www.nas.nasa.gov/hecc/resources/pleiades.html`.)

required different scaling parameters to match the shock-deceleration and the simulation approach could not be made predictive.

Since the spectrograph capture a radially integrated gas radiation, the test measurements include the effects of the deceleration and curving of the shock in the boundary layer region. Hence, it is important to quantify the effects of wall boundary layer for an accurate interpretation of the test data. Prior to the present work, computation of the full EAST shock tube flow with high-temperature chemistry and complete real-gas effects remained an open problem.

1.3 Scope of current research

This dissertation presents a novel approach for time-accurate computations of shock tube flow physics at atmospheric entry conditions. Current analyses are focused on high-speed entry missions in nitrogen rich atmospheres, such as Earth (79% by mole) and Titan (94% by mole). Numerical simulations are performed for 6-11 km/s shocks in pure nitrogen and air, where EAST experimental data is available [1, 32]. CFD predictions are used in conjunction with shock tube data to enhance the understanding of key flow physics.

Shock tube experiments are multiphysics processes. The simulation strategy developed here involves simplifications of the experimental facility and optimization of computational methods to make numerical calculations tractable. The blow-down type shock tube in EAST is modeled assuming a homogeneous arc-heating of the driver gas with an instantaneous, fully uniform diaphragm-rupturing process, and a smooth, two-dimensional, axi-symmetric tube geometry with constant cross-sectional area. EAST flow is mathematically represented by a system of time-varying, strongly hyperbolic partial differential equations (PDEs) with stiff source-terms.

A systematic approach is adopted to devise and optimize the simulation strategy for intricate flow dynamics in EAST. Challenges in EAST simulations can be viewed in three major aspects, 1) time-accurate numerical propagation of strong shock and its interaction with subsonic boundary layer, 2) computational modeling of high-temperature gas properties, and 3) numerical error-control and computational cost. Previous researchers focused on using high-order shock-capturing methods on relatively coarse computational grids to save the computational cost but the numerical solutions predicted wrong wave speeds, suffered from spurious oscillations, and did not obtain numerical convergence. The low-dissipation high-order numerics was prone to numerical oscillations, whereas dissipative methods predicted wrong wave speeds. Based on these findings, the current approach focuses on using first-order time-integration methods and second-order low-dissipation flux schemes while the time- and space-discretization steps are chosen such that the regions of strong flow

gradients are fully resolved.

First, the behavior of unsteady, strong hyperbolic systems is thoroughly assessed using model problems, such as one-dimensional convection-diffusion, shock propagation in perfect gas, and flow complexities, such as reaction kinetics, multi-dimensionality, and visocus shock-boundary layer interactions, etc., are slowly introduced to finally simulate the 2D axisymmetric real-gas flow at EAST conditions. State-of-the-art physical and kinetic models are used to capture real gas behavior. Early evolution of the shock is thoroughly assessed using various simulation approaches and numerical flux-reconstruction and time-integration schemes. Conservation equations are solved, 1) in a coupled vs. decoupled manner, 2) using a fixed computational grid vs. moving grid, and 3) in the laboratory-frame vs. shock-frame of reference. The numerical and physical modeling, and the grid-cell and time-step size requirements are optimized for numerically converged, shock-stable solutions. This analysis helped devise a new simulation approach to solve the strongly coupled EAST flow equations in shock-frame of reference using active shock-tracking and grid adaptations. Numerically computed wave speeds are validated against analytical values, and the post-shock gas properties are compared with chemical-equilibrium based predictions. It is found that the linearized implicit system of equations, when solved approximately using Jacobi-type iterations, requires a tighter convergence criterion on the residuals for shock propagation problems than in the case of steady shocks.

With this understanding, two-dimensional axisymmetric EAST flow simulations are performed for a dissociating 5-species air model using FMDP/DPLR [57] and preconditioned GMRes implicit methods [58, 59]. Numerical solutions show convergence on wave-speeds and key flow variables, and capture the curving and deceleration of the shock front due to viscous interaction with the boundary layer. Next, the EAST flow is solved in a more accurate and complete manner by including gas ionization processes. This poses additional challenges in terms of numerical stability and computational cost. Park's [60] 11-species weakly ionized air model is used to consider dominant chemical reactions in the flow. The electron-impact excitation and ionization processes are significant at these conditions. Free electrons travel at much higher speeds than heavy particles and collisions between the two ionize heavy particles to release additional electrons moving at relatively lower speeds. This leads to an abundance of free-electrons in the post-shock gas region which can accumulate near the cold tube walls ($T_{wall} = 300$ K), to be absorbed by ionic species in the gas mixture. A catalytic neutralization of ions is imposed through the numerical boundary condition at the tube walls to model this process. This also helps in controlling the numerical instabilities in the near-wall region. Numerically converged, stable and thermodynamically consistent solutions are obtained for a range of air and nitrogen shock experiments conducted in EAST [27, 32, 61]. Post-shock flow predictions are compared with experimental data to assess the

performance of current CFD modeling and identify the scope of future improvements.

The mathematical equations and gas models describing the shock tube flow are described in the following chapter. Numerical methods and simulation approach is discussed in Chapter 3. The analysis on one-dimensional shock propagation problems is covered in Chapter 4, followed by shock-tube flow predictions in Chapter 5 and 6, for air and nitrogen shocks, respectively. Main conclusions are summarized in Chapter 7 along with the scope of future research.

Chapter 2

Mathematical Formulation

This chapter describes the governing equations and constitutive relations applicable to atmospheric entry flows in EAST shock tube.

2.1 The conservation equations

The focus of current work is on 6-11 km/s shock experiments in nitrogen and air. The test gas is considered at low pressure, rarefied conditions (i.e., $P_\infty = 0.2$ Torr, $\rho_\infty \approx 10^{-4}$ kg/m^3), corresponding to the peak-stagnation heating altitude during Apollo's Lunar return trajectory.

The freestream molecular mean free path, λ_∞, is ≈ 0.3 mm, and the shock layer region is typically about $10\lambda_\infty$ wide. Based on the local Knudsen number ($Kn \equiv \frac{\lambda_\infty}{\lambda}$), different regions of the shock tube flow exhibit behavior ranging from the free-molecular to continuum flow regimes. The Knudsen number based on the shock width, W_s, is $Kn \equiv \frac{\lambda_\infty}{W_s} \approx 0.1$, which is in the continuum to free-molecular flow transition regime (i.e., $0.01 < Kn < 10$). A continuum hypothesis is not valid within the shock, however, the total mass, momentum and energy of the flow are conserved across the shock. Hence, the flow conservation equations can be applied in the pre- and post-shock gas regions assuming a continuum flow behavior.

EAST flow is mathematically represented by the compressible Navier-Stokes equations for conservation of mass, momentum and energy. For 6-11 km/s shock speeds considered in this dissertation, total specific enthalpy of the shock-heated gas, h_0, reaches up to 18-60 MJ/kg. Such high enthalpy conditions result in extreme gas temperatures and gas internal-energy modes are highly excited. A two-temperature (TT_v) approach is used to account for different energy modes present in the gas mixture with the assumption that the translational-rotational, and the vibrational-electronic-electron energy modes are in equilibrium with each other, at temperatures T and T_v respectively. The latter is based on Gnoffo et al. [62] where the energy of free electrons is equilibrated with the vibrational-

electronic modes of the heavy particles during electron-impact excitation and ionization processes. Two separate equations are solved for the conservation of total- and internal-energy of the gas mixture. Gas radiation mechanisms are important at high speeds, however, their contribution to the total heat-flux becomes significant only for shock speeds greater than 13 km/s [33]. Hence, for simplicity the radiative source terms are ignored at current flow conditions.

For a chemically reacting gaseous mixture of ns species, the governing equations can be written as,

$$\frac{\partial \rho_s}{\partial t} + \frac{\partial (\rho_s u_j)}{\partial x_j} - \frac{\partial (\rho_s v_{sj})}{\partial x_j} = \dot{w}_s \quad (s = 1 \text{ to ns}) \tag{2.1}$$

$$\frac{\partial (\rho u_j)}{\partial t} + \frac{\partial (\rho u_i u_j + p\delta_{ij})}{\partial x_j} - \frac{\partial (\tau_{ij})}{\partial x_j} = 0 \tag{2.2}$$

$$\frac{\partial E_{v,el}}{\partial t} + \frac{\partial ((E_{v,el} + p_e)\ u_j)}{\partial x_j} + \frac{\partial q_{vj}}{\partial x_j} - \frac{\partial}{\partial x_j} \sum_{s=1}^{ns} (\rho_s (e_{v,el})_s v_{sj}) = \dot{w}_{v,el} \tag{2.3}$$

$$\frac{\partial E}{\partial t} + \frac{\partial ((E + p) u_j)}{\partial x_j} + \frac{\partial (q_j + q_{vj})}{\partial x_j} - \frac{\partial (\tau_{ij} u_j)}{\partial x_j} - \frac{\partial}{\partial x_j} \sum_{s=1}^{ns} (\rho_s h_s v_{sj}) = 0 \tag{2.4}$$

Here u_i is the component of velocity in the i^{th} direction, ρ is total density, and v_{sj} is the diffusive velocity of s^{th} species at face j. The variables $\rho_s, c_s, w_s, h_s, (e_{v,el})_s$ represent the density, mass fraction, chemical source terms, enthalpy per unit mass and vibrational-electronic-electron energy per unit mass for the s^{th} species. The shear-stress tensor is $\tau_{ij} = 2\mu S_{ij} - \frac{2}{3}\mu S_{kk}\delta_{ij}$ and S_{ij} is the symmetric part of the velocity-gradient tensor. The total energy of the gas mixture is E and total vibrational-electronic-electron energy is $E_{v,el}$. The source-term for the gas internal-energy, $\dot{w}_{v,el}$, is modeled based on Gnoffo et al. [62],

as described in Eq. 2.5.

$$\dot{w}_{v,el} = \underbrace{-u_j \frac{\partial p_e}{\partial x_j}}_{1} + \underbrace{\sum_{s=1}^{ns} \rho_s \frac{(e_{v,el})_s^* - (e_{v,el})_s}{<\tau_s>}}_{2} + \underbrace{\sum_{s \neq e} \dot{w}_s (e_{v,el})_s}_{3} + \underbrace{3\rho_e \bar{R}(T - T_v) \sum_{s \neq e} \frac{v_{e,s}}{M_s}}_{4} - \underbrace{f_{eii} \sum_{s=ions} \dot{n}_{e,s} \hat{I}_s}_{5} \tag{2.5}$$

here $\dot{n}_{e,s}$ is the molar rate of ionization and $\hat{I}_s$ is the first ionization energy of s^{th} species; f_{eii} is a tunable parameter. This formulation for $\dot{w}_{v,el}$ includes the contributions of 1) the work done on electrons by an electric field induced by the electron pressure gradient, 2) the energy exchange between vibrational-electronic and translational modes, and 3) the change in vibrational-electronic energy due to species depletion or production; here p_e is the electron pressure, $(e_{v,el})_s^*$ is the species vibrational-electronic energy at chemical equilibrium conditions, and $<\tau_s>$ is the average relaxation time between gas thermal and internal energy modes. The last two terms on the right hand side of Eq. 2.5, represent 4) the energy exchange due to elastic collisions between electrons and heavy particles, and 5) the loss in the translational energy of free electrons due to electron-impact ionization reactions, respectively. These mechanisms are important in weakly ionized flow at EAST test conditions. As a starting step, the air shock simulations are performed by considering terms (1)-(3) on the right hand side of Eq.2.5. The flow solver is then improved to include all five terms in the definition of $\dot{w}_{v,el}$, which is used for nitrogen shock simulations. A value of $f_{eii} = 1$ corresponds to the assumption that all the monoatomic species participating in the electron-impact ionization are ionized from their ground energy states – this leads to an over-estimation of the loss in electron energy since the shock-heated gas contains significant amounts of energetically excited atoms. Hence, the value of f_{eii} is chosen between 0 to 1. A value of $f_{eii} = 0.28$ is used for nitrogen shocks, based on the experimental data match obtained in FIRE-II Earth entry simulations performed at NASA Ames.

2.2 Constitutive relations

The Navier-Stokes equations described above are solved together with the equation of state,

$$p = \rho R T \tag{2.6}$$

here R is the specific gas constant for reacting gas mixture. The total vibrational-electronic-electron energy ($E_{v,el}$) of the gas mixture can be expressed as,

$$E_{v,el} = \rho e_{v,el} = \sum_{s \neq e} \rho_s (e_{v,el})_s + \rho_e C_{ve} T_v. \tag{2.7}$$

and the total energy, E, is,

$$E = \frac{1}{2}\rho u_i u_i + \sum_{s \neq e} \rho_s C_{vs} T + \sum_{s \neq e} \rho_s (e_{v,el})_s + \rho_e C_{ve} T_v + \sum_{s \neq e} \rho_s h_s^\circ \tag{2.8}$$

in this formulation, h_s° is the enthalpy of formation for s^{th} species and C_{vs} is the specific heat at constant volume. The gas mixture is assumed to behave like a newtonian-fluid, hence, the shear-stress tensor can be written as,

$$\tau_{ij} = 2\mu S_{ij} - \frac{2}{3}\mu S_{kk}\delta_{ij} \tag{2.9}$$

S_{ij} is the symmetric part of the velocity-gradient tensor, μ is dynamic viscosity. Gas total heat flux vector, q_j, is modeled using Fourier's law,

$$q_j = -\kappa \frac{\partial T}{\partial x_j} \tag{2.10}$$

here κ is thermal conductivity. The internal-energy heat flux, q_{vj}, is formulated based on Gupta-Yos model [48].

2.3 Gas physical and chemistry models

The flow behavior in EAST is significantly different from the ideal gas assumptions. Due to the high enthalpy conditions, gas molecules are energetically excited, dissociated and ionized. The thermal and molecular transport properties of this highly reactive mixture are a strong function of gas thermochemical state. State-of-the-art models are used to capture these high-temperature effects. The internal energies of species are taken from the NASA Lewis curve fits [63, 64] and molecular transport properties are calculated with collision-integral models by Gupta et al. [48]. Species mass-diffusion fluxes are modeled using the Self-Consistent Effective Binary Diffusion (SCEBD) model with small electron-mass correction, based on Ref. [49].

Post-shock electron number densities reported in EAST experiments [32] are quite high, i.e., $\mathcal{O}(10^{16})$ per cm^3. This indicates a partially ionized gas state with degree of ionization

ranging from 7-15%. An 11-species weakly ionized air model (i.e., N_2, O_2, NO, N, O, N_2^+, O_2^+, NO^+, N^+, O^+ and e^-) is used to represent all dominant species in the reacting gas mixture behind high-speed air shocks. The reaction kinetics in nitrogen shocks is modeled using a subset of air chemistry model, i.e., by allowing the formation of species N_2, N_2^+, N, N^+ and e^- only, in the test gas. The driver gas is helium in all cases. Chemical kinetics are modeled using Park's reaction rates [2] based on experimental curve fits. Table A.2 in Appendix A describes the reaction rate parameters based on Arrhenius law, with forward reaction-rate constant defined as, $k_{f,r} = A_{f,r}T^{\eta}exp(\frac{-\theta}{T})$ where $A_{f,r}$ is the collision factor and θ is the characteristic temperature for that reaction.

The post-shock electron number densities reported in EAST experiments [32] are quite high (i.e., $\mathcal{O}(10^{16})$ per cm^3) and the shocked gas is in a partially ionized state with the degree of ionization ranging from 7-15%. The electron-impact ionization (EII) of dissociated N and O atoms is expected to be significant, hence, the rates of these reactions are taken from a recent calculation by Huo et al. [50, 65]. Since the thermal energy of the electrons is at T_v, it should be used as the governing temperature for EII rates. However, this implementation causes numerical instabilities, and an effective temperature similar to that for the dissociation reactions, i.e., $\sqrt{TT_v}$, is used for numerically stable behavior in air shocks. The flow solver is improved subsequently, and nitrogen shock simulations are performed by using T_v as the governing temperature for the electron-impact ionization reactions.

2.4 The Finite Volume Formulation

The conservation equations in Sec. 2.1 are in the divergence law form. In the vector notation, these can be written as,

$$\frac{\partial U}{\partial t} + \boldsymbol{\nabla} \cdot \vec{F} = \dot{W} \tag{2.11}$$

here U is the vector of conserved variables which define the gas state, and F is the flux vector. In order to compute the flow evolution over time, the rate of change in U is integrated within an arbitrary volume V.

$$\int_V \frac{\partial U}{\partial t} dv = -\int_V \boldsymbol{\nabla} \cdot \vec{F} dv \tag{2.12}$$

This can be further simplified by using the Divergence Theorem as follows. Here $\bar{U}$ is

the the volume-averaged state vector and S is the surface of volume V.

$$\frac{\partial \bar{U}}{\partial t} = -\frac{1}{V}\oint_S \vec{F}\cdot\hat{n}ds \tag{2.13}$$

For the finite-volume cells with faces, the surface integration is equivalent to the summation over all faces.

$$\frac{\partial \bar{U}}{\partial t} = -\frac{1}{V}\sum_{faces}(\vec{F}\cdot\hat{n})S \tag{2.14}$$

here S is the cell-face area and $\hat{n}$ is the outward pointing unit normal vector associated with each face. The numerical fluxes can be decomposed into the convective (inviscid) and diffusive (viscous) parts as $\vec{F} = \vec{F}_{inv} + \vec{F}_{vis}$. For simplicity, the notation from here onwards is changed to F for F_{inv}, and F_ν for F_{vis}, respectively.

The finite volume formulation for the conservation laws in a chemically reacting gas mixture with ns species, can be written as,

$$\frac{\partial U}{\partial t} + \frac{\partial F_j}{\partial x_j} = \frac{\partial F_{\nu j}}{\partial x_j} + \dot{W} \tag{2.15}$$

where

$$U = \begin{bmatrix} \rho_1 \\ \rho_2 \\ . \\ . \\ \rho_{ns} \\ \rho u_i \\ E_{v,el} \\ E \end{bmatrix}, \quad F_j = \begin{bmatrix} \rho_1 u_j \\ \rho_2 u_j \\ . \\ . \\ \rho_{ns} u_j \\ \rho u_i u_j + p\delta_{ij} \\ (E_{v,el} + p_e)\ u_j \\ (E+p)u_j \end{bmatrix}, \quad F_{\nu j} = \begin{bmatrix} \rho_1 v_{1j} \\ \rho_2 v_{2j} \\ . \\ . \\ \rho_{ns} v_{ns} \\ \tau_{ij} \\ \sum_{ns}\rho_s v_{sj}(e_{v,el})_s - {q_{v,el}}_j \\ \tau_{ij}u_i - q_j - (q_{v,el})_j + \sum_{ns}\rho_s v_{sj} h_s \end{bmatrix} \quad \dot{W} = \begin{bmatrix} \dot{w}_1 \\ \dot{w}_2 \\ . \\ . \\ \dot{w}_{ns} \\ 0 \\ \dot{w}_{v,el} \\ 0 \end{bmatrix} \tag{2.16}$$

here U is the vector of conserved variables, F_j and $F_{\nu j}$ are the Cartesian components of the convective and viscous flux vectors respectively and $\dot{W}$ is the vector of source terms.

The linearized system of governing equations is solved using full-matrix data parallel (FMDP) [59] or data parallel line-relaxation (DPLR) implicit time-integration method. Due to the high speed shock motion, the inviscid flow information convects in a highly directional manner, therefore, convective fluxes are computed using Modified Steger-Warming (MSW) flux-vector splitting [66]. The diffusion fluxes of mass, momentum and energy depend on

the local flow gradients; these are first computed at the cell-centers and then interpolated at the cell-faces using 2^{nd} order accurate Monotonic Upwind Scehmes for Conservation Laws (MUSCL) [67]. More details on the implementation of these methods can be found in Refs. [68] and [57].

The numerical fluxes and the chemical source terms at the future time level are evaluated using a linearization about the known gas state at current timestep. The first-order accurate evaluation of the inviscid split fluxes at the future time level using their Jacobian ($F_j'^{n+1} = F'^{n}_j + \left(\frac{\partial F'}{\partial U}\right)^n_j (U^{n+1} - U^n)$) is as follows:

$$F_j'^{n+1} = A'^{n}_{+j}(U^n_L + \delta U^n_L) + A'^{n}_{-j}(U^n_R + \delta U^n_R) \tag{2.17}$$

where U is the vector of conserved variables, F'_j is the surface-normal inviscid flux and A'_{+j}, A'_{-j} are the flux Jacobians at the j^{th} face. U_L and U_R are gas state vectors to the left- and right- of the surface j respectively. For a second-order accurate formulation, the vectors U_L and U_R are calculated using a variable extrapolation method (See more details in Refs. [57, 69]).

Similarly, the viscous fluxes are approximated as $F_\nu'^{n+1} = F_\nu'^{n} + \delta F_\nu'^{n}$, where $\delta F_\nu'^{n}$ is assumed to be a function of the spatial derivatives of the vector of primitive variables V. The implicit approximation to the viscous fluxes can be written as:

$$\delta F'_\nu = M' \frac{\partial}{\partial \eta} \delta V \tag{2.18}$$

where M' is the matrix operating on $\frac{\partial}{\partial \eta}\delta V$ to obtain the approximate $\delta F'_\nu$. A transformation is used to map from δV to δU such that $\delta V = N\ \delta U$, and the matrix N is absorbed in the construction of the implicit operator. The final form of the iterates for the FMDP point-relaxation method becomes:

do $k = 1,\ kmax$

$$\delta {U_i}^{(k)} + \frac{\Delta t}{V_i} \sum_{f \in \text{faces}} \left[A_+ \delta {U_i}^{(k)}\right]_f S_f = \Delta {U_i}^n - \sum_{f \in \text{faces}} \left[A_- \delta {U_o}^{(k-1)}\right]_f S_f \quad \text{with} \quad \delta U_i = {U_i}^{n+1} - {U_i}^n \tag{2.19}$$

end do

$$\delta {U_i}^{n+1} = \delta {U_i}^{kmax} \tag{2.20}$$

Eq. 2.19 follows the notation of Nompelis et al. [57], where quantities with the subscript i correspond to i^{th} cell in which the value of the flux is being evaluated. The subscript o corresponds to a neighboring cell, f is a face surrounding the cell i, and A_+, A_- correspond to the incoming and outgoing Jacobians of the total flux assuming an outward-pointing normal by convention. The superscript n corresponds to the timestep level and k is the sub-iteration index in the relaxation process. ΔU_i^n is the change in the gas state U within a time-step Δt due to the explicit operator. The maximum number of these sub-iterations is controlled by a parameter $kmax$, which for the unsteady flows directly controls the accuracy of the predicted state at the next time-level. The DPLR (data parallel line-relaxation) method computes the implicit change in the solution by solving the matrix system exactly along one chosen direction (preferably the direction of the strongest gradients, such as the wall-normal direction in wall-bounded flows) and using an iterative point-relaxation approach in other flow directions as described in Eq. 2.19.

Chapter 3

Numerical Modeling

The numerical set-up and computational approach for EAST simulations are presented here. Several aspects of the numerical modeling and their implementation in the solver framework are modified to accurately solve the EAST problem with feasible computational effort.

3.1 Computational domain

For current flow conditions, the freestream molecular mean free path, λ_∞, is about 0.3 mm, and a typical Navier-Stokes predicted shock wave is expected to be approximately $10\lambda_\infty$ wide. The flow-through time based on the shock speed (i.e., the time taken by the shock wave to travel across the full tube-length) is $\mathcal{O}(10^{-3})$ s. The experiment is stopped once the shocked gas has completely passed beyond the test-section. EAST spectroscopic data [32] show that the shock-heated gas region is contained within a $10 - 20$ cm ($\approx\ 350 - 750\lambda_\infty$) distance behind the shock front. This information of the flow-field is leveraged to optimize computational grid requirements. Only a small portion of the tube containing hot gases is modeled in the simulations, and the grid-cell sizes are set to properly resolve the shock front. The computational grid is 0.7 m long, consisting of a 4 cm ($\approx 150\lambda_\infty$) wide uniformly refined region near the shock with a cell-size of 10 μm (i.e., 20-30 cells per λ_∞) in the axial direction. The boundaries of this refined region are named as $\mathrm{x_{left}}$ and $\mathrm{x_{right}}$ respectively, beyond which the grid is geometrically stretched on both sides. The diaphragm is located at $x = 0$ and the left domain boundary is at $x = -\ 0.6$ m. Numerical simulations are started just after the diaphragm burst. The shock front starts propagating from $x = 0$ at time $t = 0$, when the highly refined region extends from $x = 0$ to $x = 4$ cm. The radial dimension spans from $r = 0$ at the centerline to $r = 5.08$ cm at the tube surface.

The subsonic boundary layer near the shock tube walls introduces a feedback mechanism in the flow. Any acoustic disturbances in the boundary layer can travel both upstream and downstream of the shock, interact with it, and if these subsonic purturbations inter-

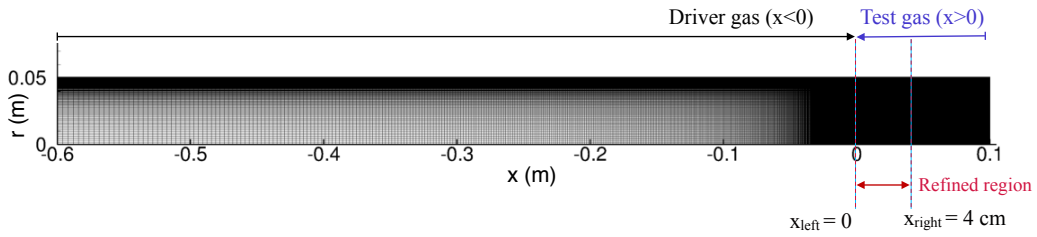

Figure 3.1: The 2D axisymmetric grid (6000×300 cells) used for EAST simulations; r = 0 is the shock tube centerline, r = 5.08 cm represents the wall

act with the boundary layer, they can grow significantly, distorting and/or breaking the shock structure completely. For this reason, the flow field in the near-wall region must be accurately resolved to capture the strong viscous interactions. The radial cell-size at the wall is taken as $\Delta r = 1\ \mu m$ to ensure the dimensionless wall-spacing, r^+, being less than 1. An appropriate grid stretching is applied in the region away from the wall, with 300 total cells in the radial direction. The total 2D axisymmetric grid size is 1.8 million cells (6000×300). With this grid design, the computational domain covers a 0.6 m long region behind the shock front whereas the region of action is only ≈ 0.2 m long. Hence, the regions of strong gradients are completely included in the numerical simulations. This is done to ensure that the numerical solution captures all important viscous interactions in the flow. The choice of total length of the computational domain being 0.7 m, which is about 10% of the total tube length (8 m), is flexible and can be further extended or reduced for different flow conditions, as long as it covers the shocked gas region entirely.

3.2 Modeling assumptions and initial conditions

In EAST experiments, helium is used as the driver gas to achieve high shock speeds without any chemical contamination of test gas. However, the existing energy accounting in the US3D solver requires non-zero vibrational-electronic energy throughout the domain. Thus, a trace amount (0.001 % by mass) of N_2 is introduced in the driver gas to avoid singular behavior of the solver, without any adverse effects on solution accuracy. Additionally, the arc heating process of the driver gas is complicated and an accurate modeling of the driver gas properties is beyond the scope of this analysis. Therefore, an instantaneous heating of the driver gas is assumed to the jump conditions required for desired shock speed. For simplicity, it is assumed that the diaphragm is fully open as soon as the fluid dynamic simulation starts. At the 6-11 km/s shock speeds considered in this work, the effects of radiative cooling and wall-ablation effects can be ignored.

The flow field is initialized with the driver gas in the region $x < 0$ and test gas in $x \geq 0$

Table 3.1: Initial Conditions

Location	Composition (by mole)	p (Pa)	ρ (kg/m^3)	T (K)
Driver gas	99.999% He + 0.001% N_2	13.7×10^6	1.105	6000
Test gas	Nitrogen, or Air (79% N_2 + 21% O_2)	26.8	3.082×10^{-4}	300

with the properties as indicated in Table 6.1.

3.3 Moving frame of reference

Strong shock waves in EAST travel about 8 m to arrive at the test section – solving this flow-field in the laboratory frame of reference would require a 8 m long grid refined sufficiently to capture the gradients in the boundary layer and across the shock front as it travels along the tube. For air shocks, a total of 17 equations (12 species mass-conservation equations, 3 momentum-conservation equations and 2 energy equations) have to be solved in each cell. Based on current grid cell-size requirements at the shock, modeling the full shock tube with a uniform grid would need about 240 million cells. An alternative approach would be to use adaptive mesh refinement in the regions of sharp gradients, but the required mesh adaptation frequency would be high due to the high-speed motion of the shock front with respect to the initial grid.

With this realization, the system of conservation equations is solved in two ways; in a fixed laboratory-frame of reference, and a frame of reference moving with the shock. In the latter, the whole computational domain is moved at a constant speed, which is the *equilibrium* shock speed in one-dimensional shock simulations at the same conditions. A constant speed is used to avoid any spurious acceleration in the flow due to the acceleration of moving-frame itself. The moving-frame is numerically implemented by adding a constant speed, u_f, to the entire flow-field, i.e., the domain interior and all boundaries. The governing equations for moving-frame calculations stay the same as described in Chapter 2, except that the gas velocity is changed from u to $u + u_f$.

Moving-frame approach enables for solving the flow only in a small region containing the shocked gas; the grid size requirements are cut by 130 times as compared to an axially uniform 8 m long grid. The implementation of moving-frame approach benefits in two ways: 1) the relative motion of the shock front within the grid is much slower, resulting in a more stable and accurate evolution of the flow and numerical residuals converge faster. and 2) the total grid size requirement is significantly reduced due to the limited motion of the shock wave in the grid, rather than having to discretize the entire facility to capture the full shock propagation. The boundary conditions are appropriately modified for the fixed-frame versus moving-frame calculations, described in next section.

3.4 Boundary conditions

Since the shock moves rapidly, the temperature of shock tube walls can be assumed to stay constant during the experiment. An isothermal wall boundary condition is employed with catalytic neutralization of all ionized species hitting at tube walls, i.e., the ionic species mass-fractions are made zero while remaining species in the gas mixture are adjusted based on the recombination of ions into neutral species. Thus, the elemental mass conservation is maintained near the wall. This is a realistic model for the current case of a cold wall (T_{wall} = 300K) and helps in stabilizing the numerical solution. The lower boundary in Fig. 4.1 represents the centerline of the tube (r = 0). A symmetry boundary condition is used here.

The shock-heated gas moves from left to right in the fixed laboratory-frame of reference, whereas in a reference frame moving with the shock, it travels from right to left. The boundary conditions are chosen accordingly, as shown in Fig. 3.2. A supersonic inflow and outflow condition is applied on the left and right domain boundaries respectively, for fixed-frame calculations. In the moving-frame set-up, the right domain boundary is modeled to allow a supersonic inflow of the freestream air through a Dirichlet boundary condition and the gas mixture exits from the left boundary through a zero-gradient Neumann boundary condition. The domain interior and all boundaries move at a constant speed, u_f, described in previous section. A no-slip boundary condition is used at the walls, that means the gas in the computational cell next to the wall moves at hypersonic speeds in moving-frame calculations.The gas state is accurately calculated based on gas velocities in the moving-frame.

Since the computational domain represents only a small portion of the shock tube, the assumption of zero gradients at left boundary does not stay valid once the expansion waves formed in the driver gas start exiting through this boundary and numerical errors due to these weak non-zero gradients can accumulate for long integration. One-dimensional shock tube studies are performed to quantify these effects.

3.5 Shock tracking

The implementation of a variable resolution grid requires only a small portion of the shock tube to be modeled. However, the shock front also moves relative to the computational grid. This is because just after the diaphragm burst, when the shock is still forming, all the energy available from the driver gas immediately excites the translational energy mode, leading to significantly larger shock speeds, and a state of strong nonequilibrium behind the shock. Subsequently, the internal energy modes present in the system start extracting energy from

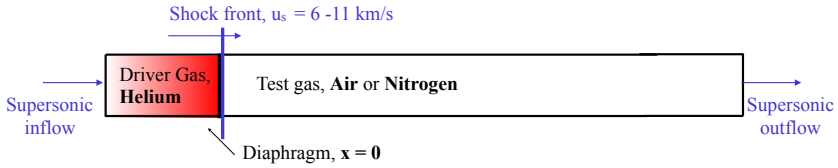

(a) Fixed-frame of reference

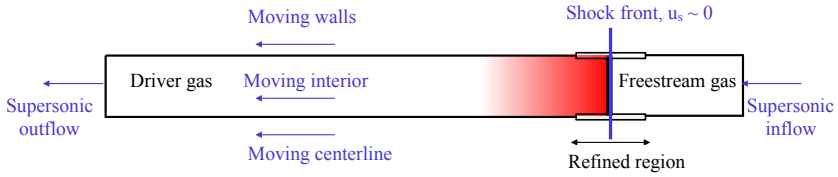

(b) Moving-frame of reference

Figure 3.2: Boundary conditions for EAST simulations

the translational mode, evolving towards a quasi-steady state. This mechanism along with the interaction of the shock with the boundary layer that is growing at the walls, leads to a deceleration of the shock front. As a result, in the frame of reference moving at a constant, near-equilibrium shock speed, the shock first moves a certain distance upstream in the grid, and then travels downstream based on its local relative speed with respect to the frame of reference. This requires a periodic mesh-adaptation and numerical interpolation based on the shock motion, which itself is prone to numerical errors and instabilities. The length and grid resolution of the highly refined region of the computational domain that tracks the shock in the moving frame of reference must be carefully chosen for a well-resolved flow field calculation.

For current calculations, a 4 cm wide ($\approx 150\lambda_\infty$), uniformly-refined region is used to track the shock. The shock front is detected at the computational cell where a 10% pressure-rise from the upstream value is observed. The motion of the shock within this region is tracked periodically, and mesh-adaptation is employed based on the location of the shock relative to the boundaries i.e., x_{left} or x_{right}). If the shock front is found within $0.2-0.5$ cm of either of the boundaries, the computational grid is translated in the axial direction such that a minimum of 2 cm wide nonequilibrium region behind the shock front would be contained within this window of high grid-cell resolution for next 0.5-1.0 m of shock travel. At this point, the numerical solution from the original grid is interpolated to the newly translated grid and the simulations are continued for further shock propagation. These grid-translation and numerical-interpolation steps are performed periodically such that the interpolated flow solution has less than 0.5% differences in key flow variables relative to the solution obtained on original grid.

The numerical set-up described here is used to understand the behavior of one-dimensional wave propagation problems presented in next chapter. This analysis is useful to optimize the numerics for two-dimensional axisymmetric EAST flow simulations.

Chapter 4

One-dimensional shock propagation

This chapter focuses on one-dimensional fast moving shocks. Simple test cases are used to assess the performance of conventionally used numerical methods in hypersonic flows. Starting with the model convection-diffusion equation, computations are performed to simulate high-speed shock propagation in perfect gas and reacting gas conditions. The learning from these test cases is used to optimize the computational approach for two-dimensional axisymmetric simulations. Various aspects of this new approach are validated against analytical solutions.

4.1 Sample problems

The analysis is started with the simplest wave-propagation problem, i.e., the convection-diffusion equation, where a scalar discontinuity propagates in a medium at a constant speed. This is referred to as Case 1. Since the analytical solution is known for this case, the performance of different numerical methods can be accurately assessed. Based on the findings from the model problem, one-dimensional shock tube flow is simulated assuming perfect gas behavior. These are referred to as Case 2(a) and 2(b), with shock speeds of 1 km/s and $\approx$ 10 km/s, respectively. Finally, the reacting flow simulations are performed for 10 km/s air shock, corresponding to EAST conditions. As a starting step, only molecular exchange and dissociation processes are considered in the reaction kinetics while ionization reactions are ignored. The gas mixture consists of helium and 5-species dissociating air (i.e., He, N_2, O_2, NO, N and O). NASA Lewis fits [63][64] are used to compute gas thermodynamic properties and species internal-energy. This is referred to as Case 3.

These simulations use a uniform, highly resolved grid ($\Delta x = 10\ \mu m$, i.e., $\approx$ 32 cells per λ_∞) with first-order accurate discretization methods for time and space. The flow conservation equations are solved in a laboratory fixed-frame of reference. Various time-integration and flux-computation schemes are used to understand the behavior of the numerical solu-

Table 4.1: Summary of Numerics

Flux schemes	Time integration methods
MSW[70],[71]	Explicit; Euler 1st order
KEC[72]	Explicit; Runge-Kutta 2nd order
-	Implicit; Central 2nd order
-	Implicit; FMDP[73] 1st order

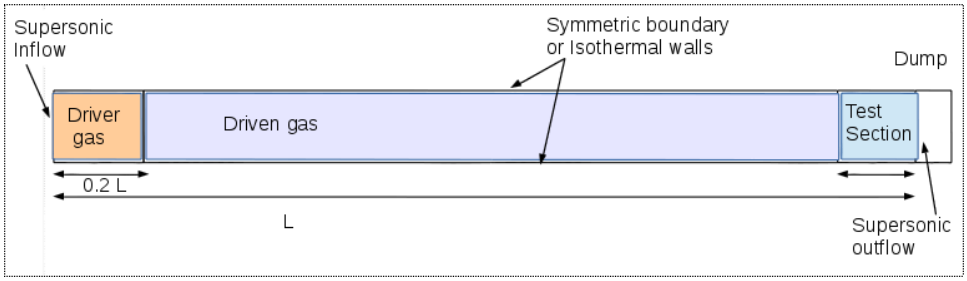

Figure 4.1: Boundary Conditions

tion. A snapshot of the numerics employed is shown in Table 4.1. Numerical simulations are performed using different combinations of these flux-schemes and time-integration methods.

An overview of the computational domain for Cases 2(a), 2(b) and 3, is shown in Fig. 4.1. Here, L represents the length of the computational domain, taken as 1 m. Since one-dimensional shock propagates at a constant speed, the post-shock properties stay constant; therefore, simulating only the first 1 m of shock propagation is sufficient for current purposes. The driver gas section is 0.2 m long. The dump region after the test-section is irrelevant and is excluded in our simulations.

4.1.1 Convection-Diffusion problem

As discussed earlier, the model advection-diffusion equation is solved to understand the behavior of unsteady, hyperbolic systems. The one-dimensional form of the model equation is as follows:

$$\frac{\partial u}{\partial t} + c\frac{\partial u}{\partial x} = \nu\frac{\partial^2 u}{\partial x^2} \tag{4.1}$$

where u is gas velocity, c is wave speed and ν is the kinematic viscosity.

An initial disturbance in scalar quantity, u, is advected and diffused across a 1 m long uniform grid with cell-size $\Delta x = 0.01$ m. The disturbance moves with a constant wave speed $c = 1$ m/s in air with kinematic viscosity $\nu = 10^{-4}$ m^2/s. A low value of wave speed is chosen to accurately demonstrate the performance of numerical methods with relatively coarse grid cells and time step sizes. The one-dimensional wave propagation is solved using

explicit and implicit time-integration schemes and the numerical solution is analyzed after $t = 0.5$ s. The CFL number is defined as $\frac{c\Delta t}{\Delta x}$.

Discretized System of Equations

The Eq. 4.1 is discretized using an upwinding scheme for convective fluxes and a central scheme for diffusive fluxes with Euler time-integration. The discretized form of equations using 1^{st} order spatial and temporal accuracy is given below.

$$\frac{u_i^{n+1} - u_i^n}{\Delta t} + c\frac{u_i^n - u_{i-1}^n}{\Delta x} = \nu\frac{u_{i+1}^n - 2u_i^n + u_{i-1}^n}{\Delta x^2} \tag{4.2}$$

Where u_i^n, is the value of gas-velocity u at the i^{th} node after n^{th} time-step. By defining $\alpha = c\frac{\Delta t}{\Delta x}$ and $\beta = \nu\frac{\Delta t}{\Delta x^2}$; and the linear system of equation can be re-written as follows,

$$u_i^{n+1} - u_i^n = -\alpha(u_i^n - u_{i-1}^n) + \beta(u_{i+1}^n - 2u_i^n + u_{i-1}^n) \tag{4.3}$$

The solution at i^{th} node and $(n+1)^{\text{th}}$ time-step can be obtained by $u_i^{n+1} = u_i^n + \delta u_i^n$, where δu_i^n can be solved in three different ways named as explicit, direct-implicit and diagonal-implicit methods. These are described in through Eqs. 4.4, 4.5, and 4.6 respectively.

$$\delta u_{i,exp}^n = -\alpha(u_i^n - u_{i-1}^n) + \beta(u_{i+1}^n - 2u_i^n + u_{i-1}^n) \tag{4.4}$$

$$-(\beta + \alpha)\delta u_{i-1}^n + (1 + 2\beta + \alpha)\delta u_i^n - \beta\delta u_{i+1}^n = \delta u_{i,exp}^n \tag{4.5}$$

$$(1 + 2\beta + \alpha)\delta u_i^n = (\beta + \alpha)\delta u_{i-1}^{kmax} + \delta u_{i,exp}^n + \beta\delta u_{i+1}^{kmax} \tag{4.6}$$

The diagonal-implicit method used here is essentially a block-Jacobi type – the off-diagonal terms are taken to the right-hand side in the implicit formulation, and then are iteratively corrected within an implicit time-step using a series of $kmax$ Jacobi-iteration steps. The $kmax$ is the same parameter as used in the DPLR [41] implicit method. In this approach, first the off-diagonal terms are ignored and the initial value of change in the solution $\delta u_i^{(0)}$ is obtained by operating the explicit residual $\delta u_{i,exp}^n$ with the inverse of the diag.-implicit operator.

$$\delta u_i^{(0)} = (1 + 2\beta + \alpha)^{-1}\delta u_{i,exp}^n \tag{4.7}$$

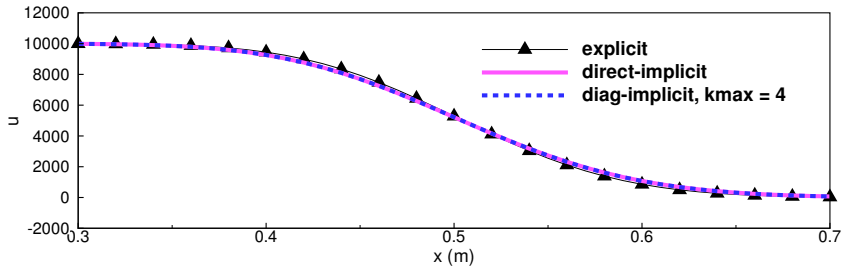

(a) CFL = 0.1

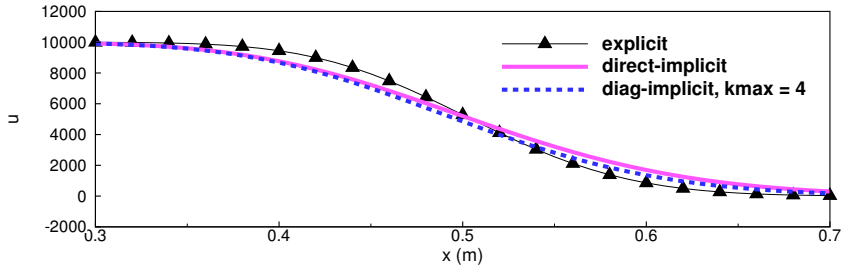

(b) CFL = 0.8

Figure 4.2: Numerical solutions for convection-diffusion equation at $t = 0.5$ s

Then, a series of $kmax$ relaxation steps using Jacobi-iteration is made for $k = 1$ to $kmax$. The implicit change in the solution at k^{th} sub-iteration can be written as,

$$\delta u_i^{(k)} = (1 + 2\beta + \alpha)^{-1}[\ \delta u_{i,exp}^n + (\beta + \alpha)\delta u_{i-1}^{(k-1)} + \beta \delta u_{i+1}^{(k-1)}] \tag{4.8}$$

Finally, the net implicit update at the end of n^{th} time-step is calculated as $\delta u_i^n = \delta u_i^{kmax}$

Preliminary Results

The solution to the convection-diffusion problem are presented here at time, t = 0.5 s. Numerical solutions are obtained using explicit time-integration, and with implicit methods where full-implicit system of equations is solved in two different ways. The first is direct-implicit, in which both convective and diffusive fluxes are treated implicitly and the system of equations is solved exactly by direct matrix back-substitution. The second method is diagonal-implicit where only the main diagonal of the block-tridiagonal linear system of equations is inverted, whereas off-diagonal terms are relaxed using Jacobi iterations. The gas velocity profiles are shown in Fig. 4.2

The wave speeds using these methods with varied CFL are presented in Table 4.2. The explicit solution captures the wave motion in a time-accurate manner, but the time-step size is constrained by CFL stability condition. For the model problem considered here, the 1^{st} order accurate explicit euler method requires a time-step size of 1 ms (CFL = 0.1).

Table 4.2: Numerical wave speeds (m/s) for convection-diffusion equation

CFL no.	Δt ($\times 10^{-3}$ s)	Explicit	Direct-implicit	Diag.-implicit $kmax = 4$	Diag.-implicit $kmax = 30$	Diag.-implicit $kmax = 100$
0.1	1.0	1.00	1.00	1.00	1.00	1.00
0.8	8.0	1.00	1.00	0.98	1.00	1.00
10.0	100.0	-	1.00	0.33	0.97	1.00

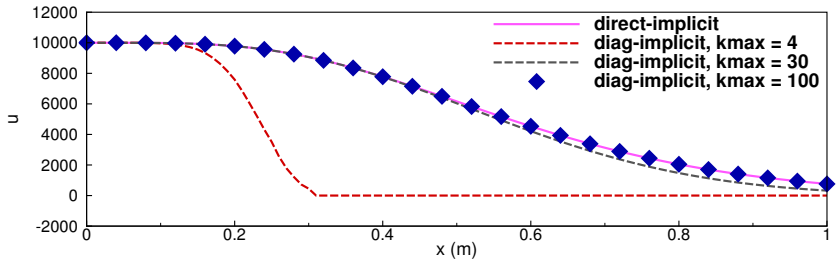

Figure 4.3: CFL=10.0, Diag.-implicit solution with varied *kmax*

The direct-implicit scheme is time-accurate and stable, but requires the solution of the full-tridiagonal system of equations exactly. The explicit method with a CFL number as 0.1 can be taken as the reference solution to compare the performance of both implicit methods for CFL numbers up to 1. However, the diagonal-implicit method lags behind in capturing the wave, and the accuracy is further worsened as the CFL number is increased. This behavior is expected since the off-diagonal terms are not exactly computed at the future time-step but are approximated via $kmax$ sub-iterations, and hence there is a lag in the information propagation. When the time-step is small (CFL number = 0.1) all three methods predict accurate wave speed as seen in Fig. 4.2(a). As the CFL number is increased to 0.8 for implicit methods, the diagonal-implicit method requires a higher number of sub-iterations (i.e. $kmax = 30$) to match with direct-implicit solution as shown in Fig. 4.2(b). Both implicit solutions are more diffused than the reference explicit solution. This behavior can be further examined at a much higher CFL number of 10. As seen in Fig. 4.3, a $kmax$ of 100 is now required to match with the direct-implicit solution. It should also be noted that the commonly used $kmax$ value of 4 at this time-step size predicts shock-speed as 0.33 m/s which has 67% error with respect to analytical shock-speed. This clearly demonstrates the need of ensuring tight-convergence during iterative-implicit calculations.

The explicit time-integration is unaffordable for such high-speed wave propagation problems due to extremely small time-step requirements. The direct inversion of the full-implicit method gives stable and time-accurate solutions at practical time-step sizes but involves matrix factorization operations of the large-sparse matrix system. An efficient way to solve such unsteady systems is by improving the accuracy of diagonal-implicit type methods

Table 4.3: Initial Conditions

Case no.	M_s	Location	p (Pa)	ρ (kg/m^3)	T (K)	u_{gas} (m/s)	h_0 (MJ/kg)
2(a)	2.88	Driver gas	319.8	1.462×10^{-3}	762.24	732.91	0.72
2(a)	2.88	Driven gas	26.6	3.096×10^{-4}	300	0	0.72
2(b), 3	28 to 30	Driver gas	1.904×10^{6}	1.1055	6000	0	31.2
2(b), 3	28 to 30	Driven gas	26.6	3.096×10^{-4}	300	0	31.2

which are already used in industrial solvers such as US3D [57].

This realization is helpful since actual engineering problems in high-temperature gas dynamics usually consist of a large sparse matrix system. In practice, the implicit system is solved with a Jacobi point- or line-relaxation method such as FMDP [73] and DPLR [41] etc. with $kmax = 4$ sub-iterations to relax off-diagonal terms. This works well for steady-state shock problems such as hypersonic flow over a blunt-body, however, the high-speed shock-propagation problem requires absolute time-accuracy for proper shock-tracking. The above analysis shows that the performance of diagonal-implicit system is significantly improved either by reducing the time-step size, Δt or by increasing the $kmax$; the number of sub-iterations in the relaxation process.

As mentioned earlier, should the diagonal-implicit relaxation scheme be used without proper modification, not only the predicted shock-speed can be wrong but it can also cause a thermodynamically inconsistent post-shock gas state as will be shown in the upcoming sections. More importantly, such results could be easily thought of as the correct solution in absence of thorough analysis and understanding of the behavior of strongly hyperbolic systems. This hypothesis is investigated in the next section for shock-propagation at low- and high-Mach number conditions.

4.1.2 Shock propagation in perfect gas

Numerical simulations are now performed for one-dimensional shock propagation in air. The diaphragm is located at 0.1 m. The performance of the numerical methods is first analyzed for low Mach conditions ($M_s = 3$) where analytical solution is available, followed by high-speed shock propagation in EAST at perfect gas conditions.

4.1.3 Shock propagation at Mach 3, perfect gas

Numerical solutions are obtained in three different ways, referred to as run 1, 2 and 3 in Table 4.4. The time-integration is done using 2$^{\text{nd}}$ order Euler Explicit and Implicit FMDP point-relaxation type methods. A central, 2$^{\text{nd}}$ order spatial accurate KEC [72] flux-scheme is employed in all cases. The first two runs use a significantly small time-step $\Delta t = 0.2$ ns (CFL number = 0.03). At this time-step size, both the explicit and implicit methods

Table 4.4: Summary of results for Air shock, $M_s = 3$

Run no.	CFL number	Δt ($\times 10^{-9}$s)	Time integration	U_s (km/s)	W_s/λ_∞	$T_{\max}$
1	0.03	0.2	explicit, 2$^{\text{nd}}$ order	1.04	4.15	815
2	0.03	0.2	implicit, 2$^{\text{nd}}$ order	1.03	4.21	813
3	0.70	4.4	implicit, 2$^{\text{nd}}$ order	0.66	1.54	737

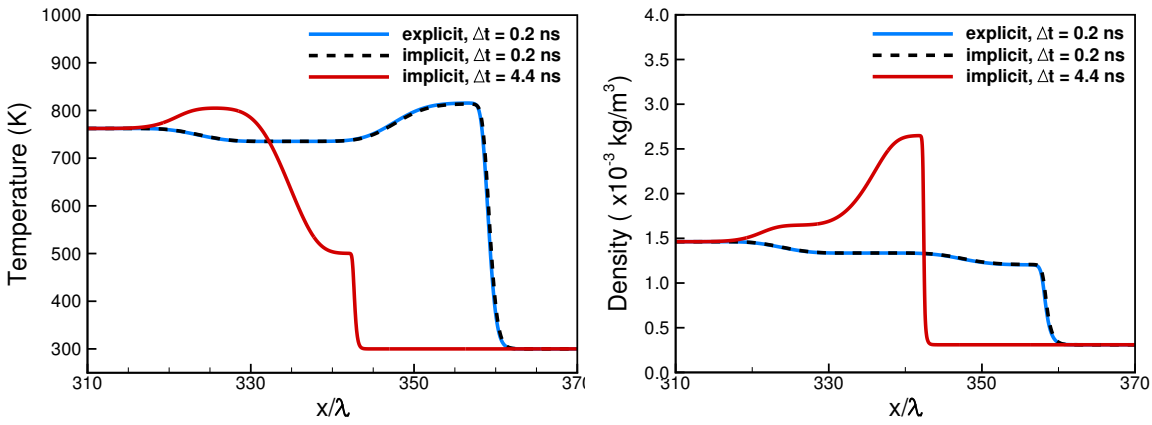

Figure 4.4: Numerical solutions for Mach 3 shock, at $t = 11.68$ μs

predict a shock-speed very close to the analytical shock-speed. In run 3, the time-integration scheme is the same as in run 2, but the time-step is increased to $\Delta t = 4.4$ ns (CFL number = 0.7) which gives a lower shock-speed and a totally different post-shock gas-state. This is noted in Table 4.4. The peak temperature just behind the shock T_{max} is dropped by 10% in run 3. The temperature and density profiles are shown in Fig. 4.4; plotted against x/λ, the axial distance (x) non-dimensionalized by the free-stream mean-free path ($\lambda_\infty = 0.27$ mm). There is a spurious overshoot in the density profile for run 3. The shock-width, W_s, is also significantly different.

Thus, for implicit method, run 2 can be taken as the reference solution and the efforts are now made to improve the solutions from run 3 ($\Delta t = 4.4$ ns) to match with run 2 by increasing the $kmax$. As shown in Fig. 4.5 the reference solution which is implicit 2$^{\text{nd}}$ order with $\Delta t = 0.2$ ns and $kmax = 4$; is compared with implicit solution using $\Delta t = 4.4$ ns and $kmax =$ 4, 30 and 100. It is seen that $\Delta t = 4.4$ ns with $kmax = 100$ can reproduce same result as with $\Delta t = 0.2$ ns and $kmax = 4$. This improvement in the solution accuracy can be attributed to the faster rates of convergence of numerical residuals due to better approximated off-diagonal terms using higher $kmax$.

It can be concluded that the implicit point-relaxation method, when used for unsteady problems, gives the advantage of numerical stability compared to the explicit methods. But even at this low-Mach flow, the solution is highly sensitive to the time-step size and the

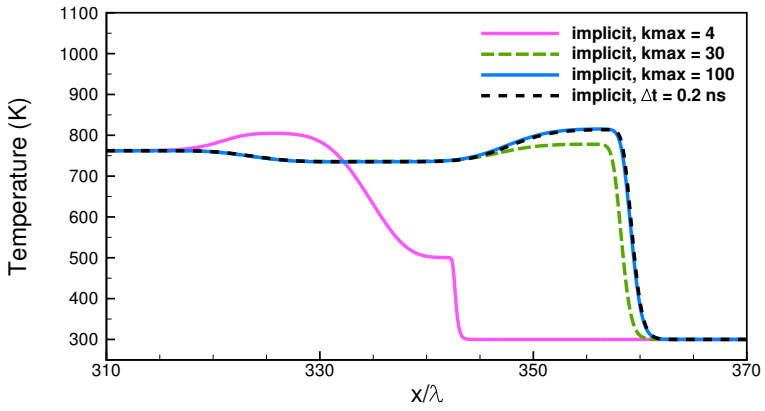

Figure 4.5: Numerical solutions for Mach 3 shock using implicit method with varied $kmax$, at $t = 11.68$ μs

accuracy involved in approximating the off-diagonal terms. This behavior is similar to that suggested by the analysis of the model convection-diffusion solutions.

4.1.4 Shock propagation in EAST, perfect gas

The initial conditions for this simulation are described in the Table 4.3. The post- to pre-shock pressure ratio is huge, i.e., $\mathcal{O}(10^5)$. Such large pressure difference is used to produce a high-speed shock wave at Mach number $\approx$ 28-30. The simulations in this section assume perfect gas flow, which is invalid at EAST conditions, yet a suitable choice to test different numerical methods. Similar to the low-Mach case, the diaphragm is located at $x = 0.1$ m.

Implicit simulations with a CFL number of 1.0 are carried out using three methods: (a) the FMDP [73] method, which is essentially a block-Jacobi, (b) an exact tridiagonal solution of the block tri-diagonal linearized system, and (c) an iterative method based on the GMRes [59] algorithm that is preconditioned with the block-Jacobi method. The simulations are executed until a pre-specified elapsed time when the shock waves are well-formed for all cases.

Based on earlier findings, the solutions from the FMDP with default settings (i.e. $kmax = 4$) are expected to predict wrong shock-speed which is indeed the case here. However, the method also calculates an incorrect post-shock gas state. In particular, Fig. 4.6 shows the temperature as a function of location in the one-dimensional domain. The FMDP method with $kmax$=4, predicts a peak gas temperature of about 40,000 K whereas the simulation results by solving the linear system exactly through direct matrix-inversion; give a significantly different answer. The latter predicts a post-shock gas temperature of 65,000 K for current prefect gas calculations. It is also noted that the shock location predicted with the FMDP method is lagged behind than the exact solution. These observations are

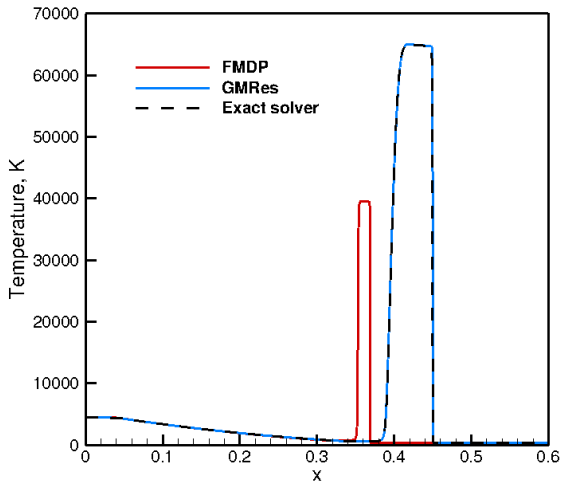

Figure 4.6: Numerical solution for Case 3 with perfect-gas behavior, at $t = 30.0$ μs

consistent with the earlier findings in Sec. 4.1.3

It is also noted that the predictions from iterative GMRes method are nearly identical to that using the exact solver. This is because the GMRes method relies on tunable parameters to efficiently iterate the linear system solution within an acceptable error-tolerance. Nompelis et al. [58] performed sensitivity studies to guide the GMRes parameter tuning for hypersonic flow simulations which are utilized in current analysis.

Computational cost As the GMRes embedded algorithm turns out to be a possible choice to correctly solve the high-speed shock propagation in EAST, a comparison of computation-cost is carried out to realize the potential of these methods in a practical sense. For this purpose, the simulations are performed since just after the diaphragm rupture until $t = 0.5$ μs using 8 processors on a paraller computing architecture. The FMDP [73] method with $kmax = 4$ requires about 96 minutes whereas the GMRes embedded algorithm takes about 367 minutes. The GMRes method is more expensive than the standard DPLR [41] and FMDP [73] methods that are used in practice for implicit solutions. Therefore, it should only be used for classes of problems where a very accurate linear system solution is necessary as is the case here. For current test case, GMRes method is 4 times more expensive than the basic FMDP method with $kmax$=4. However, the GMRes based method is 30% cheaper than FMDP with $kmax$=100, which gives a time-accurate solution. The cost difference is based on the choice of the tunable parameters that guarantee convergence to the correct solution. In general, the method has only an *a priori* cap on the cost, but the

actual cost varies from time-step to time-step depending on how the flow evolves.

4.1.5 Shock propagation in EAST, reacting gas

As mentioned earlier, EAST flow is highly energetic and reactive in nature. The time-step size requirement for an explicit method is 0.05 ns which is not affordable in practice. Solving the full-implicit system of equations allows to take larger time-steps but the savings on total computation cost are limited by the latency introduced during inter-processor communication on parallel computers. It is clear that using an implicit point-relaxation is the feasible option but proper modifications should be incorporated to achieve desired time-accuracy. Based on this understanding, EAST reacting gas simulations are performed using the modified Steger-Warming [74] flux-scheme with the FMDP implicit 1^{st} order point-relaxation method. Since the grid is extremely resolved, the numerical dissipation provided by the upwinding nature of the MSW flux-scheme is small, hence, the flow behavior is governed by the physical viscosity of the gas and not by the artificial viscosity introduced by the numerics. This enables for accurately resolving the strong flow gradients across high enthalpy shocks in EAST. The FMDP scheme used here is 1^{st} order accurate in space and has total-variation diminishing (TVD) properties due to the monotonicity provided by upwinding in the direction of advection. The 1^{st} order Euler time-integration method is used.

The one-dimensional EAST flow is examined in three steps. First, the point-relaxation time-integration method is modified to solve the implicit system of equations in a more accurate manner by adjusting the number of sub-iterations (i.e. $kmax$) used to iteratively correct the relaxed off-diagonal terms of the block-tridiagonal system within an implicit time-step. The higher the value of $kmax$, the more accurately the implicit system is solved. This analysis helps to find an optimal value of $kmax$. Next, with this optimal $kmax$ setting, the sensitivity of the numerical solution is assessed using different values of CFL number (i.e. different time-step sizes while the grid is same). Finally, using the optimal values for $kmax$ and the CFL number a grid convergence study is performed. This analysis is presented below.

Convergence of the linear system

As explained in Sec. 4.1.3, a higher value of the parameter $kmax$ can be directly related to the improved accuracy of the implicit system being solved. In order to quantify this behavior, the numerical calculations are performed using $kmax$ values ranging from 4 to 400. The numerical results are put together in Table 4.5 and Fig. 4.7 below. Temperature and density profiles are plotted along the distance in the axial direction normalized by free-stream mean free path, i.e., x/λ_∞. The shock-speed and post-shock temperature is

Table 4.5: Summary of results at $t = 10$ μs

Run no.	$kmax$	U_s (km/s)	$T_{\max}$ (K)
1	4	9.12	25312
2	30	10.34	39288
3	100	10.52	42198
4	200	10.52	42209
5	400	10.52	42209

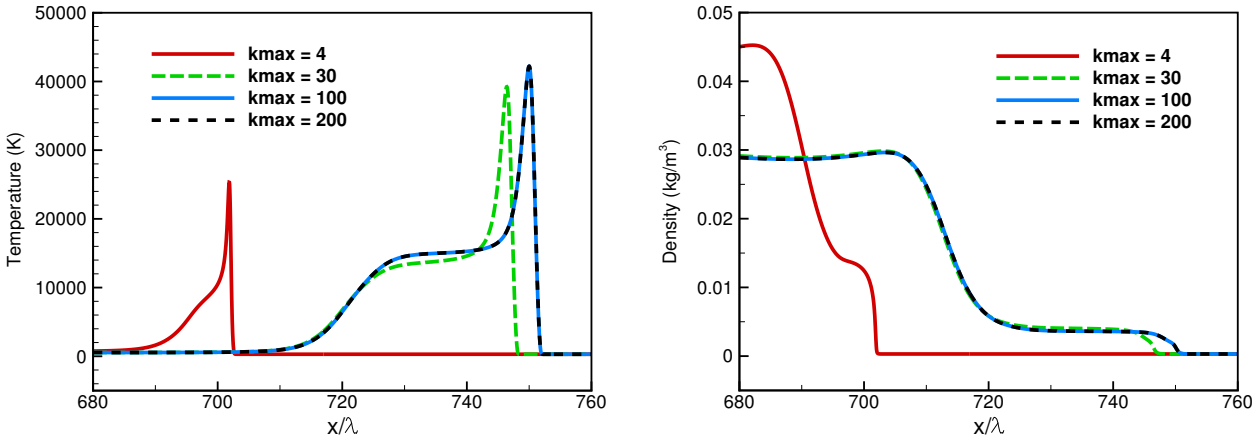

(a) Temperature **(b) Density**

Figure 4.7: Numerical solutions, Case 3 with varied *kmax*, at $t = 10$ μs

significantly improved when $kmax$ is changed from 4 to 30. After $kmax$ 100,the numerical solution can be assumed to be converged. The shock-speed with $kmax$ of 4 is only 9.12 km/s with about 14% error as compared to converged shock-speed of 10.52 km/s with $kmax$ of 100. The error in peak temperature is about 17,000 K which is far beyond the acceptable limits.

Computational Cost Once the shock has fully developed and has propagated about 0.1 m in the axial direction, the simulations with varied $kmax$ are run for a physical time of $t = 0.5$ μs using 8 processors. The computation cost for $kmax = 100$ is about 7 times that of $kmax = 4$; as shown in Fig. 4.8

Sensitivity to time-step size

After setting $kmax$ to the optimal value of 100, the time-step size is varied while the cell-size is kept at the baseline value (i.e. $\Delta x = 8.4$ μm). Using $kmax$ as high as 100, the shock-speed is captured in a fairly accurate manner, even with larger time-steps. However, the post-shock gas state is still a strong function of time-step size as seen in Table 4.6.

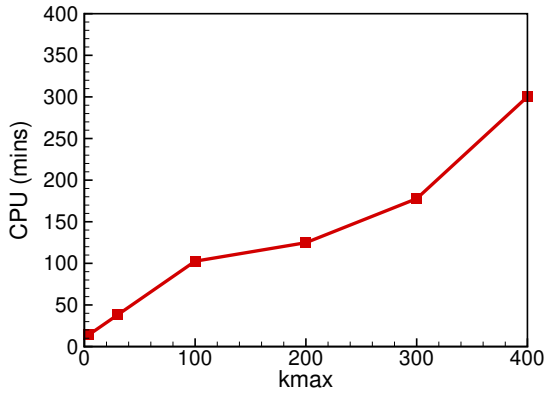

Figure 4.8: Computation cost for 1D East simulations with varied *kmax*

Table 4.6: Summary of results for time-step size variation

Run no.	CFL	Δt (ns)	$kmax$	U_s (km/s)	$T_{\max}$ (K)
1	0.3	0.19	100	10.54	42675
2	0.7	0.44	100	10.56	42098
3	2.0	1.27	100	10.53	38419
4	3.5	2.24	100	10.48	32886

Depending on the acceptable-error in the prediction of post-shock gas properties, a suitable time-step size can be chosen. For current purposes, a CFL number of 0.7 gives a good trade-off between computational-time and numerical-accuracy.

Sensitivity to cell-size Finally, grid-convergence is studied using half-, double- and quadruple-sized cells with respect to reference cell-size of $\Delta x = 8.4$ μm. The $kmax$ parameter is set to 100 and the time-step is $\Delta t = 0.44$ ns (CFL = 0.7); based on the conclusions from the previous steps. The results are presented in Fig. 4.10. Though the shock-speed is a weak function of cell-size but the post-shock gas state changes significantly as the grid is coarsened. For practical purposes, a grid-size of $\Delta x = 16.8$ μm is chosen as baseline cell-size for two-dimensional axisymmetric simulations. Table 4.7 shows a summary of key flow parameters in each case.

Table 4.7: Summary of results for Grid-convergence study

Grid no.	Δx (μm)	Δt (ns)	U_s (km/s)	$T_{\max}$ (K)
1	4.2	0.44	10.33	38726
2	8.4	0.44	10.54	42198
3	16.8	0.44	10.65	40065
4	33.7	0.44	10.86	36827

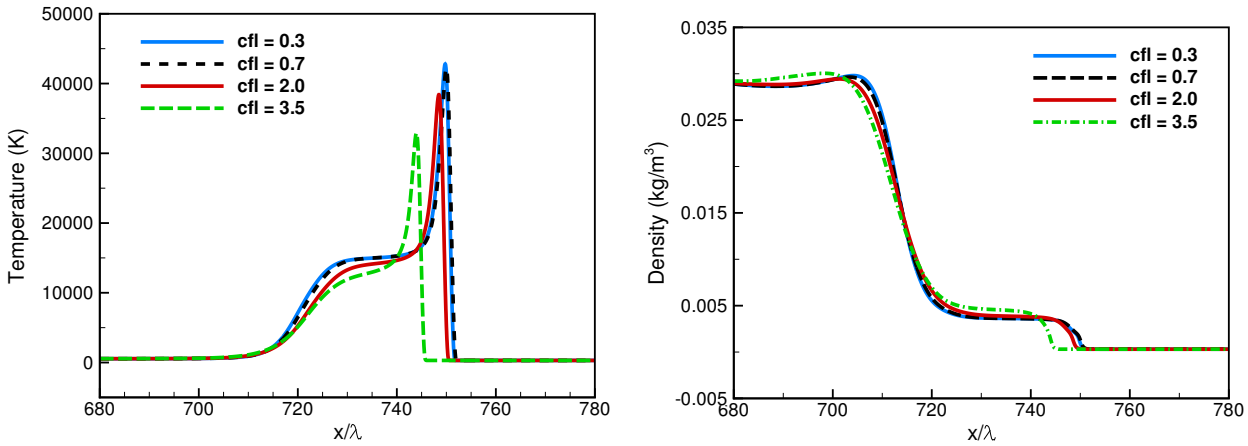

(a) Temperature (b) Density

Figure 4.9: Numerical solutions, Case 3 with varied time-step size, at $t = 10\ \mu s$

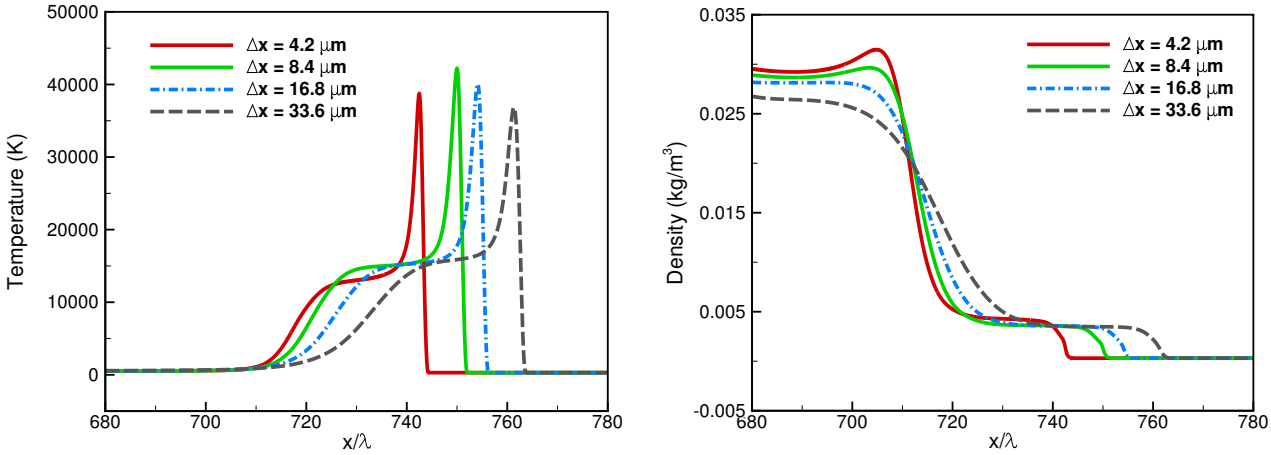

(a) Temperature (b) Density

Figure 4.10: Numerical solutions, Case 3 with varied cell-size, at $t = 10\ \mu s$

Table 4.8: Initial conditions

Region	P(N/m^2)	T(K)	u (m/s)
Driver gas	9.28×10^{-4}	1000	670
Test gas	2.99×10^{-4}	300	670

With the analyses presented above, the numerical methods are optimized to produce accurate solutions for high-speed wave propagation in EAST. These optimal parameters will guide the numerical set-up for two-dimensional axisymmetric calculations. However, the conservation equations are solved in a laboratory fixed-frame of reference using a uniform, highly refined grid, which is not a feasible set-up for full-tube EAST simulations. Therefore, the next step is to minimize the computational cost by implementing the moving-frame of reference described in Chapter 3. This is presented in the next section.

4.2 Validation studies

One-dimensional Mach 2 shock in Nitrogen is taken as a test case for the moving-frame of reference calculations in US3D flow solver. The numerical predictions are validated against analytical solution for accurate wave-speeds, post-shock gas properties and the conservation of mass, momentum and total energy across the shock. The initial conditions are described in Table 4.11. The speed of moving-frame is 670 m/s, same as the analytical shock speed at these conditions. Thus, the motion of the shock with respect to the computational grid is minimal.

4.2.1 Post-shock gas state

Post-shock gas temperatures are shown in Fig. 4.11, after 6.3 m of shock propagation. The dashed lines represent post-shock gas equilibrium temperature computed with NASA's Chemical Equilibrium with Application (CEA) code. Gas temperatures predicted with moving-frame of reference approach match exactly with CEA predictions.

4.2.2 Conservation laws across the shock

The gas properties change drastically due to the shock-heating, however, the total mass, momentum and total energy of the flow remain conserved across the shock. In this section, conservation of these quantities is investigated for the numerical solutions obtained from the moving-frame approach. The numerically predicted flow field is shown in Fig. 4.12a and different regions of the shock tube flow are indicated. The mass-flux, axial-momentum flux and total energy flux are plotted in Fig. 4.12b. The numerical solution conserves these

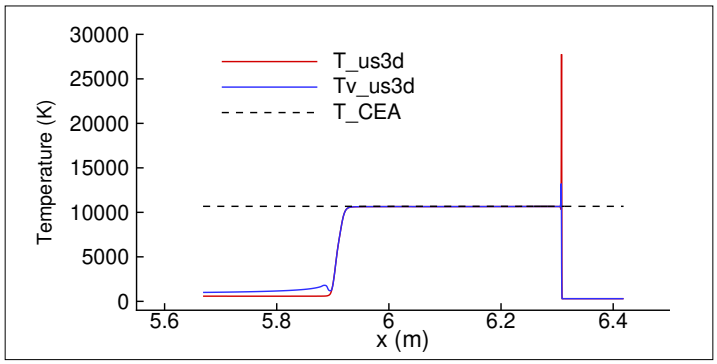

Figure 4.11: Gas temperatures with moving-frame calc., Mach 2 shock in Nitrogen

Table 4.9: Post-shock properties: US3D vs. CEA data

Flow variables	Pre-shock	Post-shock (US3D)	Post-shock (CEA)
pressure, P (N/m^2)	26.67	107.8	108
temperature, T (K)	300	482.4	481
das speed, u (m/s)	0	404.16	404.12
density, ρ (kg/m^3)	2.99×10^4	7.53×10^4	7.55×10^4
specific enthalpy, h_0 (MJ/kg)	0.5361	0.5364	0.5361
mass-flux (kg/m^2 s)	0.2001	0.2005	0.2001
x-mom. flux (N/m^2)	161.02	161.02	161.02

quantities in the post-shock gas region within 0.5% of the pre-shock values. A summary of pre- versus post-shock gas properties is shown in Table 4.9. Numerical predictions predict post-shock equilibrium properties exactly.

4.2.3 Wave speeds

The shock front and the contact front move from left to right, and the expansion wave moves in the opposite direction. The expansion fan leading edge (LE) and trailing edge (TE) locations are shown in Fig. 4.12a along with the shock and the contact front. The space-time evolution of all four waves is shown in Fig. 4.13a. The wave locations are detected in the numerical solutions and wave speeds are computed as a function of time, and as a function of the distance along the tube. These are shown in Fig. 4.13b and 4.13c respectively.

Numerically predicted wave speeds are also compared with analytical wave speeds in different regions of the flow. This is shown in Table 4.10 . Numerical wave speeds are represented by w_n. The analytical shock speed is u_s and the contact front moves at local sonic speed, a. The analytical speeds for expansion fan LE and TE are a-u_s and a+u_s, respectively. The numerical solution captures all wave speeds within 2% error.

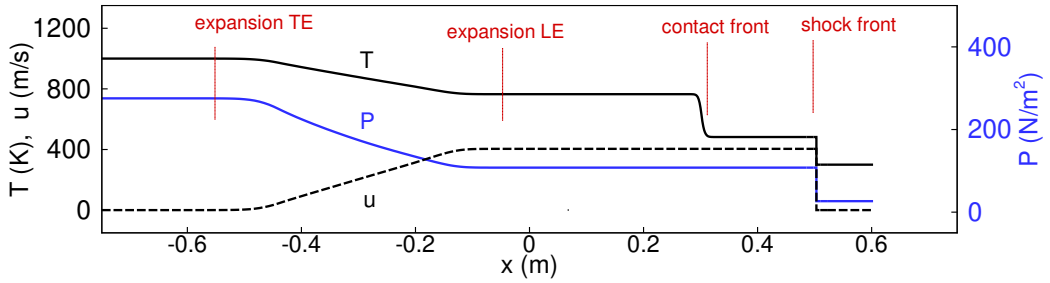

(a) Flow field

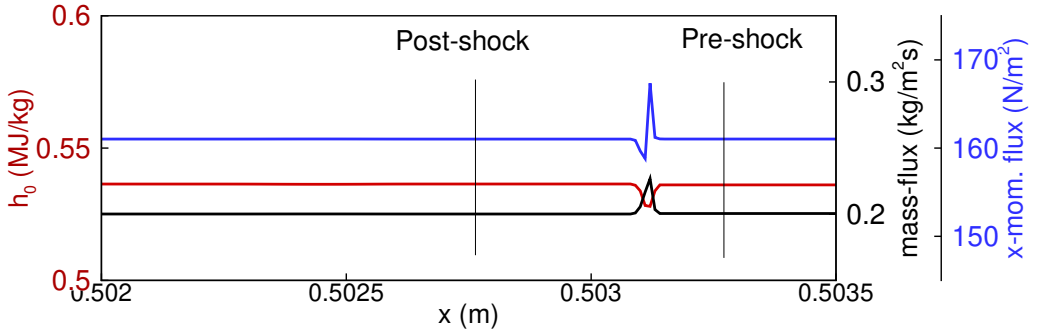

(b) conserved quantities

Figure 4.12: Conservation across the shock, Mach 2 shock in Nitrogen

Table 4.10: Wave-speeds: Analytical vs. US3D

Region	wave type	T(K)	sonic speed a (m/s)	analytical speed w_a (m/s)	US3D wave speed w_n (m/s)
Driver (He)	expansion TE	1000	1861	a+u_s	2531
Expansion zone (He)	expansion LE	765	1627	a-u_s	1020
Post-shock (N_2)	contact front	481	446	a	440
Pre-shock (N_2)	shock front	300	353	u_s	670

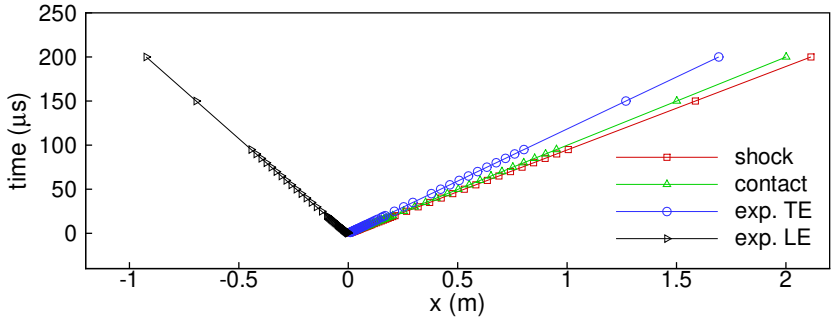

(a) x-t diagram

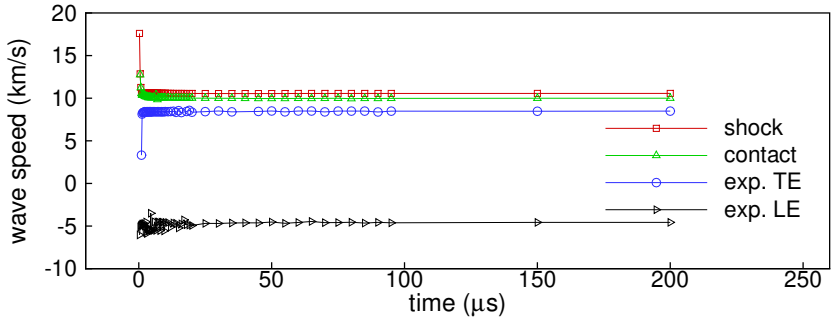

(b) Wave speeds with time

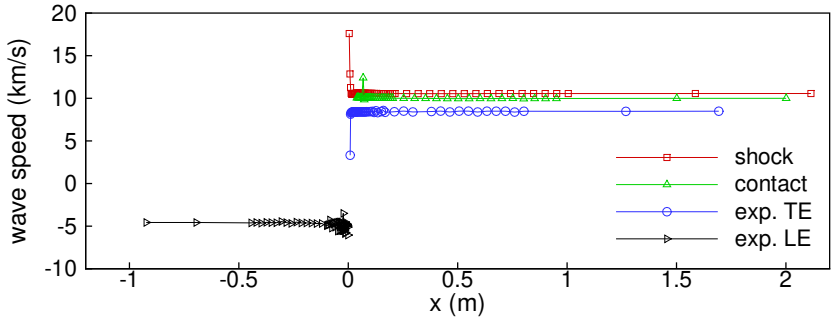

(c) Wave speeds along the tube

Figure 4.13: Numerical predictions for Mach 2 shock in Nitrogen

4.3 Assessment of domain boundary conditions

As mentioned in Chapter 3, only a small portion of EAST shock tube is modeled with the moving-frame of reference approach. However, this also means as the shock moves forward in the tube, the upstream flow-field information is gradually lost once the expanded driver gas starts exiting from the left domain boundary. An accurate boundary condition (BC) at this location would be to use a subsonic outflow where the flow parameters are calculated and updated in each time-iteration. The implementation of such time-varying BC is non-trivial, and moreover it can introduce numerical oscillations in the flow-field. Another option is to use a Neumann BC, referred to as supersonic outflow, which basically sets a zero-gradient between the interior cells adjacent to the boundary and the ghost-cells representing the boundary. It should be noted that as the expansion waves start crossing this boundary, the actual flow-field will have weak non-zero gradients. Therefore, implementing a supersonic outflow with zero gradients introduces small numerical errors which accumulate during the long-time integration. Finally, the supersonic inflow BC is also tested at this boundary. In this case, the ghost cells flow variables are set to freestream test gas conditions after every time-step. ((**NOTE: it should have been tested by using initial driver gas conditions as the inflow because setting it as freestream gas does not make sense; I'll either remove this case from the comparison, or run a new test case) This is a valid assumption only until the expansion waves are sufficiently far from the left boundary. **) Therefore, the numerical errors with this BC choice are expected to grow significantly as expansion waves approach to left boundary.

It is important to quantify the effect of modeling a small portion of the tube versus the full-tube, and identify appropriate boundary conditions such that numerical predictions are accurate for the entire duration of shock propagation. For this purpose, three sets of simulations are performed on computational grids with the domain lengths of 0.6 m, 4 m and 24 m, respectively. The shock tube flow is initialized with EAST jump-conditions corresponding to an approximate shock speed of 10 km/s in the experiment. One-dimensional simulations are performed for the perfect gas and reacting gas behavior, using a long and a short computational domain. These are referred to as Case 1 and 2, respectively, in this section. The initial conditions are described in Table 4.11. The domain length and speeds of frame-motion are described in Table 4.12. The length of the long domain is chosen such that the expansion waves are contained within the computational domain for the entire duration of simulated physical time, and numerical predictions match with the analytical solution. Hence, the numerical solutions obtained on the long domain can be taken as the reference solution to assess the performance of short domain simulations. The short domain length in each case is 0.6 m; this is the desired domain length for two-dimensional axisymmetric

Table 4.11: Initial conditions

Region	Composition (by mass)	ρ(kg/m^3)	T(K)
Driver gas	He + 0.1%N_2	1.10546×10^{-4}	6000
Test gas	76.7% N_2 + O_2	3.096×10^{-4}	300

Table 4.12: List of test cases

Case no.	Flow behavior	Frame-speed u_f (km/s)	long domain (m)	short domain (m)
1	Inviscid, Perfect gas	11.5	4	0.6
2	Viscous, Reacting gas	10.5	24	0.6

simulations based on the width of hot gas region in shock spectroscopic images collected at EAST. Two sets of boundary conditions are specified at the left boundary of the short domain by using either a supersonic inflow or outflow. These numerical predictions are compared against the reference solution obtained from long-domain simulations.

4.3.1 Inviscid, perfect gas flow

The behavior of inviscid, perfect gas flow is discussed here. Such flow behavior is not realistic for the high enthalpy EAST jump-conditions in these simulations, but is used as a test-case to understand and quantify the numerical behavior under various flow conditions. There are no viscous losses and the gas is assumed to be thermally perfect in this case. Hence, the entire energy of the driver gas is absorbed by test gas translational energy mode, leading to a numerically predicted shock speed of 11.5 km/s. Numerical results are shown at elapsed time 166 μs. The left domain boundary for the short domain is located at 1.6 m, and the shock front is at 1.9 m. The profiles of key flow variables are shown in Fig. 4.14. The outflow BC on the left boundary predicts an accurate flow behavior whereas the implementation of inflow BC leads to an artificial expansion of the flow near the boundary. The accumulated errors with outflow BC are neglegible until this elapsed time-level. The next step is to investigate these effects for full-tube shock propagation in EAST with reacting gas behavior.

4.3.2 Viscous, reacting gas flow

Finally, the full-tube simulations are performed with a more realistic representation of EAST flow. An 11-species weakly ionized Air model is used to accurately capture the reaction kinetics. These one-dimensional simulations predict a shock speed of 10.5 km/s. The profiles of key flow variables are shown in Fig. 4.15. The shock front has propagated 8.42 m along the tube. The left domain boundary in short-domain simulations is located

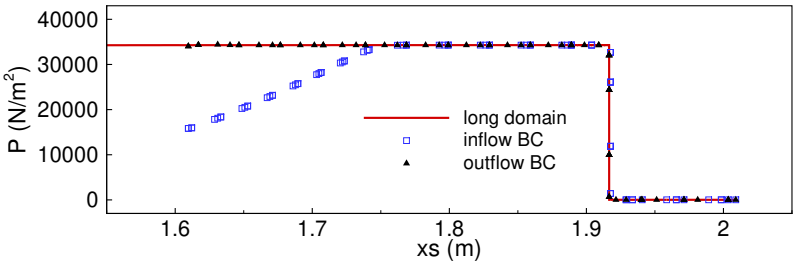

(a) Pressure

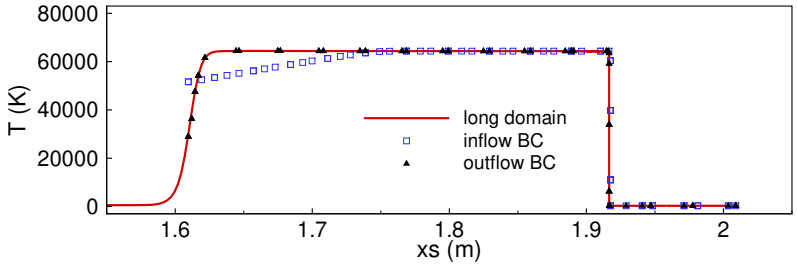

(b) Temperature

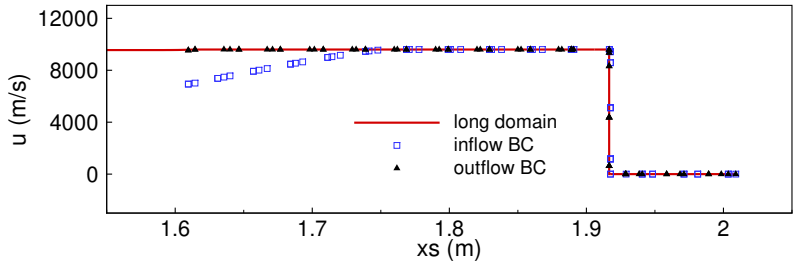

(c) Gas velocity

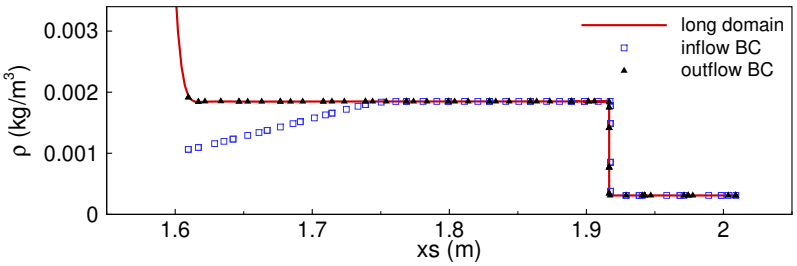

(d) Density

Figure 4.14: Effects of domain BCs for inviscid, perfect gas flow at EAST conditions; Numerical predictions are shown at t = 166 μs.

at 7.8 m. The reference solutions with long-domain are shown in solid red lines, compared against short-domain based predictions. Clearly, the inflow BC is not a good choice as the numerically predicted gas state is significantly disturbed due to the accumulated errors after 8+ m of shock propagation. The shock front location is wrong and the gas ionization behavior is drastically different as seen in the electron no. density plots 4.15e. However, the simulations with supersonic outflow BC capture the flow behavior accurately. The post-shock gas properties closely match with the reference solution with a maximum error of just 0.3%. This analysis proves that supersonic outflow BC is a suitable choice for EAST simulations.

At this stage, the numerical modeling for EAST has been investigated on various aspects and the numerical predictions have been validated against analytical solutions for a range of flow conditions. The optimal numerical set-up identified here will be used for the simulations of two-dimensional axisymmetric EAST flow. This is presented in the next chapter.

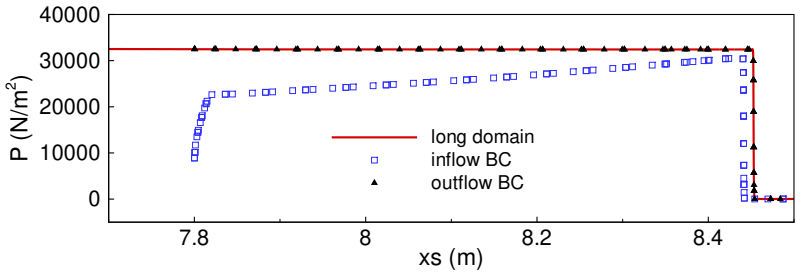

(a) Pressure

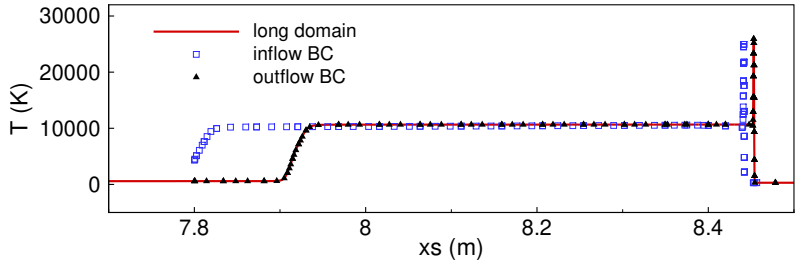

(b) Temperature

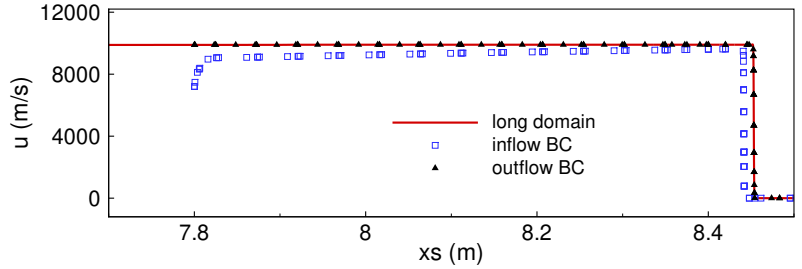

(c) Gas velocity

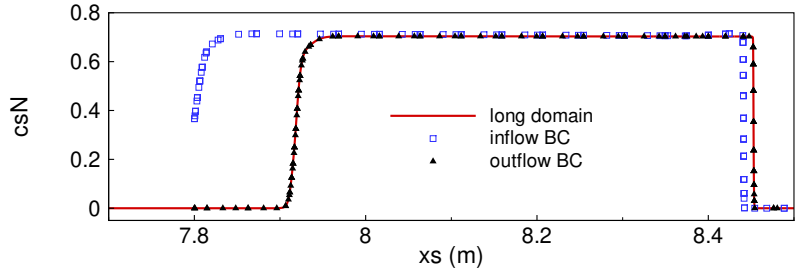

(d) N mass-fraction

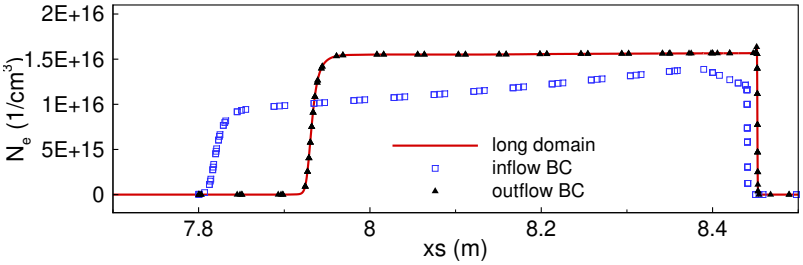

(e) Electron no. density

Figure 4.15: Effects of domain BCs for viscous, reacting gas flow at EAST conditions; Numerical predictions are shown at t = 800 μs.

Chapter 5

Shock tube flow: Air Shocks

The numerical modeling devised and validated in the previous chapters is utilized to simulate the EAST shock tube flow assuming a two-dimensional axisymmetric, laminar behavior. Fluid dynamic computations are performed for a range of atmospheric entry conditions pertinent to Earth and Titan entry missions. The numerical predictions for 10 km/s Air shock experiments are presented in this chapter. The speed of moving-frame of reference is chosen as 10.5 km/s which is the equilibrium shock speed predicted in one-dimensional reacting gas simulations presented in Sec. 4.1.5.

The experimental data show a partially ionized, strong nonequilibrium behavior at these conditions [32], and large enthalpy of the gas results in highly stiff gas chemistry, posing additional challenges for numerical stability. Therefore, the reaction kinetics in EAST is modeled in two stages. As a starting step, only the molecular exchange and dissociation processes are considered while the ionization reactions are ignored to simplify the reaction kinetics. This is a good test case to understand the performance of current numerical modeling for the wall-bounded flow in shock tube. The grid cell-sizes in the axial direction and the time-step sizes for the numerical integration are set based on one-dimensional convergence studies discussed in Sec. 4.1.5. The baseline radial cell-size at the wall is taken as $\Delta r = 1\ \mu m$, corresponding to a non-dimensional distance, $r^+ = 1$. Finally, the two-dimensional axisymmetric EAST simulations are performed with full reaction-kinetics applicable to high enthalpy conditions. The numerical predictions are thoroughly analyzed to understand the hot gas behavior.

5.1 EAST flow, 5-species Air

Numerical calculations in this case are performed on an axisymmetric grid with a uniform axial spacing of $16\,\mu$m for a tube length of 1.1 m. There are 300 grid elements in the radial direction. The grid cell size at the wall is $1\,\mu$m beyond which a hyperbolic tangent

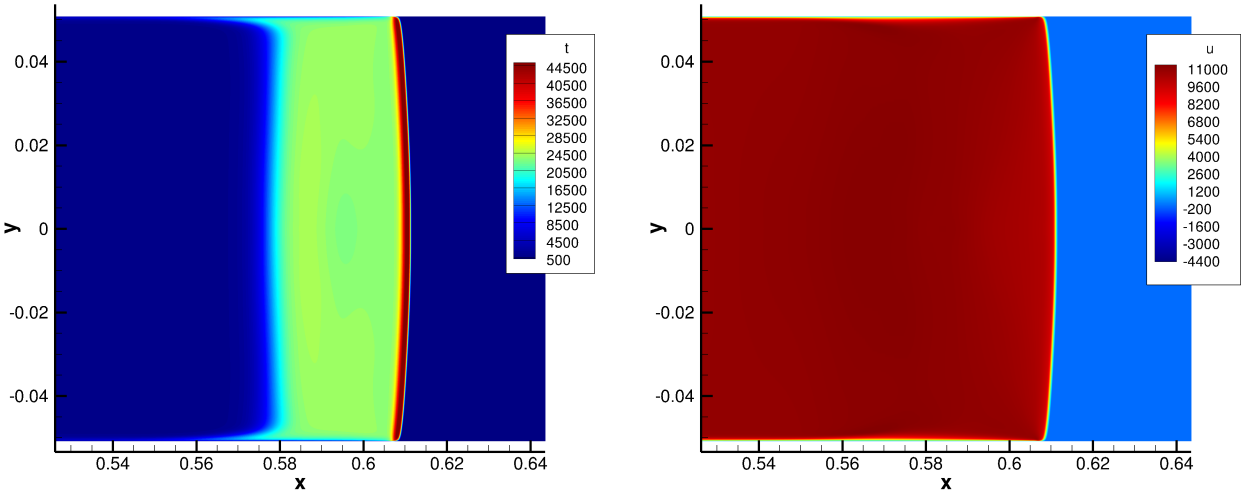

(a) Temperature **(b) Axial-velocity**

Figure 5.1: Contour-plots for 2D axi-symmetric EAST flow, at $t = 56 \times 10^{-6}$ s

based grid-stretching is applied. This results in a grid composed of 20.6M elements. The simulation is run using 6 chemical species in the gas mixture (5-species Air and Helium). A simple harmonic oscillator (SHO) model is used to compute the species vibrational energies.

Based on the analysis presented in Sec. 4.1.5, the current simulations are use a value of $kmax = 100$ for an adequate convergence of the implicit system. The one-dimensional analysis showed that in the vicinity of shock, a CFL of 0.7, i.e. a time step of about 1 ns was adequate to obtain the correct shock speed and post-shock conditions. This is what is used here, corresponding to a CFL number of 225 in the near-wall region due to the small grid spacing. The hot gas flow field is shown after an elapsed time of 56 μs, corresponding to about 0.61 m of shock propagation down the shock tube. Fig. 5.1 presents a contour plot of temperature and axial velocity at this time. The numerically computed shock-speed is 10.8 km/s at this time level which is very similar to what found one-dimensional simulations 4.1.5 with same time-step and grid-cell sizes. Note that the shock wave remains nearly planar, and curves slightly toward the wall, as expected. The simulation attempts without the tight convergence of the implicit problem (i.e., using small values of $kmax$ and larger time step) produced a highly distorted shock wave that was clearly erroneous.

Hence, the current numerical set-up computes the dissociating gas behavior successfully. The next step is to consider a complete thermochemical model by including electronic-energy excitation and ionization processes for a more realistic representation of hot gas behavior. This is discussed in the next section.

5.2 EAST flow, 11-species air model

Numerical simulations are now performed with a complete set of reaction-kinetics using 11-species Air model of Park [60]. The analyses from the previous section are assimilated together to devise an optimized numerical set-up for full-tube shock propagation. The EAST shock tube flow is a high Reynolds number flow with finite-rate and strongly coupled thermochemistry. The current goal is to optimally resolve the finite-rate flow physics exhibited within the relatively thin regions near the shock front and boundary layer. The sensitivity of the numerical solution to the grid cell size in the axial direction and to the time-step size was studied in Sec. 4.1.5, which led to a time-accurate resolution of the shock-structure. A similar analysis is presented here to, 1) optimize the grid cell size in the wall-normal direction, and 2) assess the need of higher order time-accuracy for the numerical time-integration. The optimal parameters obtained here are used for full-tube simulations. The early evolution of the shocked gas flow is thoroughly analyzed to ensure a numerically converged prediction of the initial flow behavior. As the shock front propagates, it becomes fully developed and the gas behavior in the post-shock region attains a near-equilibrium state. The numerically predicted flow behavior is investigated at multiple axial locations for the numerical stability. Finally, the flow predictions at the test-section are analyzed in detail.

5.2.1 Wall-normal cell-size requirements

The numerical predictions during the initial shock formation are compared for three different cell-sizes in the wall-normal direction. These cases are labeled as $\Delta r = 0.5\ \mu m$, $1\ \mu m$ and $2\ \mu m$, which is the size of the first cell at the wall. The grid is geometrically stretched from the wall towards the centerline using a hyperbolic tangent function. We first study the non-dimensional wall distance, y^+ (i.e., r^+), in each case. For sufficiently resolved numerical calculations, a $y^+ < 1$ is desired behind the shock. The axial profiles of wall y^+ values are shown in Fig. 5.2a, where $xs = 0$ represents the shock-front location. In each case, the strong shear present at the shock front leads to high values of y^+ in the vicinity of $xs = 0$. The y^+ values for $\Delta r = 0.5\ \mu m$ and $1\ \mu m$ are similar to each other within $\pm 2mm$ ($\approx$ 8-10 λ_∞) of the shock front, staying closer to $y^+ = 1$ for up to 8 cm and 4 cm behind the shock respectively, whereas the $\Delta r = 2\ \mu m$ case with $y^+ \geq 4$ fails to provide a sufficient grid resolution behind the shock. Since the shock front is always contained within a 4 cm wide heavily refined region, the $\Delta r = 1\ \mu m$ case satisfies y^+ requirements with a lower computational cost than that in $\Delta r = 0.5\ \mu m$.

Next, the numerically predicted shock speed is studied until first 10 μs of shock travel (see Fig. 5.2b). The start-up speed of the shock front is about 30 km/s for $\Delta r = 0.5\ \mu m$ while

other two cases with coarser cells, i.e., $\Delta r = 1$ and 2 μm, predict initial shock speeds of about 26 km/s and 22 km/s respectively. The differences among these predictions quickly diminish as the shock front is decelerated, and by the end of 10 μs, the local shock speed predicted for increasing Δr cases becomes 10.58 km/s, 10.51 km/s and 10.41 km/s respectively. If the shock speeds were to stay constant at these values, the shock front locations after $\approx$ 7.98 m of shock travel (i.e., at t $\approx$ 760 μs) are estimated to be lagged behind by about 5.2 cm, and 12.7 cm from the finest grid case, for $\Delta r = 1$ μm and 2 μm cases respectively. However, the shock speed in each case decreases at a slightly different rate; the deceleration is highest for the finest grid resolution while it is lower for the coarser grids. Therefore, as the shock travels along the tube, the numerically computed shock speeds in three cases come closer to each other and the differences between numerically predicted shock-front locations will be lower than aforementioned estimates.

The near-equilibrium shock speed in the larger Δr cases stay within 1.5% of $\Delta r = 0.5$ μm, therefore, the post-shock gas states are similar to each other. After 10 μs elapsed time, the peak translational (T) and vibrational-electronic temperature (T_v) are about 28,000 K ($\pm$0.4%) and 13,000 K ($\pm$0.44%) for all three cases (results not shown). The axial profiles of electron density, which is the most sensitive function of the local gas state, are shown in Fig. 5.3. As expected, the most refined grid predicts the peak electron density location being the most lagged behind due to maximum shock deceleration. This effect is more prominent in the near wall region, as can be seen in Fig. 5.3a. The boundary layer effects are better captured with the smallest wall-normal cell-size. The flow behavior at the centerline (Fig. 5.3b) shows a difference in the location of the shock front while the electron density values are similar. The location of peak electron density computed on two coarser grids is within 2-3 λ_∞ ($<$ 0.8% error) of the finest grid case.

The radial variation of key flow variables are also studied for each case. Radial profiles of gas temperatures, velocity and electron number density behind 0.5 cm of the shock front are shown in Fig. 5.4. As expected, the flow behavior near the centerline is similar in all three cases whereas there are some differences near the wall. The near-wall plots shown in Fig.5.4 suggest that the difference between the key flow variables stay within 1-2%, and the behavior for $\Delta r = 0.5$ μm and 1 μm cases is practically the same.

The computational cost of these simulations is significantly different. As the wall normal cell-size is halved and quartered from an initial value of $\Delta r = 2$ μm, the computations become about 2.5 and 4.5 times more expensive respectively. Since the differences in the shocked gas state become smaller as the shock front approaches a near equilibrium speed, a cell-size of $\Delta r = 1$ μm at the wall is an optimal choice for full-tube simulations. This enables for sufficiently resolved near-wall flow predictions at a feasible computational cost.

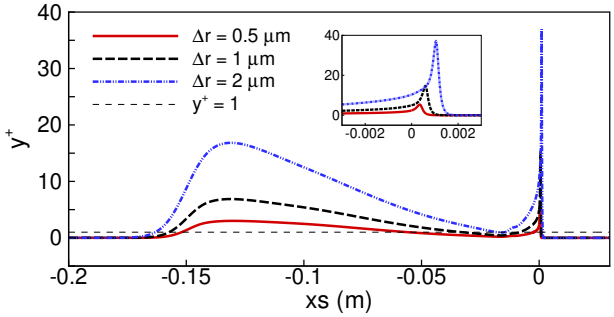

(a) wall y^+ profiles at t = 10 μs

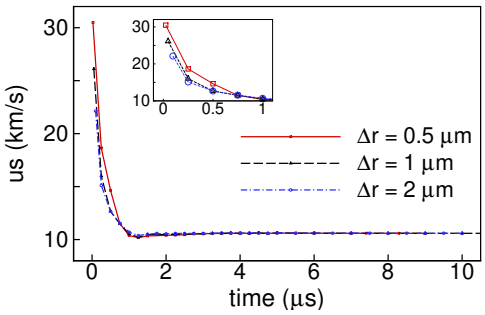

(b) Shock speed

Figure 5.2: Numerical predictions with varied wall-normal cell-size

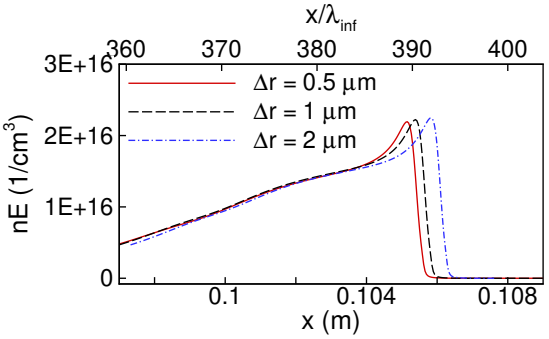

(a) near wall, r = 5.06 cm

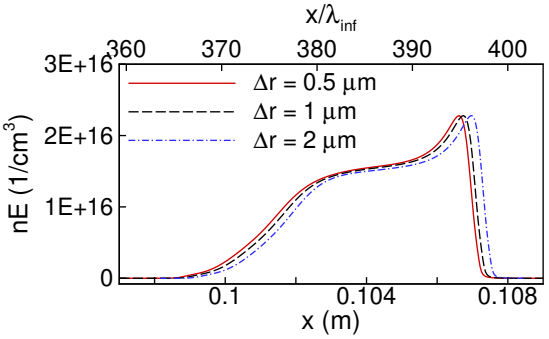

(b) at centerline, r = 0 cm

Figure 5.3: Electron density profiles at t = 10 μs with varied wall-normal cell size

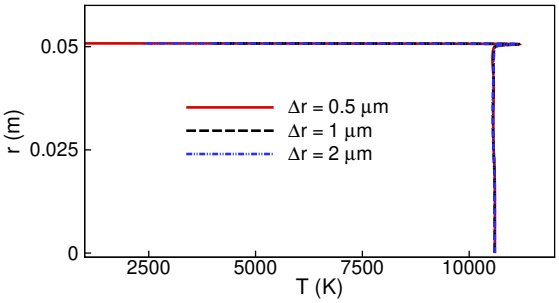

(a) Translational temperature

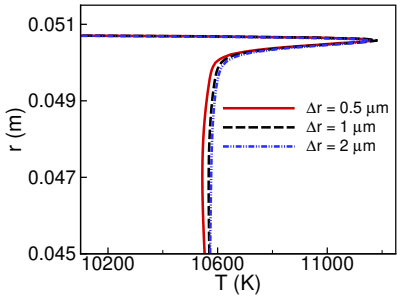

(b) near-wall behavior

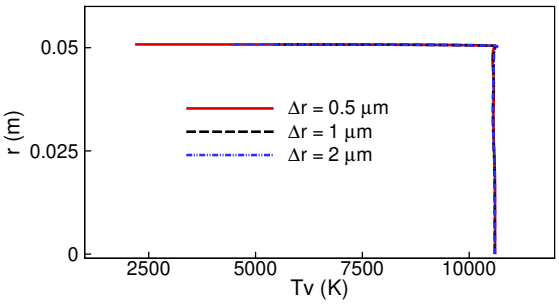

(c) Vibrational-electronic temperature

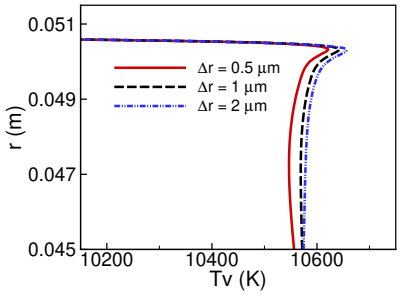

(d) near-wall behavior

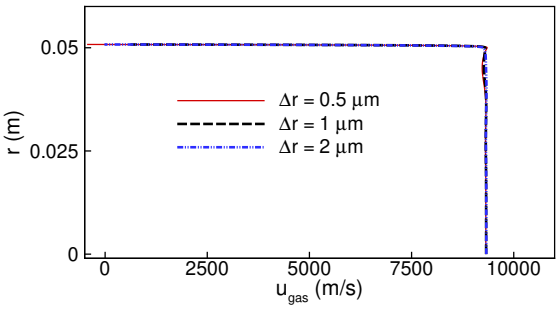

(e) Gas velocity

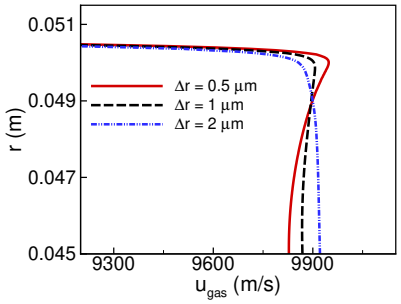

(f) near-wall behavior

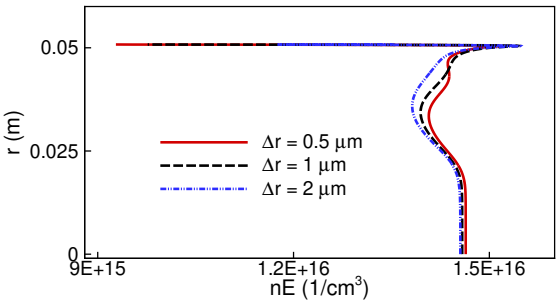

(g) Electron density

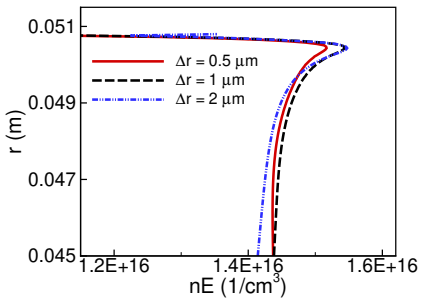

(h) near-wall behavior

Figure 5.4: Radial profiles at t = 10 μs at an axial location, d = 0.5 cm behind the shock front; r = 0 is tube centerline, r = 5.08 cm represents tube walls.

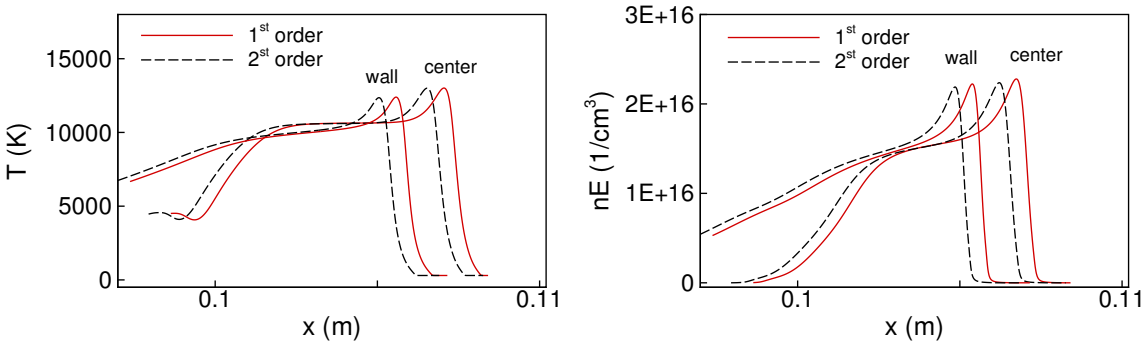

(a) Translational temperature **(b) Electron density**

Figure 5.5: Axial profiles at t = 10 μs with 1st vs. 2nd order time-accurate simulations

5.2.2 Accuracy of temporal discretization scheme

The high speed shock propagation in EAST features extremely fast time-scales associated with various processes, such as convection, viscous interactions and reaction kinetics. In general, such highly unsteady problems are solved using higher order time-integration methods to maintain time-accuracy. However, previous attempts to solve the EAST flow with higher order methods, as described in the Section I, suffered from spurious oscillations. In order to avoid this behavior, a first-order time-accurate method with a highly resolved time-step size ($\Delta t \approx 2ns$) is used as the baseline scheme. The numerical predictions are then compared with those obtained using a second-order accurate time-integration method with same time-step size. The axial profiles of translational temperature and electron density are shown at the centerline and in the near-wall region at r = 5.06 cm in Fig. 5.5. The axial variation of key flow variables behind the shock is practically the same between both schemes, i.e., the differences in absolute values are less than 2%. The difference in the shock front location predicted by second-order vs. first-order time-integration method is within 2-3 λ_∞ at this time which leads to a nominal error of $< 0.5\%$ in the shock speed, i.e., 10.46 km/s vs. 10.51 km/s respectively. As the shock travles further, the difference between the shock front locations predicted by two time-integration schemes can reach up to 3-4 cm, however, the post-shock gas states with respect to the shock front location will stay similar to each other. It is clear that the highly resolved time-step size used here is sufficient to capture the key flow behavior in a time-accurate manner even with first-order temporal discretization. Since the first-order accurate method is computationally cheaper and more stable, further shock propagation is simulated using the same.

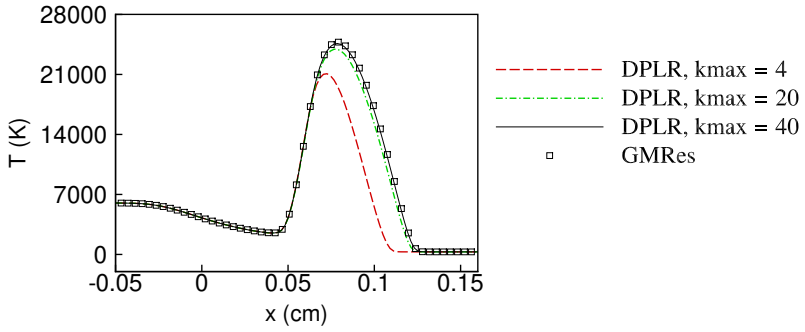

Figure 5.6: Centerline translational temperature at t = 48 ns, DPLR (varied *kmax*) vs. GMRes method

5.2.3 Early flow evolution

Since a long-time numerical integration is necessary for simulating the shock travel from the diaphragm location until the test-section, the numerical method must ensure minimal error at each time-step during the transient period of shock formation. For this reason, a parametric study is performed to opitimize the numerical method as described below.

The implicit system of equations is solved approximately using the DPLR line-relaxation and FMDP point-relaxation methods with varied $kmax$ parameter. The inviscid flux linearization of the implicit operator for these methods is exact only in the case of a first-order discretization. Therefore, the convergence of the linear system is studied for the first-order flux scheme, such that any influence of approximations involved in the implicit operator are minimal. The preconditioned GMRes-based method used here approximates the solution to the linear system more accurately than the FMDP/DPLR methods, and it is taken as the reference method in order to assess the performance of the other methods.

The centerline profile of translational temperature during initial shock development is shown in Fig. 5.6. It is realized that the numerical predictions using the iterative implicit DPLR method are a strong function of the number of relaxation steps (the $kmax$ parameter), and a value of $kmax = 40$ or higher is needed to achieve an accuracy similar to the GMRes solver. Based on this understanding, further simulations are performed using the FMDP and DPLR methods, both with $kmax = 40$, and accuracy of both methods is found to be similar to the GMRes solver.

The computational cost between these methods is significantly different [75]. The preconditioned GMRes method solves the linearized system of equations in a more coupled fashion. The FMDP with $kmax = 40$ gives the same accuracy as the GMRes solver while reducing the computational cost by about 32 times. Since the FMDP method has a point-relaxation scheme while DPLR performs line-relaxations, it is 3 times cheaper than DPLR method, and also, it is free from the numerical bias inherent in the DPLR algorithm. The

DPLR method solves the linear system exactly along the lines drawn in the chosen direction of strong gradients while coupling is only relaxed in the other directions. Generally, the DPLR method is used to solve exactly along lines in the wall-normal direction inside the thin boundary layer, where viscous coupling is strong and the stability condition of the scheme is stringent due to the presence of high aspect ratio cells. However, the EAST shock tube flow is different because here both the shock-normal and the wall-normal directions exhibit extremely steep gradients. It is computationally expensive to solve the system of equations for the EAST flow exactly in both wall-parallel and wall-normal directions; alternatively, choosing one direction over the other, may introduce numerical bias in the system. The FMDP method avoids these issues and still gives a desired level of numerical accuracy. Hence, further simulations are performed using the FMDP method and not with DPLR.

Since a second-order flux-scheme is required to capture the near-wall effects, it is important to assess the convergence of the FMDP time-integration with second-order spatial accuracy as $kmax$ is varied. Three simulations are performed using the values of $kmax$ = 20, 40 and 100 respectively and an early time-evolution of the key flow variables is shown in Fig. 5.7. The start-up shock speed and the initial peak temperatures behind the shock are significantly higher as $kmax$ is increased. These initial differences are large ($\approx$ 10%) but quickly diminish as the shock becomes fully developed. After 10 μs elapsed time, the differences among the three cases become less than 4%.

Further analysis of the shocked gas flow field is presented in Fig. 5.8. The axial profiles of temperature and electron density are plotted for three different $kmax$ values, both at the centerline (i.e., r = 0 cm) and in the near-wall region (i.e., r = 5.06 cm). It can be seen that the flow field at the centerline is more sensitive to $kmax$ variation than the near-wall region. This behavior is as expected; though the axial grid cell sizes are constant across the tube diameter, the grid is significantly stretched in the radial direction from the tube walls to the centerline. Since the wall-normal grid cell spacing at the wall is about 500 times tighter than at the centerline, a lower number of off-diagonal relaxation steps (i.e, a lower value of $kmax = 20$) is sufficient to resolve the flow as accurately as by $kmax = 40$ or 100, whereas, the core flow region with coarser wall-normal spacing requires a larger value of $kmax$ for converging the numerical residuals to similar levels.

It is clear that there is a significant impact of the parameter $kmax$ on the predicted flow behavior. The differences in the centerline flow behavior predicted by $kmax = 40$ and 100 are within 5% of that predicted by $kmax = 20$ while the difference in the computational cost is huge. The computational cost for $kmax = 100$ is about 4 times higher than that for $kmax$ = 20, and 2 times higher than for a $kmax$ of 40. Since the history of shock deceleration along the tube affects the accuracy of the final gas state and the radiation properties measured at the test section, capturing an acurate evolution of the flow field is essential. The FMDP

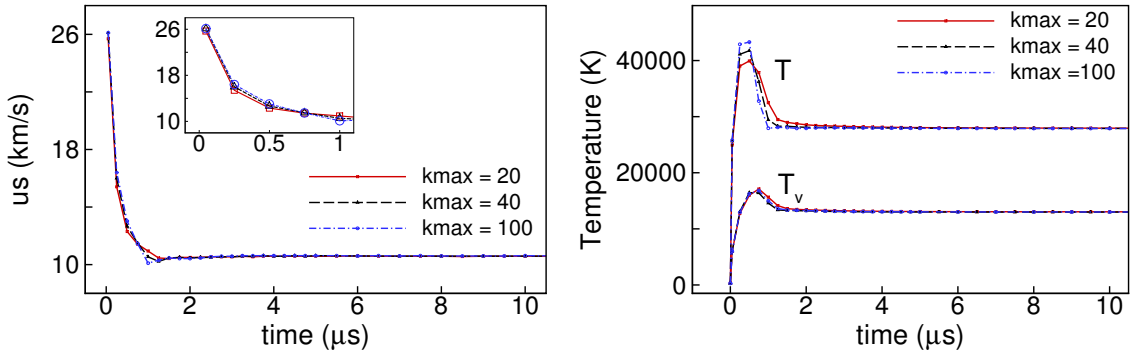

(a) Shock speed (b) Peak temperatures

Figure 5.7: Early flow-field evolution with varied *kmax* parameter

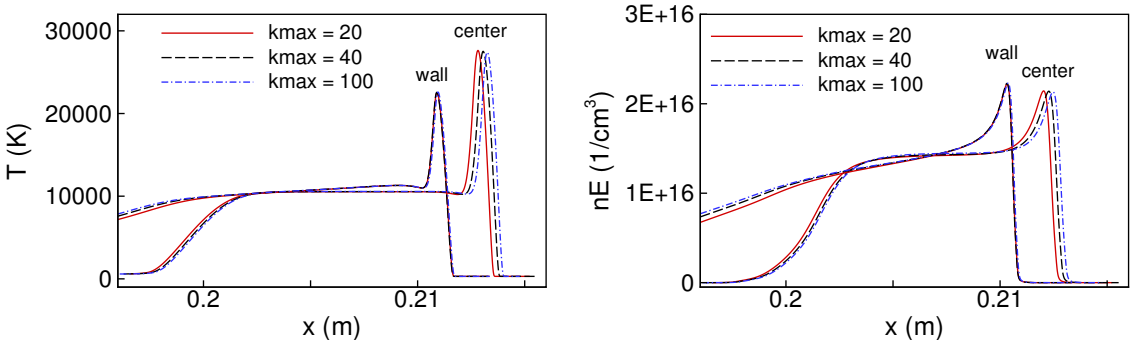

(a) Translational temperature (b) Electron density

Figure 5.8: Axial profiles at t = 20 μs with varied *kmax* parameter

time-integration method with $kmax = 40$ is used for further computations to ensure a fair trade-off between desired levels of accuracy and requirement of the computational resources.

5.2.4 Analysis of the shock tracking

The requirement and implementation of the shock tracking strategy are described in this section. The propagation of the shock front within the computational domain is shown by its space-time evolution in Fig. 5.9, as predicted by a second-order flux reconstruction scheme implemented in a first-order accurate FMDP time-integration with $kmax = 40$. The solid lines represent the left and right boundaries of the domain, whereas the dashed lines represent the extent of the highly refined region as time progresses. The local position of the shock front in the computational grid at discrete time intervals is shown by the square symbols. Since the width of refined region was chosen based on an approximate shock deceleration profile from Ref. [76], the shock is properly accommodated in the refined region during the first 50 μs of shock travel without any re-adjustment of the grid-cell

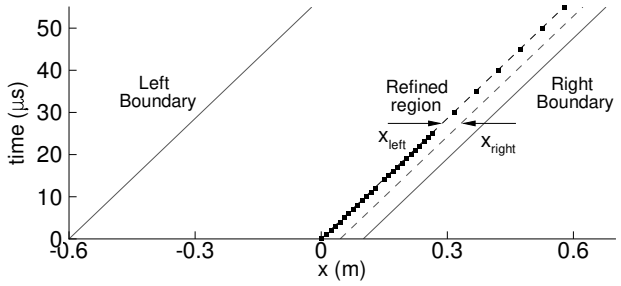

Figure 5.9: Motion of the shock front in the moving-frame; symbols indicate the position of the shock at discrete times.

resolution.

The evolution of the temperature profiles at the centerline is shown in Fig. 5.10. The instantaneous shock speed, u_s, is also indicated. The shock front has decelerated to a speed of 10.44 km/s by the end of 50 μs. The region in the vicinity of the shock front is well resolved during this period. As can be seen in the temperature profiles, the shock front first moves forward in the refined region – the local shock speed is more than 10.5 km/s which is the constant speed of frame motion – and is expected to travel backwards once it is sufficiently decelerated by the boundary layer. For this reason, it is important to track the motion of the shock front within the refined region so that the computational grid can be re-adjusted as required for a well-resolved numerical solution.

The relative motion of the shock front with elapsed time is described in Fig. 5.11. The refined region shown by the dashed lines is periodically modified based on the local shock speed and deceleration, and the expected displacement of the shock front within a short future time-duration. The implementation of this flow dependent tracking strategy ensures that the region in the vicinity of the shock is fully accomodated within the small window of high resolution at all times.

5.2.5 Near equilibrium flow behavior

After the shock has traveled about ten tube diameters, i.e., ≈ 1 m, downstream along the tube, the shock wave attains a nearly constant speed, and therefore, the thermochemical state of the shocked gas evolves more slowly. Based on the findings in the previous sections, the 2D axisymmetric EAST flow field is computed using a second-order spatially accurate and first-order time-accurate implicit time-integration (FMDP method with $kmax = 40$) along with active shock tracking. The solution obtained is presented here at different values of elapsed time. The temperature contours are shown in Fig. 5.12. As the test gas mixture is strongly shocked, both the translational and the vibrational-electronic temperatures rapidly rise to their maximum value just behind the shock front. Additionally, the vibrational-

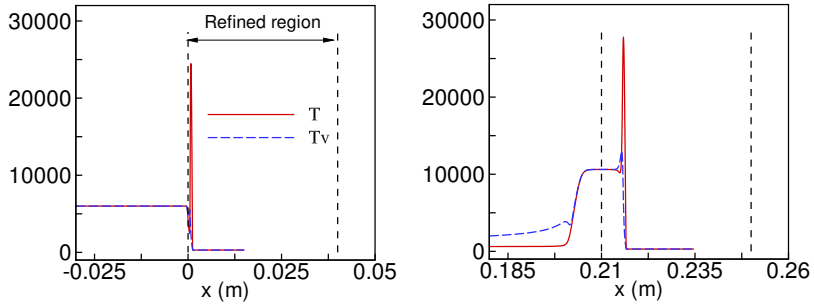

(a) $t = 48$ ns, $u_s = 26.11$ km/s (b) $t = 20\ \mu s$, $u_s = 10.51$ km/s

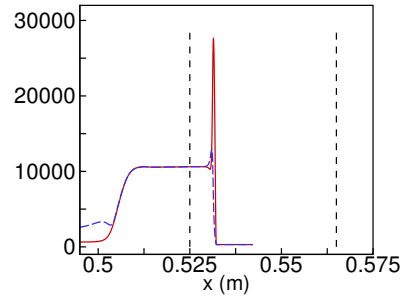

(c) $t = 50\ \mu s$, $u_s = 10.44$ km/s

Figure 5.10: Evolution of the shocked gas relative to the refined region depicted by T and T_v profiles at the centerline of the tube.

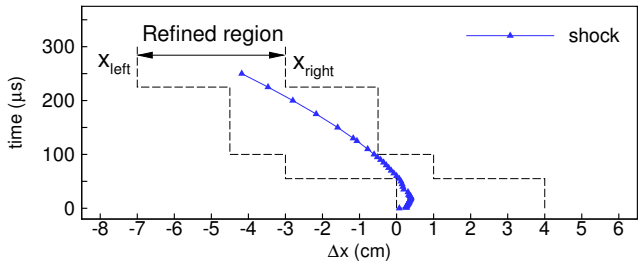

Figure 5.11: Movement of the shock front in the grid with active shock-tracking, (symbols represent the location of the shock front and dashed lines represent the boundaries of the refined region)

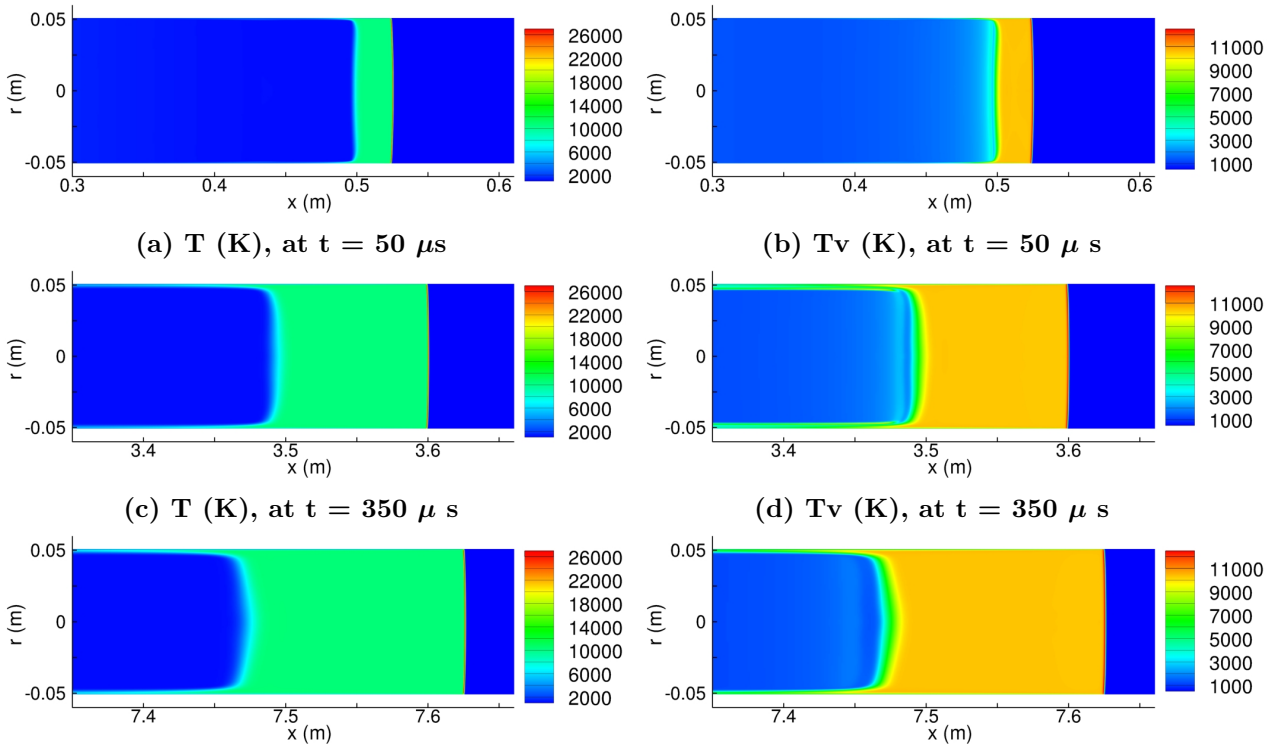

(a) T (K), at t = 50 μs

(b) Tv (K), at t = 50 μ s

(c) T (K), at t = 350 μ s

(d) Tv (K), at t = 350 μ s

(e) T (K), at t = 750 μ s

(f) Tv (K), at t = 750 μ s

Figure 5.12: Evolution of the shocked gas from t = 50 μ s to 750 μ s.

electronic energy modes show significant excitation behind the contact front in the vicinity of the boundary layer. The numerically predicted flow field behind the shock is stable, and there is a slight curving of the shock front near the wall. At time, t = 750 μs, the instantaneous shock speed is approximately 10.1 km/s and the shocked gas region near the centerline has expanded to approximately $15 - 17$ cm.

To obtain further understanding of the flow physics, the time-evolution of the key thermodynamic quantities at the centerline is also analyzed. The centerline profiles of temperature and electron density in the shock frame of reference are plotted in Fig. 5.13. In this notation, the location of the shock front is represented by $x = 0$ at all times, whereas the contact front keeps shifting backwards in the axial direction as the shocked gas mixture expands and different energy modes of the gas equilibrate with each other. At time, t = 50 μs, the temperature and electron densities in the post-shock gas region are significantly high. As the shock front travels downstream along the tube, the shock speed and associated shock strength is continuously reduced due to thermochemical relaxation of the shocked gas and the deceleration of the shock front by the boundary layer. Thus, the test gas at different axial locations in the tube is shocked differently, leading to different post-shock gas states. With increasing elapsed times, the nonequilibrium gas mixture at the shock front expands and interacts with the previously shocked gas behind the shock. This interaction results in a strongly nonequilibrium gas state in the entire shocked gas region and modifies the thermochemical relaxation time-scales in the shocked gas, especially near the contact front. These effects are demonstrated by slowly increasing temperatures and electron densities towards the contact front, as can be seen in Fig. 5.14. Also, the peak of vibrational-electronic temperature is slightly lagged behind that of the translational temperature due to relatively larger relaxation times of the vibrational-electronic modes.

It should be noted that the numerical solutions obtained here are free from spurious oscillations. These simulations are continued further as the shock reaches the EAST test-section located about 8 m downstream of primary diaphragm. The next section presents a detailed analysis of the numerically predicted shocked gas state at the test-section.

5.2.6 Flow field at EAST test-section

The 2D axisymmetric flow field after t = 786 μs elapsed time are discussed in this section. The contours of temperatures and electron density are shown in Fig. 5.15. At this time, the shock front has traveled $\approx$ 7.96 m along the tube from the diaphragm location. The instantaneous shock speed is $\approx$ 10.00 km/s and the shocked gas region has expanded to a width of about 17 cm behind the shock. Since the test-section window in the EAST shock tube is 12 cm wide, extending from x = 7.84 m to 7.96 m, the analysis of numerically predicted flow field at x = 7.96 m can provide insight into the measured flow behavior in

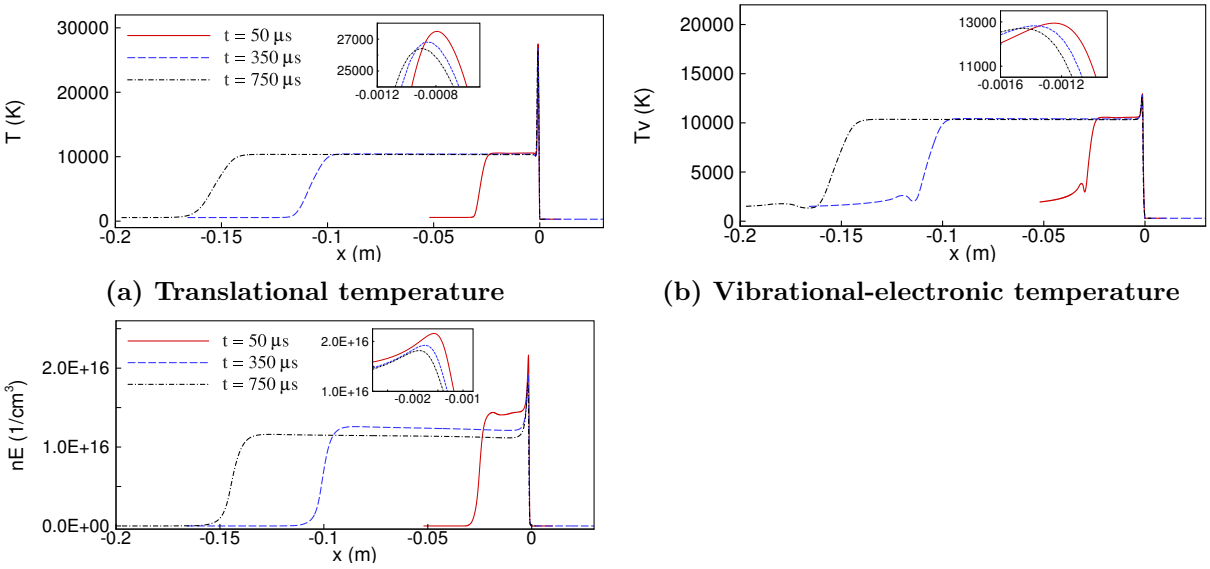

(a) Translational temperature

(b) Vibrational-electronic temperature

(c) Electron density

Figure 5.13: Time evolution of the centerline flow properties plotted in the shock frame of reference

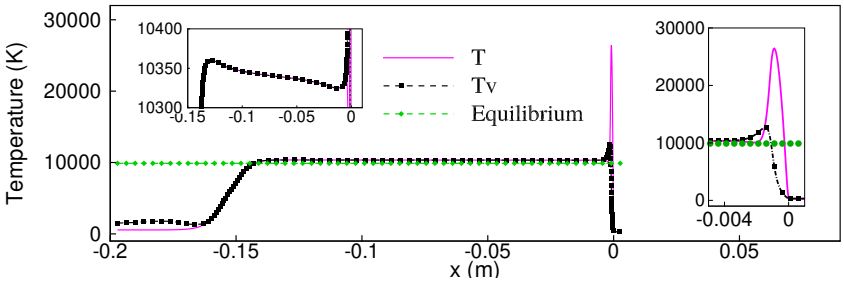

Figure 5.14: Centerline profiles of temperatures at time, t = 750 μs (x = 0 represents the shock front location)

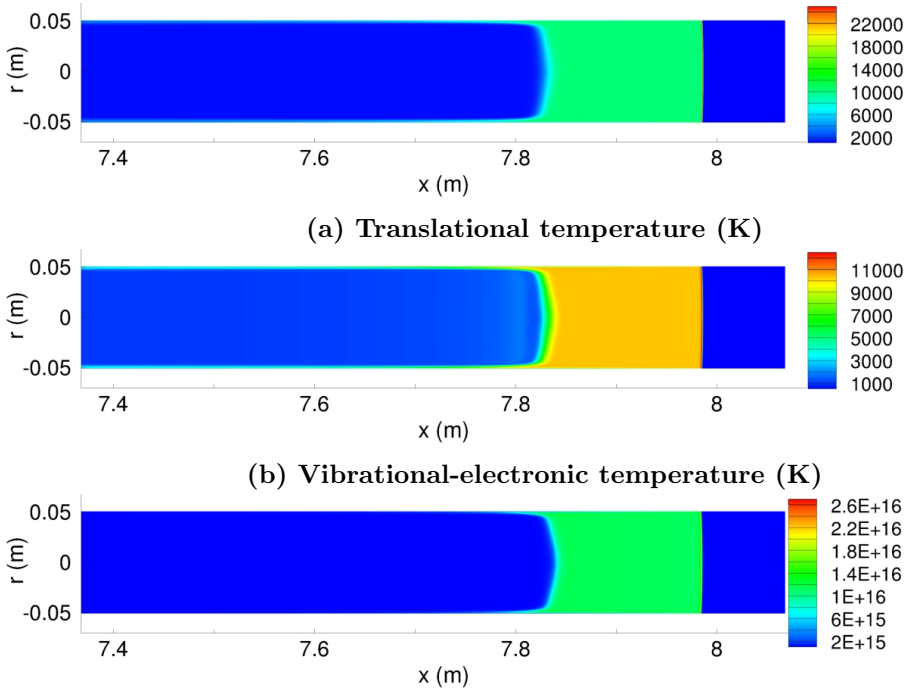

(a) Translational temperature (K)

(b) Vibrational-electronic temperature (K)

(c) Electron number density ($1/cm^3$)

Figure 5.15: Flow field contours at EAST test-section, t = 786 μs

EAST.

With existing measurement techniques, the spectroscopic data gathered in the shock tube experiments can be processed to obtain its spatial variation in the axial direction behind the shock but is radially averaged across the tube-diameter. As described earlier, the boundary layer effects are significant for the high-speed shock waves in EAST, hence the assumption of a radially uniform gas state may introduce errors if the shock tube data is used as it is to infer the rates of thermochemical processes in the shocked gas.

The current goal is to assess the non-uniformity in the flow field across the tube-diameter and quantify its effect both in the 1) nonequilibrium region in the vicinity of the shock front, and 2) the equilibrium region away from the shock. The radial profiles of translational and vibrational-electronic temperatures are shown in Fig. 5.16 at different axial locations. We use a new parameter, d, to represent the distance behind the shock (d = 0 represents the shock front). Going left to right from Fig. 5.16a to 5.16e corresponds to moving a distance of d = 0.07 cm to d = 0.57 cm behind the shock. At a fixed axial location, the shock speed is maximum at the centerline (r = 0 cm) and drops significantly towards the tube wall (r = $\pm$ 5.08 cm). For this reason, the presence of the moving shock front at any axial location is first detected at the tube centerline while the near-wall region receives the shock front after a small time-lag. This behavior is clearly seen in the numerically predicted radial profiles of

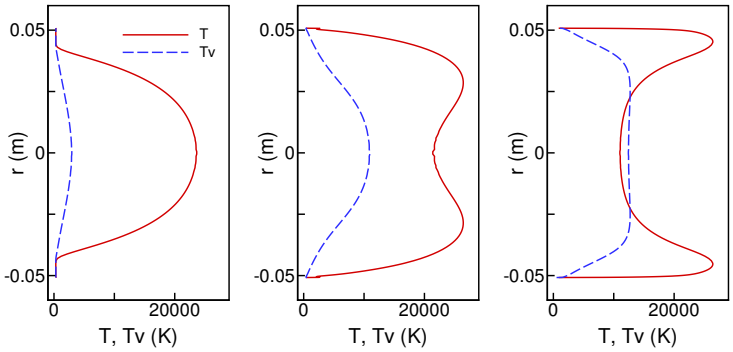

(a) d = 0.07 cm **(b) d = 0.12 cm** **(c) d = 0.17 cm**

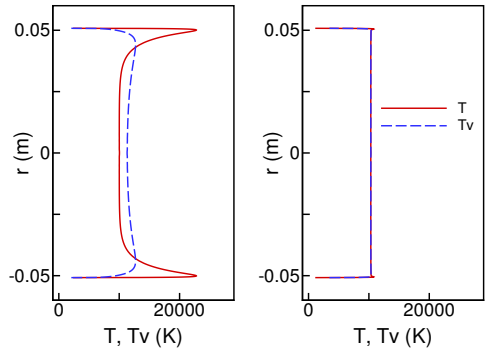

(d) d = 0.22 cm **(e) d = 0.57 cm**

Figure 5.16: Temperature profiles in the nonequilibrium region near shock, *d* is the distance behind the shock-front

temperatures. The translational and vibrational-electronic energy modes exhibit a state of strong nonequilibrium just behind the shock front (i.e., d = 0.07 cm). As the distance from the shock front location is increased from d = 0.07 cm to d = 0.57 cm, the presence of the shock is felt in a wider region across the tube-diameter leading to higher gas temperatures. The translational and vibrational-electronic energy modes first start to equilibrate at the centerline, but a significant portion of the tube away from the centerline stays under strong thermal nonequilibrium until d = 0.22 cm. The radial nonuniformities and the extent of nonequilibrium between two energy modes diminish with increasing distance behind the shock.

After d = 0.57 cm onwards, the gas state becomes almost uniform in the radial direction where the nonuniformities in the flow properties get confined in a thin near-wall region. The radial profiles of gas velocity, temperatures and electron densities extracted at d = 0.27 cm, 0.57 cm and 10.07 cm are shown in Fig. 5.17. With increasing distances behind the shock front, the core flow becomes more uniform. The near wall profiles for key flow variables are shown in Fig. 5.18 , the radial data is extracted at six axial locations ranging from d =

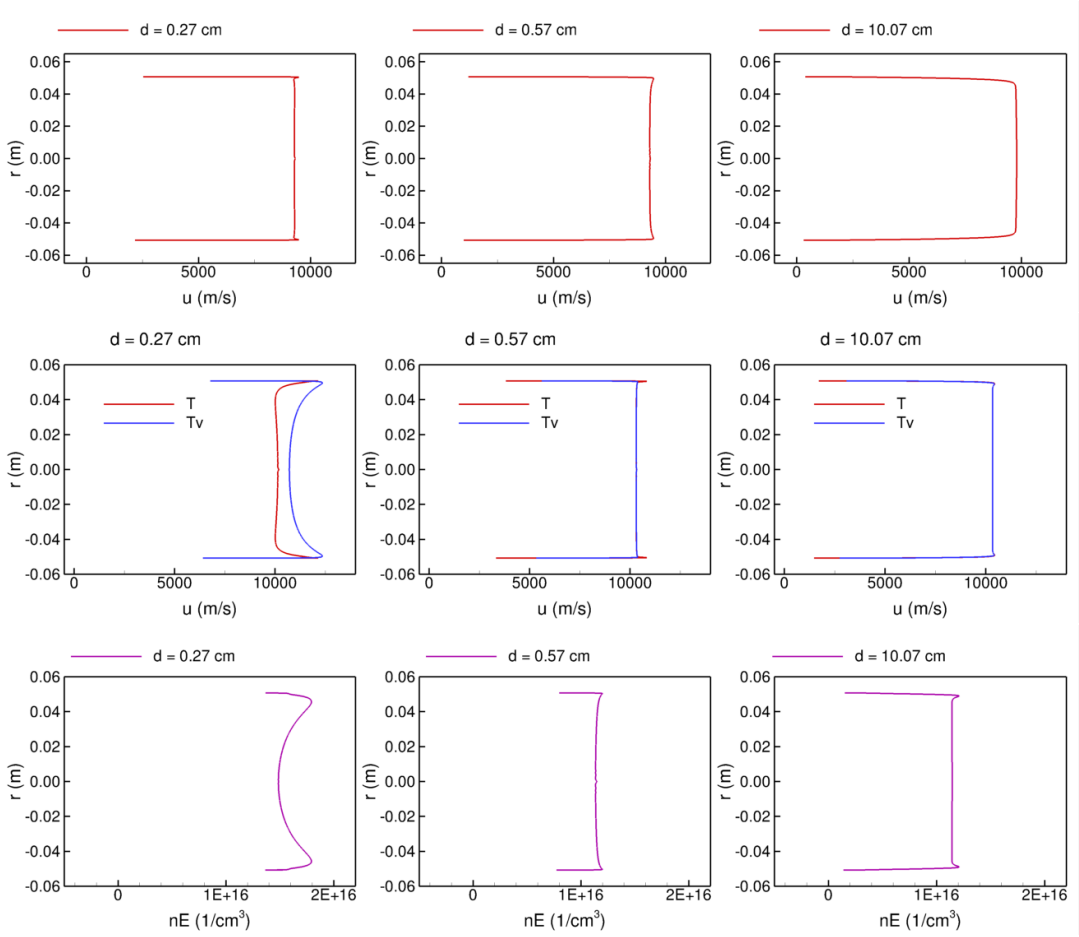

Figure 5.17: Radial profiles of gas velocity, temperaturs and electron density plotted at three axial locations behind the shock, *d* is the distance behind the shock-front; please read the x-axis title on TTv plots as Temperature (K)

0.57 cm to d = 25.07 cm behind the shock front. The contact front is located at d = 17.07 cm which separates the shocked test gas and the expanded driver gas. With increasing distances from the shock front until the contact front, the shocked gas relaxes and expands, and the gradients in the near-wall region are smoothened by viscous diffusion. Beyond the contact front, i.e., d = 17.07 cm onwards, the gas properties correspond to expanding driver gas – the temperatures and electron densities increase in the near-wall region as the gas stagnates at the wall while the core flow is relatively cold and uniform.

Using this fluid dynamic data at the test-section, the boundary layer thickness based on 99% of centerline axial-velocity (i.e., δ_{99}) is calculated at different axial locations behind the shock. This is shown in Fig. 5.19, where d = 0 represents the shock front location. The boundary layer grows behind the shock until the contact front (from d = 0 to d = 17.07 cm) from zero to a maximum thickness of $\approx 6\ mm$. This happens because the test gas is

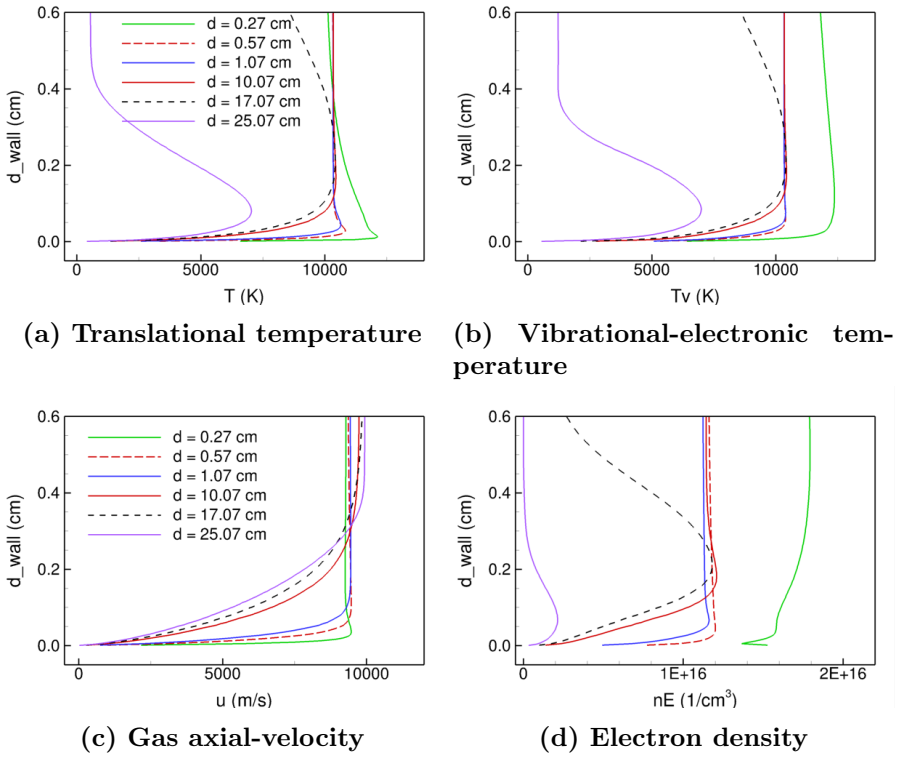

(a) Translational temperature **(b) Vibrational-electronic temperature**

(c) Gas axial-velocity **(d) Electron density**

Figure 5.18: Near-wall variation of shocked gas properties plotted at various axial locations (d = 0.27 cm to 25.07 cm) behind the shock front, (*d_wall* represents the radial distance from the wall)

accelerated by the shock. Beyond the contact front, boundary layer thickness decreases in the expanded driver gas region as the gas velocity decreases.

Hence, the two-dimensional axisymmetric solutions for the high-enthalpy shock propagation in the EAST shock tube are obtained using an optimized simulation approach. The computational cost is reduced by approximately three orders of magnitude by solving the flow in a moving frame of reference as compared that in a fixed frame of reference. A time-accurate evolution of the shocked gas flow is obtained until the shock reaches at EAST test-section. Since the diaphragm is assumped to be fully open at the beginning of the simulations, the numerically predicted shock starts at a large speed, and then quickly decelerates to a near-constant speed based on the excitation, interaction and relaxation of different energy modes of the gas. A laminar boundary layer grows behind the shock front as it travels along the tube and the shocked gas is decelerated near the wall. Shocked gas properties are thoroughly analyzed in both axial and radial directions. The test gas behind the shock front first relaxes towards thermochemical equilibrium corresponding to instantaneous shock speed, and then deviates from the equilibrium as it interacts with pre-

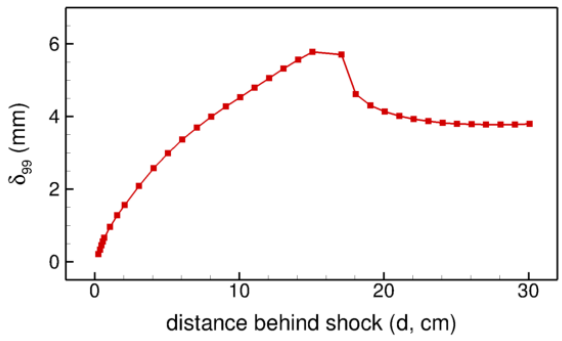

Figure 5.19: Boundary layer thickness (δ_{99}) behind the shock, d is the distance behind the shock-front

viously shocked downstream gas. This is demonstarted by the axial profiles of temperatures and electron density behind the shock. The maximum boundary layer growth after 8 m of shock travel is $\approx 6\ mm$. The CFD data obtained here are the first-ever numerically stable predictions of shocked gas behavior at EAST test-section enabling for an improved understanding of the shock tube flow physics. These numerical predictions can be validated against measured quantities in the experiments to identify the scope of further modeling improvements. Also, quantities useful for heating calculations, such as the boundary layer growth rate and the radial variation of shocked gas properties, can also be quantified, which are difficult to measure in tests.

The numerical analyses presented here provide a deeper insight into the high enthalpy gas dynamics in Air. The next step is to understand the numerically predicted gas behavior over a range of flow conditions, and assess the performance of current CFD modeling against experimental observations. This is presented in the following chapter.

Chapter 6

High enthalpy shocks in Nitrogen

The full-tube EAST calculations presented in the previous chapter provided a deeper insight into the high enthalpy gas dynamics in air. The next goal is to understand the numerically predicted gas behavior over a range of flow conditions, and assess the performance of current CFD modeling against experimental observations. Recently, Brandis & Cruden [1] performed nitrogen shock experiments at shock speeds ranging from about 6 km/s to 11 km/s. Having pure nitrogen as the test gas greatly simplifies the reaction kinetics, which makes this set of experiments a more suitable candidate for the validation of CFD simulations. In this chapter, six of these nitrogen experiments are simulated with an improved modeling of the electron-impact ionization process, as decribed in Chatper 2. This means that the electron-impact ionization rates are calculated by using a governing temperature corresponding to the gas internal energy modes, i.e. T_v; and the corresponding loss in the electron-translational energy is deducted from the mixture's internal energy.

The initial conditions are described in the next section followed by a brief discussion on the performance of active-shock tracking in each case. The CFD predicted gas behavior at different test conditions is investigated in several ways. Gas dynamics during the shock formation process is explained briefly, while the emphasis is on the near-equilibrium gas behavior beyond 2 m of shock travel and at the test-section. The hot gas properties are analyzed at different axial locations along the shock tube and the differences in gas kinetic behavior are demonstrated for varied shock speeds. Numerically predicted gas properties are also compared with the EAST data.

6.1 Initial conditions

The test gas is pure nitrogen at freestream temperature, T_∞ = 300 K, and pressure, p_∞ = 0.2 Torr (26.67 N/m^2), in all cases. The driver gas initial conditions are adjusted to generate desired shock speed (u_s) at the test-section, as described in Table 6.1 along with

Table 6.1: Driver gas properties for different test cases

Case no.	Pressure p (N/m^2)	Density ρ (kg/m^3)	Temperature T (K)	Frame-speed u_f (km/s)	Shock speed u_s (km/s)
1	5.05×10^6	1.105	2200	6	6.04
2	6.43×10^6	1.105	2800	7	6.63
3	8.03×10^6	1.105	3500	8	7.7
4	10.33×10^6	1.105	4500	9	8.7
5	12.63×10^6	1.105	5500	9.9	9.62
6	15.62×10^6	1.105	6800	11	10.32

the moving-frame speed, u_f, in each case.

6.2 Early flow evolution

The diaphragm breaks at time $t = 0$, and the driver gas energy is quickly absorbed by the translational-rotational energy modes of the test gas, leading to large values of start-up speeds and gas temperatures. For the test conditions considered here, the shock start-up speeds reach up to approximately 15-28 km/s with peak gas temperatures of 20,000 K to 40,000 K. However, these high values are merely an artifact of the simplified diaphragm rupture process in CFD, which in reality is a finite-time, three-dimensional process. For current purposes, this modeling works well since the initial translational energy of the gas is quickly re-distributed into its internal energy modes within the first 10-15 cm of shock travel, and the effects of large start-up speeds are diminished. From the simulation point of view, this demands the validity of the physical models and the stablity of the numerical algorithms during these extreme conditions which was studied by Chandel et al. [75].

The variations of peak temperature and gas axial velocity for the first 20 cm of shock travel are shown in Figs. 6.1 and 6.2, respectively. Since the shock formation process and early evolution of the shocked flow are qualitatively similar in all these simulations, only the lowest (case 1) and the highest shock speed (case 6) results are shown here. The symbols represent CFD data computed at discrete locations of the shock front. The instantaneous shock speed in CFD is represented by u_s. The shock start-up speeds just after the diaphragm burst are 14.84 km/s and 27.78 km/s respectively, which are reduced to 6.24 km/s and 11.16 km/s, after $\approx$ 20 cm of shock travel. The peak temperatures in the shocked gas region also drop significantly within this time period. As the shock front moves further downstream, the shocked gas energy is updated due to chemical kinetics, and viscous interactions with the boundary layer. The shock front attains a near-constant speed within 1-2 m of shock travel; beyond this stage, the shocked gas state evolves comparatively slowly. This is referred to as the *near-equilibrium* shock behavior. The shock speeds observed at the test-section for case

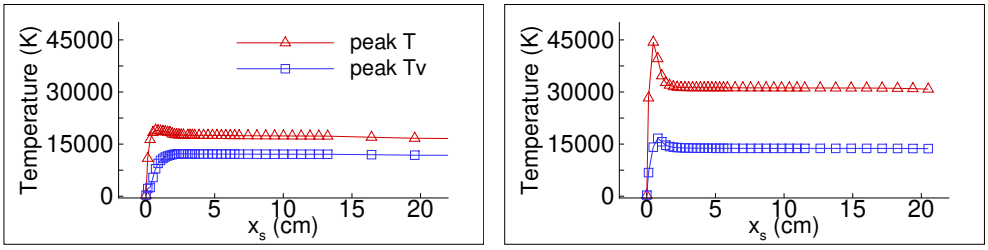

(a) $u_s = 6.24$ km/s (b) $u_s = 11.16$ km/s

Figure 6.1: Peak post-shock temperatures at discrete locations (shown by symbols) along the tube

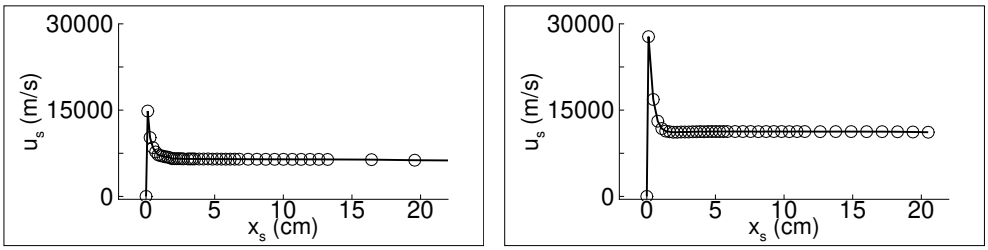

(a) $u_s = 6.24$ km/s (b) $u_s = 11.16$ km/s

Figure 6.2: Shock speed at discrete locations (shown by symbols) along the tube

1 & 4 are 6.04 km/s and 10.32 km/s respectively. The early evolution of the shocked flow in 10 km/s air shock was investigated in previous chapter – nitrogen shocks behave in a similar manner. The focus in the current chapter is on understanding the shock-formation process and near-equilibrium gas behavior beyond 2 m of shock travel. The next section gives a quick overview of the shock tracking in these simulations, the discussion is then shifted to the numerically predicted flow-field.

6.3 Shock tracking

As mentioned in the previous chapters, the moving-frame of reference travels at a constant speed whereas the shock front gets decelerated by the boundary layer. Hence, based on the instantaneous shock speed, the shock front moves either backward or forward within the computational grid. Using the active-shock tracking, the heavily refined region is periodically adjusted to contain the shock front during the entire shock propagation. The movement of the shock within the refined region is shown in Fig. 6.3, here Δx is the relative displacement with respect to the initial computational grid when the refined region extends from $\Delta x = 0$ to 4 cm. The shock front is at $\Delta x = 0$, at time, $t = 0$. The shock start-up speeds are much higher in CFD, hence, during first 20-50 μs the shock front moves

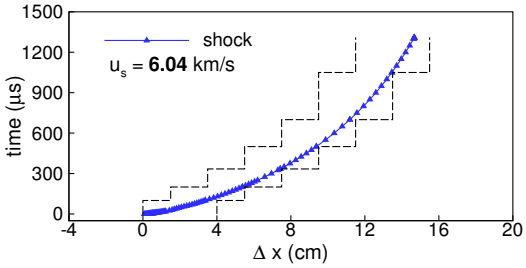

(a) Case 1, $u_s = 6.04$ km/s

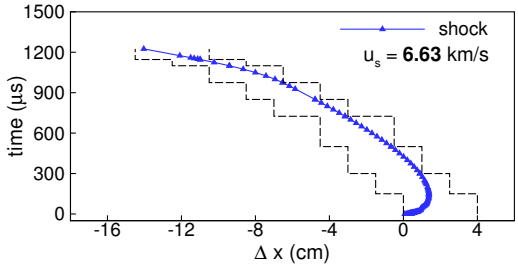

(b) Case 2, $u_s = 6.88$ km/s

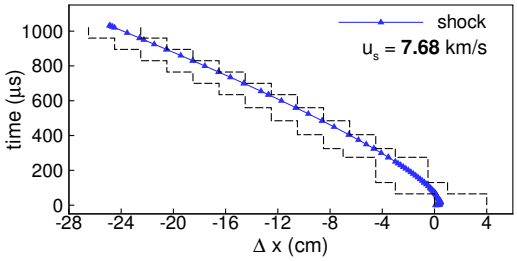

(c) Case 3, $u_s = 7.68$ km/s

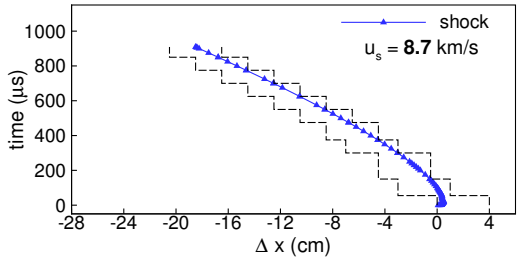

(d) Case 4, $u_s = 8.7$ km/s

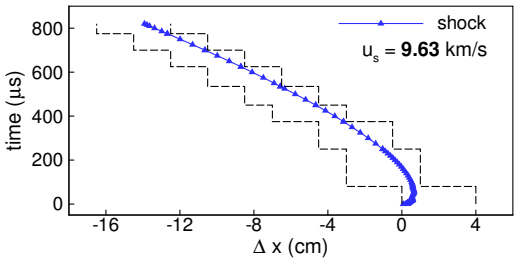

(e) Case 5, $u_s = 9.62$ km/s

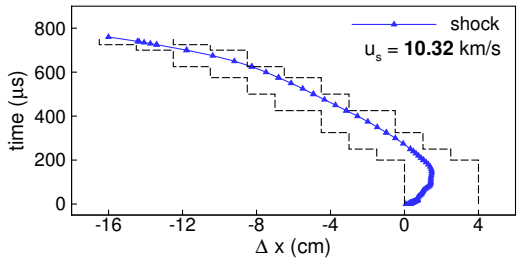

(f) Case 6, $u_s = 10.32$ km/s

Figure 6.3: Movement of the shock front in the grid with active shock-tracking for nitrogen shocks, (symbols represent the location of the shock front and dashed lines represent the boundaries of the refined region)

forward relative to the grid, in all cases. For cases 2 to 6, the moving-frame speeds are higher than the shock speed at the test-section (see Table 6.1, therefore, once the shock has fully formed, it keeps moving backwards in the moving-frame. For case 1, the moving-frame speed is slightly smaller than the near-equilibrium shock speed, therefore, the shock front keeps moving forward relative to the moving-frame. The boundaries of the refined region are adjusted throughout the simulation such that the shock front is well resolved at all times.

6.4 Shock start-up process

The diaphragm rupturing in the shock tubes is a transient, three-dimensional process, but it is modeled as an instantaneous, two-dimensional axisymmetric mechanism in CFD. Hence, the energy transfer from the driver gas to the test gas is artificially large and much faster at the beginning of the simulations. As the thermochemical processes start, the gas behavior in CFD becomes more realistic with increasing elapsed times. However, it is important that the numerical methods predict a thermodynamically consistent gas state at all times. In this section, the fluctuating pressure-field behind the shock is studied to understand the behavior of weak compression waves in the hot gas region. The pressure contours during elapsed time, t = 20-100 μs, are plotted for cases 1, 3, 4 and 5. The color contour is chosen such that the minimum and maximum pressure values are within $\pm$10% of the corresponding equlibrium pressure at that shock-speed, i.e., the minimum pressure value shown in the contours is 0.9 times of the post-shock equilibrium pressure and the maximum value is 1.1 times of the equilibrium value. The time-evolution of the pressure-field is shown in Fig. 6.4 and 6.5 respectively, in groups of cases 1 and 3, and cases 4 and 5. This grouping is done because the shock speed at the test-section is less than 8 km/s for cases 1 and 3, hence, the behavior of $<$ 8 km/s shocks is first understood in Fig. 6.4, followed by the 8-10 km/s shocks in cases 4 and 5. The contours are shown in the shock-frame of reference, where $xs = 0$ represents the shock front location. The shock front location in the laboratory frame, x_{shock}, the instantaneous shock speed, u_s, and the elapsed time, t, are also mentioned in the plots.

The pressure-field behind these shocks is qualitatively similar while the time-rates of the thermochemical evolution of gas state are different. The case 1, with the lowest shock speed, has the smallest energy in the flow. Hence, the post-shock gas pressure stays higher than equilibrium for a much longer time than in case 3. As the time progresses, weak compression waves within the hot gas region (qualitatively represented by the red color in the contours, i.e., pressure values greater than 10% of the equilibrium pressure) move from the shock tube centerline towards the walls. These pressure waves are reflected by the walls, to interact with the core flow while freshly formed compression waves keep hitting and reflecting at the walls in a periodic manner. This behavior is better understood via animation, the flow contours shown here provide just a rough idea of this transient process. At elapsed time, t = 100 μs, the shock in the case 3 has developed an about 5 cm wide region with a significantly uniform core flow at equilibrium pressure, whereas the post-shock pressure is still far from equilibrium in case 1. This is also expected since the lower energy shock has much slower reaction kinetics, hence, the relaxation of the hot gas to the equilibrium conditions requires a longer time. Due to higher energy present in the flow, the flow-field evolves much faster

at higher speeds (8-10 km/s) and the pressure values are closer to the equilibrium value in the majority of the inviscid core flow region. The flow behavior for cases 4 and 5, at higher shock speeds, is qualitatively similar to the low shock speed cases except that the compression waves are now stronger and the thermochemical relaxation processes are much faster. Hence, the post-shock gas is significantly closer to the equilibrium gas state, at just after the elapsed time, $t \approx 50$ μs onwards.

6.5 Flow behavior at ≈ 2 m

In this section, we analyze the shocked gas behavior at different shock speeds after 2 m of shock travel. The nomenclature for each case follows from Table 6.1, (i.e., case numbers 1, 2, 5 and 6 have a CFD predicted shock speed of 6.04 km/s, 6.63 km/s, 9.62 km/s and 10.32 km/s respectively, at the test-section). We first analyze the temperature field for each case. The contours of T and T_v are shown in Fig. 6.6 and 6.8 respectively, followed by their axial profiles extracted at four different radial locations across the tube. The tube centerline is represented by $r = 0$ and tube walls are located at $r = 5.08$ cm. We extract the axial data at the centerline, and at $r = 4.8$ cm which is an indicative of the end of the core flow region. The axial profiles are also shown at $r = 5.02$ cm and $r = 5.06$ cm to understand the near-wall flow behavior. This is shown in Fig. 6.7 and 6.9. The dashed lines represent equilibrium gas properties corresponding to the instantaneous shock speed, u_s, computed at the centerline.

Gas equilibrium properties are calculated using NASA's Chemical Equilibrium with Applications (CEA) code developed by Gordon & McBride [63]. The gas temperatures rise just behind the shock to their peak value and then relax toward their equilibrium values in two different ways. For lower shock speeds ($<$ 8 km/s, i.e., case 1 & 2), the translational-rotational and vibrational-electronic-electron energy modes do not achieve equilibrium within this distance of shock travel. At higher speeds ($>$ 8 km/s, i.e., case 5 & 6), the shocked gas temperatures first relax toward their equilibrium values and then slowly increase toward the contact front. At higher shock speeds, the relaxation to equilibrium is achieved over a shorter distance of shock travel. As mentioned earlier, the motion of the shock front is decelerated by chemical kinetics and viscous interactions, hence, the test gas is shocked at reducing strengths resulting in decreasing post-shock temperatures along the tube. Therefore, as the shocked gas at a particular axial location interacts with previously shocked gas, the temperatures and associated reaction rates increase towards the contact front. This is also demonstrated in the electron number densities behind the shock which are shown in Fig. 6.10 and 6.11 .

Next, we investigate the gas velocity (u_{gas}) at different radial locations. As seen in

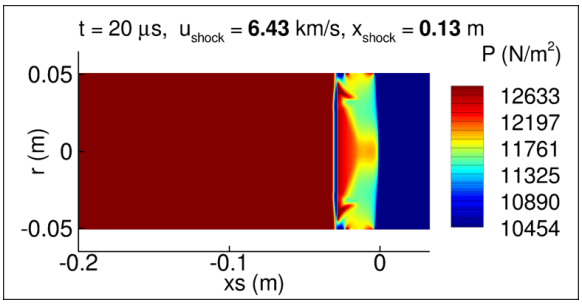

(a) Case 1, $t = 20\ \mu s$

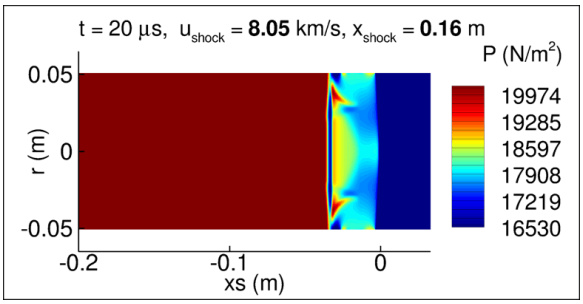

(b) Case 3, $t = 20\ \mu s$

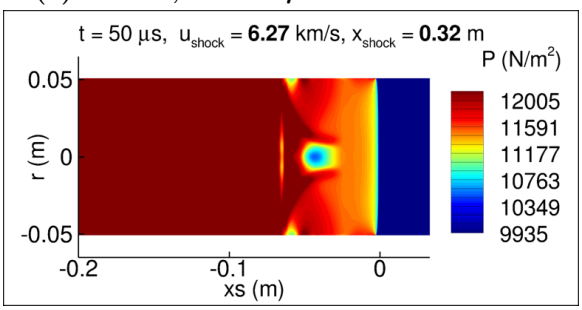

(c) Case 1, $t = 50\ \mu s$

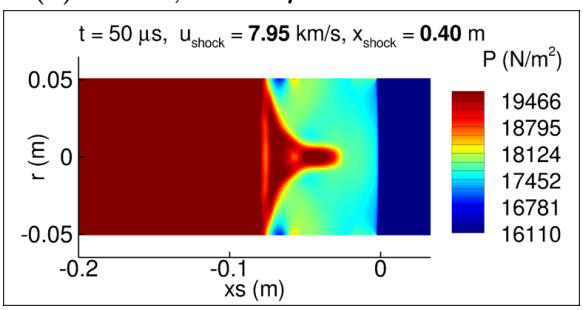

(d) Case 3, $t = 50\ \mu s$

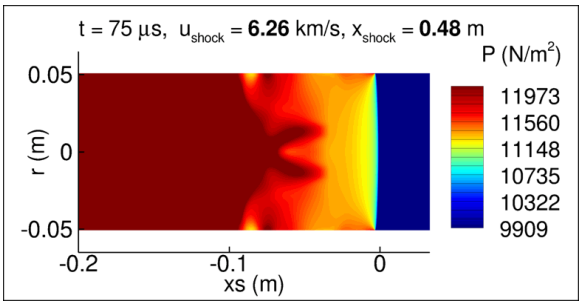

(e) Case 1, $t = 75\ \mu s$

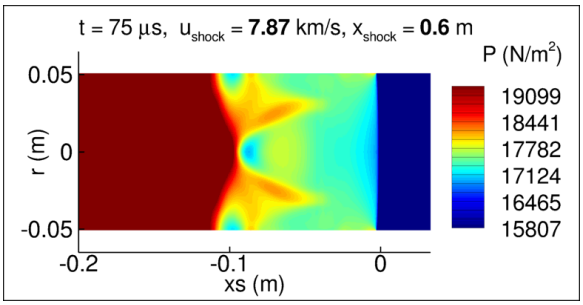

(f) Case 3, $t = 75\ \mu s$

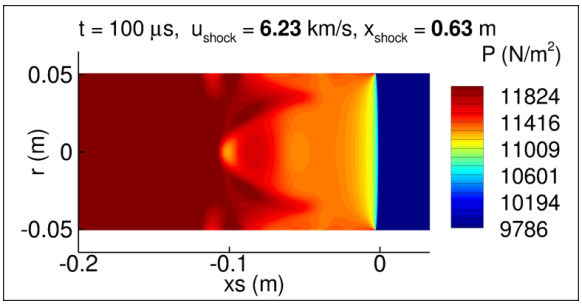

(g) Case 1, $t = 100\ \mu s$

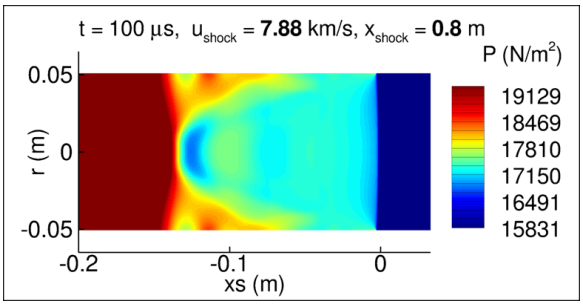

(h) Case 3, $t = 100\ \mu s$

Figure 6.4: Pressure field at lower shock speeds, $xs = 0$ represents the shock front location

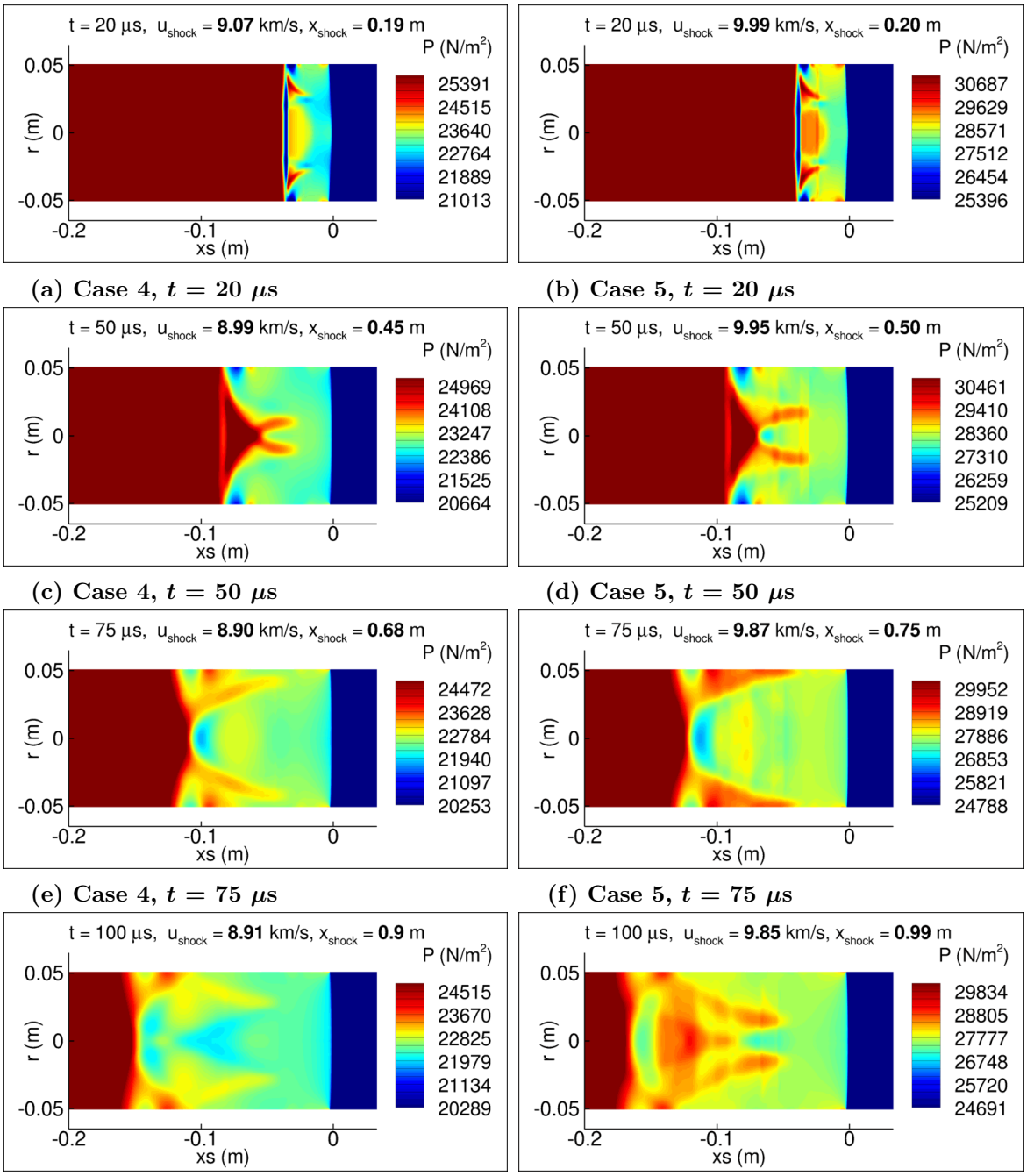

(a) Case 4, $t = 20$ μs

(b) Case 5, $t = 20$ μs

(c) Case 4, $t = 50$ μs

(d) Case 5, $t = 50$ μs

(e) Case 4, $t = 75$ μs

(f) Case 5, $t = 75$ μs

(g) Case 4, $t = 100$ μs

(h) Case 5, $t = 100$ μs

Figure 6.5: Pressure field at higher shock speeds, $xs = 0$ represents the shock front location

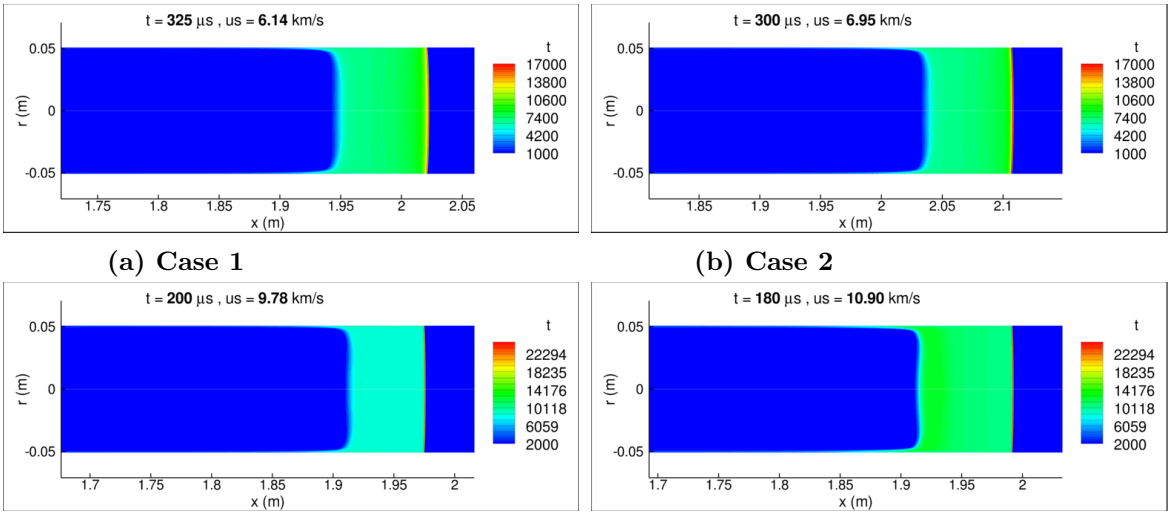

(a) Case 1 (b) Case 2

(c) Case 5 (d) Case 6

Figure 6.6: Translational temperature, $x_s \approx 2$ m (r = 0 is centerline, r = ± 5.08 cm represents tube-walls)

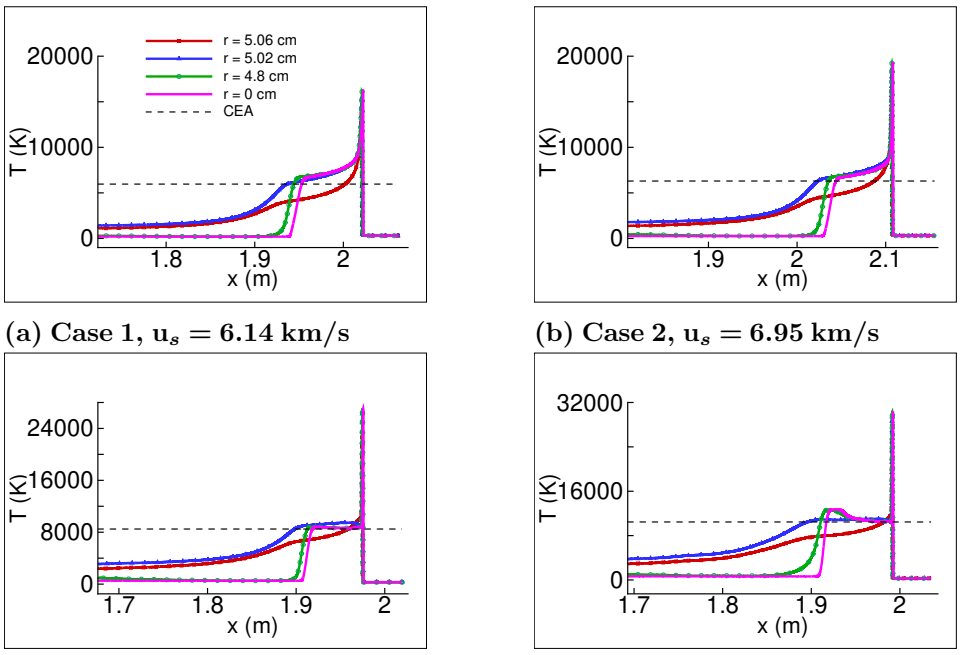

(a) Case 1, $u_s = 6.14$ km/s (b) Case 2, $u_s = 6.95$ km/s

(c) Case 5, $u_s = 9.78$ km/s (d) Case 6, $u_s = 10.9$ km/s

Figure 6.7: Translational temperature profiles at different radial locations across the tube, $x_s \approx 2$ m

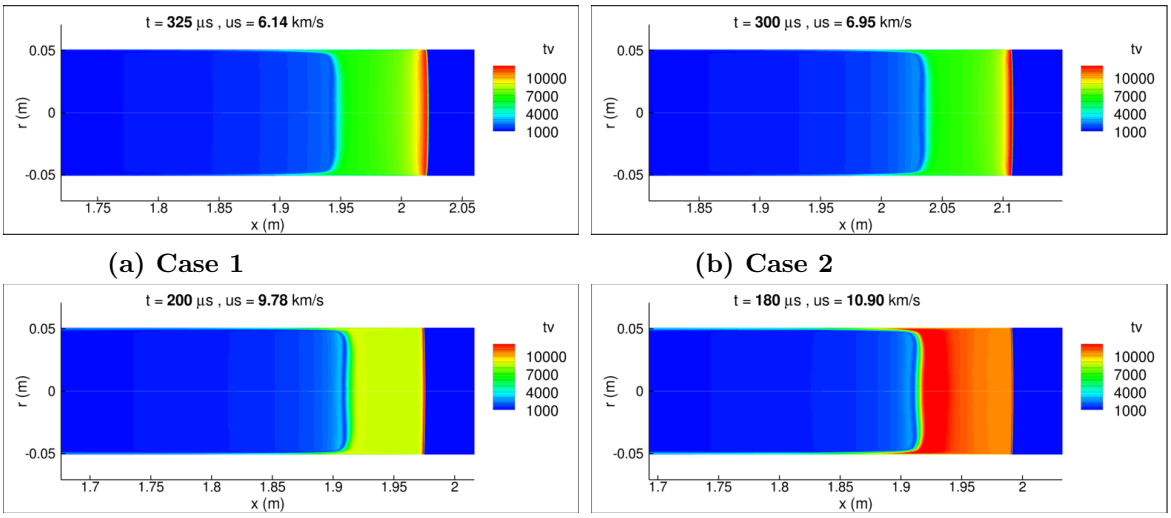

(a) Case 1 (b) Case 2

(c) Case 5 (d) Case 6

Figure 6.8: Vibrational-electronic temperature, $x_s \approx 2$ m (r = 0 is centerline, r = ± 5.08 cm represents tube-walls)

Fig. 6.12 , the core flow region has an almost constant post-shock gas velocity whereas near-wall gas velocities quickly drop behind the shock due to the presence of the boundary layer. The thermochemical evolution of the gas is qualitatively similar as the shock front travels from 2 m to ≈ 8 m but the rate at which the gas state evolves varies in each test case. This is briefly discussed in the following section with an emphasis on understanding the flow behavior at the test-section.

6.6 Flow-field at EAST test section

In this section, we investigate the behavior of the key flow variables, both in the axial and radial directions. The test-section window starts at about 7.865 m, and is 12 cm wide, therefore, we analyze the shocked gas state when the shock front is at $x_s \approx 7.98$ m to understand the gas dynamics predicted by CFD vs. that observed in EAST.

6.6.1 Gas temperatures

We first analyze the extent of equilibrium between the two energy modes of the gas (represented by temperatures T and T_v) in the shocked gas region. Fig. 6.13 shows the axial profiles of T and T_v in the core flow region. The dashed lines represent the corresponding equilibrium temperature. The flow behavior for high shock speeds (case 5 & 6) is similar to that after 2 m of shock travel. The gas temperatures rise toward the contact front to values up to 10-30% higher than equilibrium. The low speed cases (1 & 2) are closer to

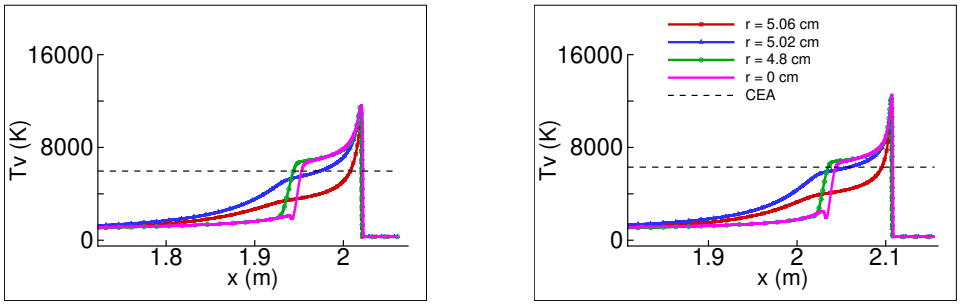

(a) Case 1, $u_s = 6.14$ km/s

(b) Case 2, $u_s = 6.95$ km/s

(c) Case 5, $u_s = 9.78$ km/s

(d) Case 6, $u_s = 10.9$ km/s

Figure 6.9: Vibrational-electronic temperature profiles at different radial locations across the tube, $x_s \approx 2$ m

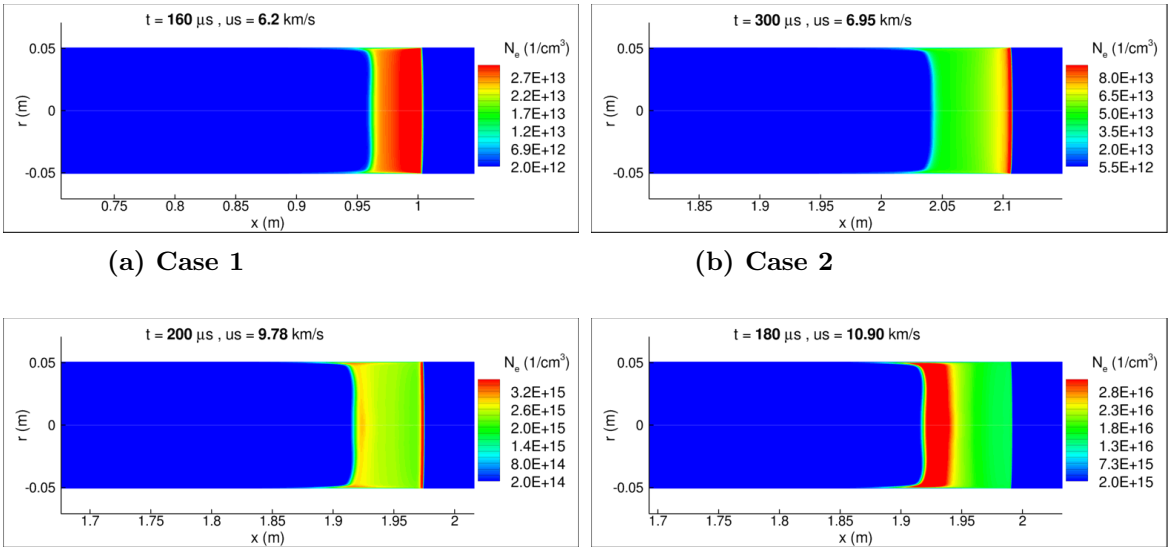

(a) Case 1

(b) Case 2

(c) Case 5

(d) Case 6

Figure 6.10: Electron density, $x_s \approx 2$ m (r = 0 is centerline, r = ± 5.08 cm represents tube-walls)

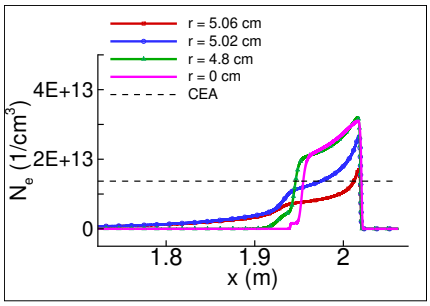

(a) Case 1, $u_s = 6.14$ km/s

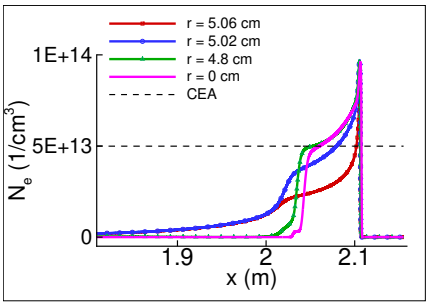

(b) Case 2, $u_s = 6.95$ km/s

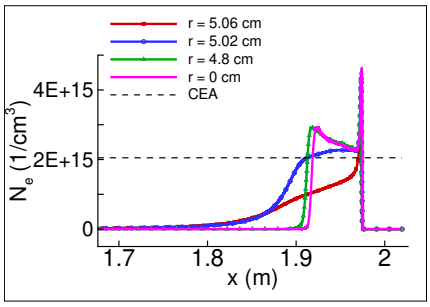

(c) Case 5, $u_s = 9.78$ km/s

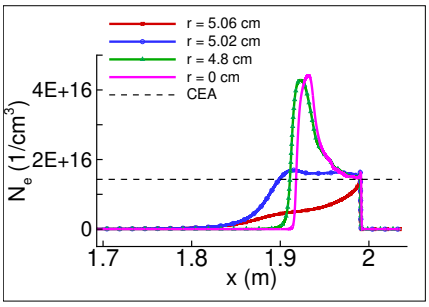

(d) Case 6, $u_s = 10.9$ km/s

Figure 6.11: Electronic density profiles, $x_s \approx 2$ m

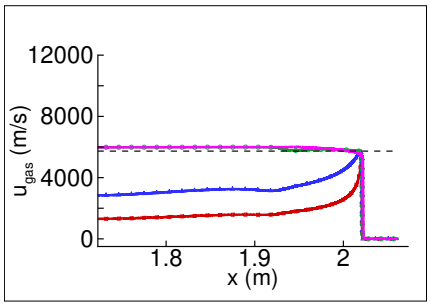

(a) Case 1, $u_s = 6.14$ km/s

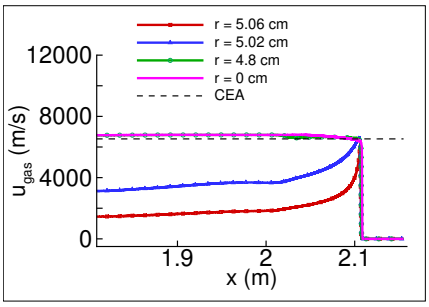

(b) Case 2, $u_s = 6.95$ km/s

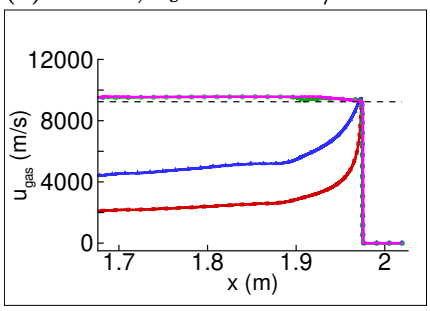

(c) Case 5, $u_s = 9.78$ km/s

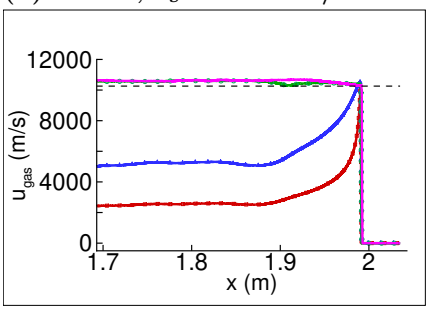

(d) Case 6, $u_s = 10.9$ km/s

Figure 6.12: Gas velocity profiles, $x_s \approx 2$ m

equilibrium values than after 2 m of shock travel (Fig. 6.7, 6.9). However, the gas state is still approaching thermal equilibrium as can be seen in the zoomed-in plots. The gas temperatures at the centerline are about 10% higher than the equilibrium values.

Fig. 6.14 describes the axial behavior near the wall. The gas temperatures are closer to equilibrium and drop significantly behind the shock front. The radial variation in gas temperature is also significant from $r = 5.02$ cm to $r = 5.06$ cm, which is 2 cm away from the wall surface. The gas temperatures at $r = 5.06$ cm are about 30% lower than equilibrium for low speeds, and about 15-20% lower for high speeds. This trend is expected since the gas temperatures cool down to equilibrate with the wall temperature of 300 K.

The contours of translational temperature are shown in Fig. 6.15. The shocked gas region has expanded to about 17-20 cm behind the shock front. Next, we compare the axial profiles at four radial locations plotted together in Fig. 6.16. For low speeds (case 1 & 2), the gas temperatures in the core flow region have not yet relaxed to their equilibrium values whereas at higher speeds (case 5 & 6), there exists a small post-shock region at equilibrium beyond which the gas state starts deviating from equilibrium. The shocked gas behavior at the centerline is the closest representation of that behind an inviscid normal shock wave, i.e., the gas properties are closest to the equilibrium values and the contact front is the least diffused as compared to other radial locations. However, as the boundary layer growing at the tube walls interacts with the shock front it introduces nonuniformities in the shocked gas behavior. The shocked gas region becomes slightly wider from the centerline towards the wall, and as the gas velocities decrease near the wall, the contact front becomes more diffuse. This can be seen from the axial profiles with increasing values of r from 0 to 5.06 cm. Similar behavior is observed in the vibrational-electronic temperature as shown in Fig. 6.17 and 6.18. In all four cases, the vibrational-electronic energy modes are significantly excited over the entire shocked gas region. For high speed cases, the gas temperatures increase by about 10-30% near the contact front.

6.6.2 N mass-fraction

The dissociative properties of the shocked gas are analyzed here. The contours of N mass-fraction are shown in Fig. 6.19 . Cases 1 & 2 show monotonically increasing amounts of dissociation away from the shock front whereas cases 5 & 6 have peak dissociation rate just behind the shock front. The equilibrium gas temperatures are about 5920 K and 6166 K respectively for cases 1 & 2. The shocked gas temperature in the core flow region are in the range of 6000-8000 K at which gas vibrational energy modes get fully excited and shocked gas region is dominated by dissociated N atoms.

As shown in Fig. 6.20 , the N mass-fraction at the centerline stays very close to the equilibrium value with only a small increment at the contact front, whereas in case 6 ($u_s =$

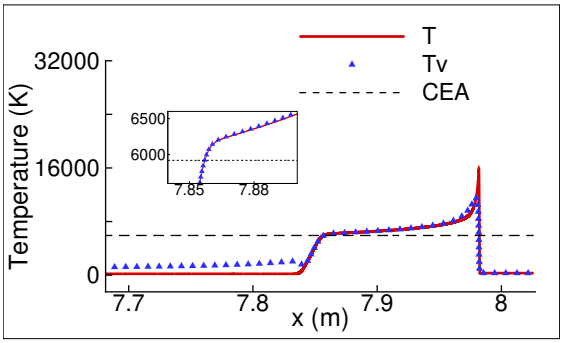

(a) Case 1, centerline

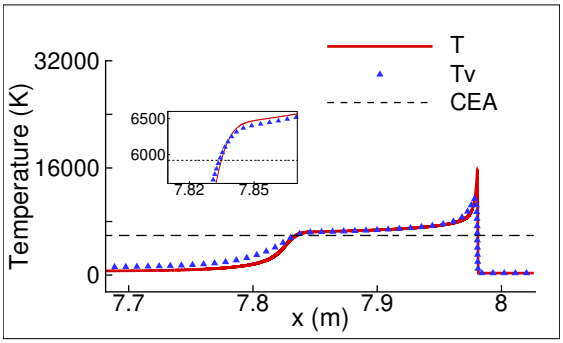

(b) Case 1, r = 4.8 cm

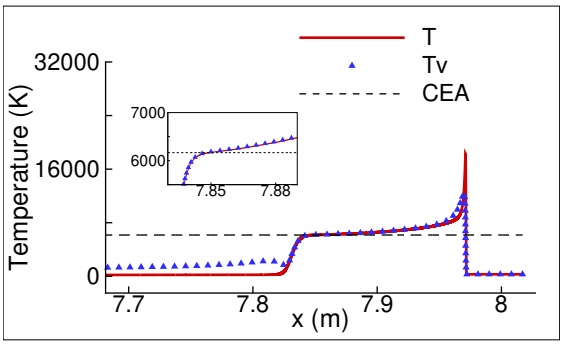

(c) Case 2, centerline

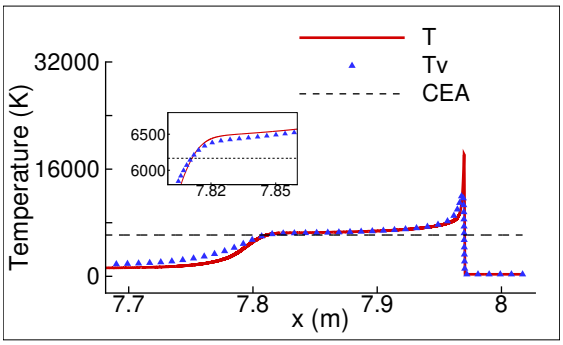

(d) Case 2, r = 4.8 cm

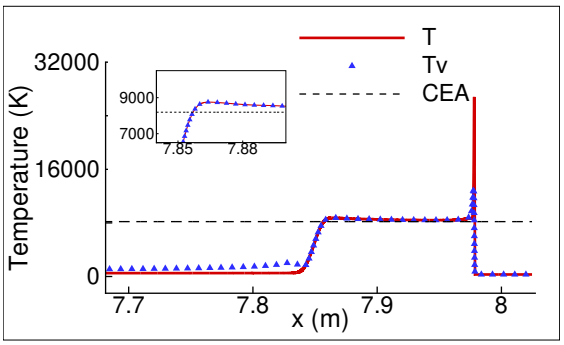

(e) Case 5, centerline

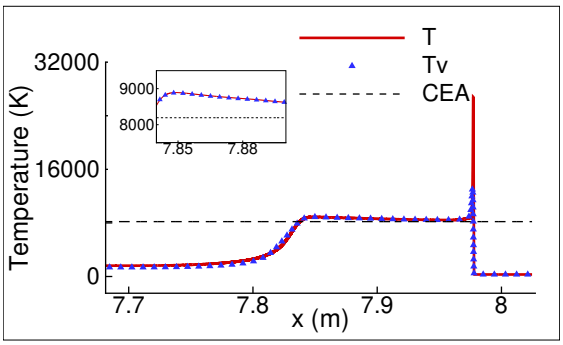

(f) Case 5, r = 4.8 cm

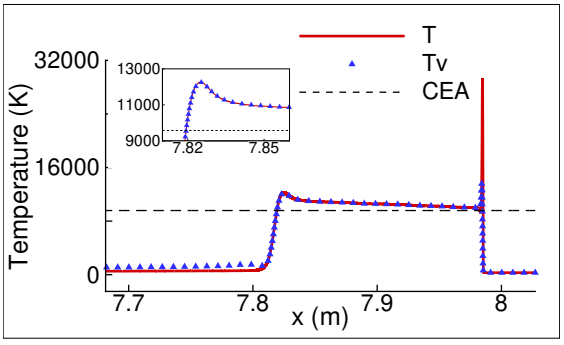

(g) Case 6, centerline

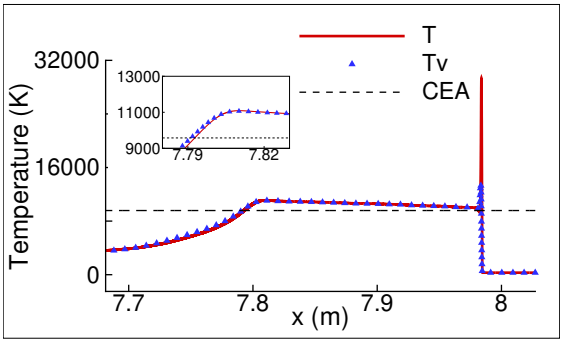

(h) Case 6, r = 4.8 cm

Figure 6.13: Temperature profiles in the core-flow region, $x_s \approx 8$ m

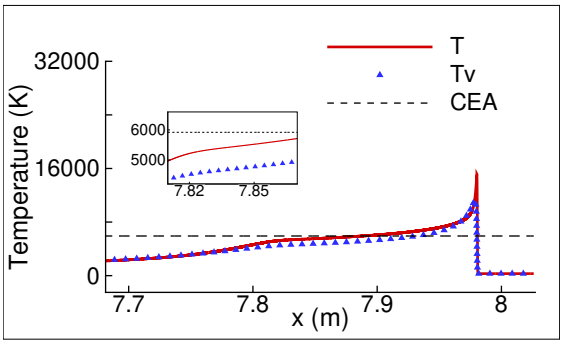

(a) Case 1, r = 5.02 cm

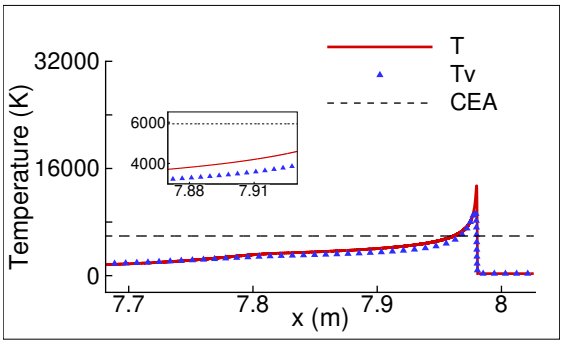

(b) Case 1, r = 5.06 cm

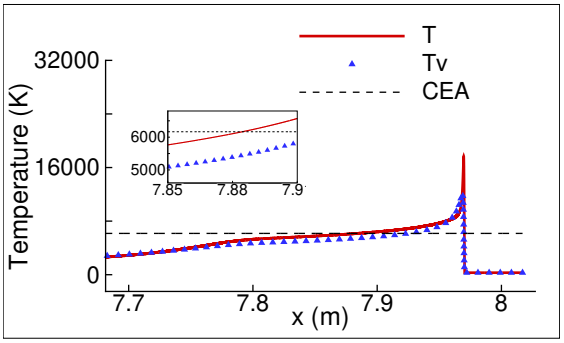

(c) Case 2, r = 5.02 cm

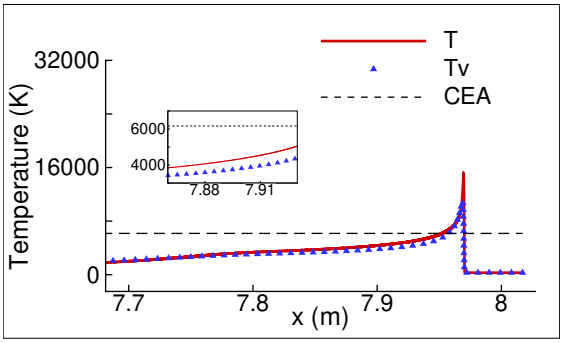

(d) Case 2, r = 5.06 cm

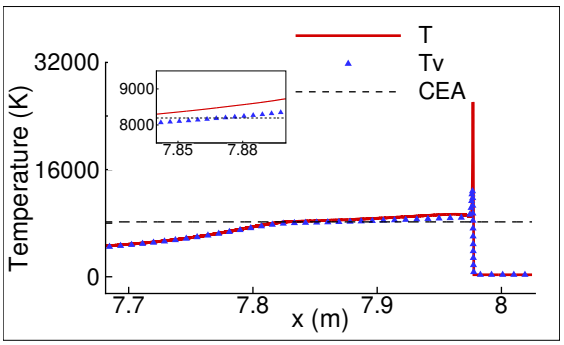

(e) Case 5, r = 5.02 cm

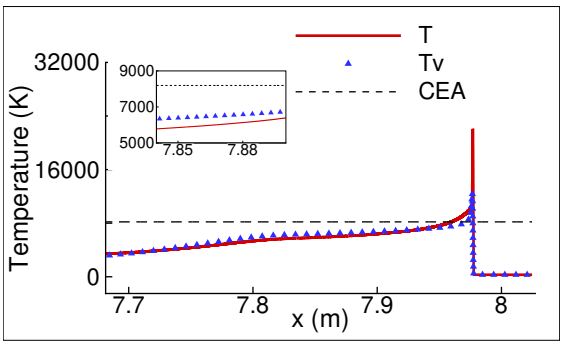

(f) Case 5, r = 5.06 cm

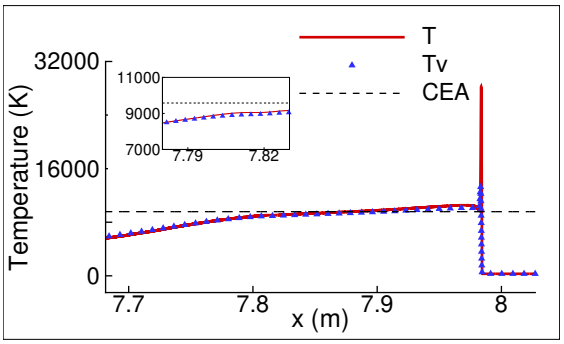

(g) Case 6, r = 5.02 cm

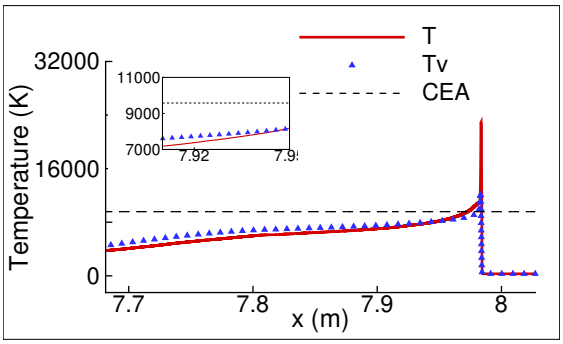

(h) Case 6, r = 5.06 cm

Figure 6.14: Temperature profiles in the near-wall region, $x_s \approx 8$ m

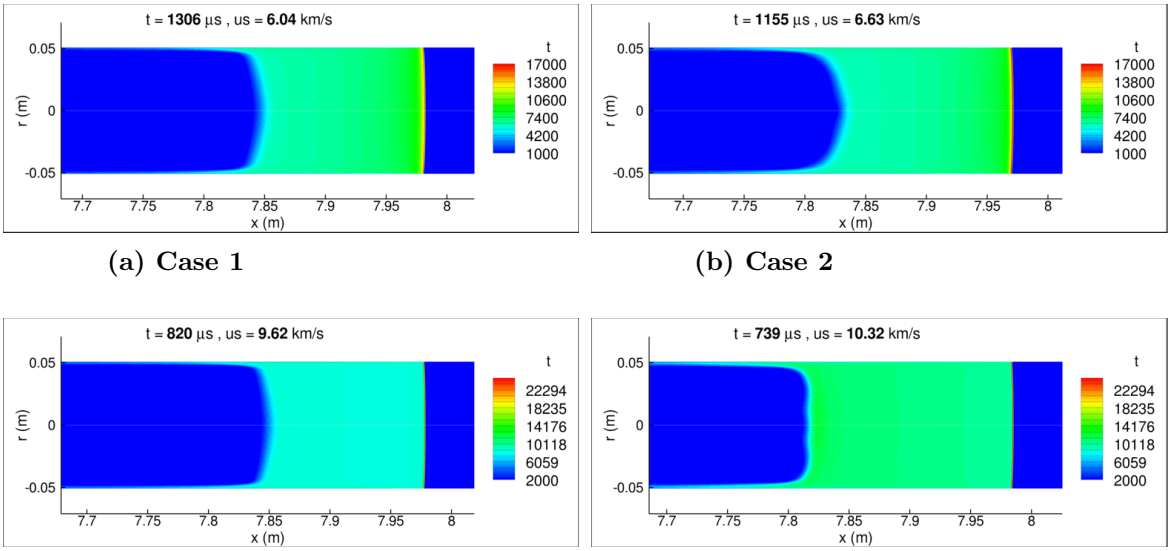

(a) Case 1 (b) Case 2

(c) Case 5 (d) Case 6

Figure 6.15: Translational temperature, $x_s \approx 8$ m (r = 0 is centerline, r = ± 5.08 cm represents tube-walls)

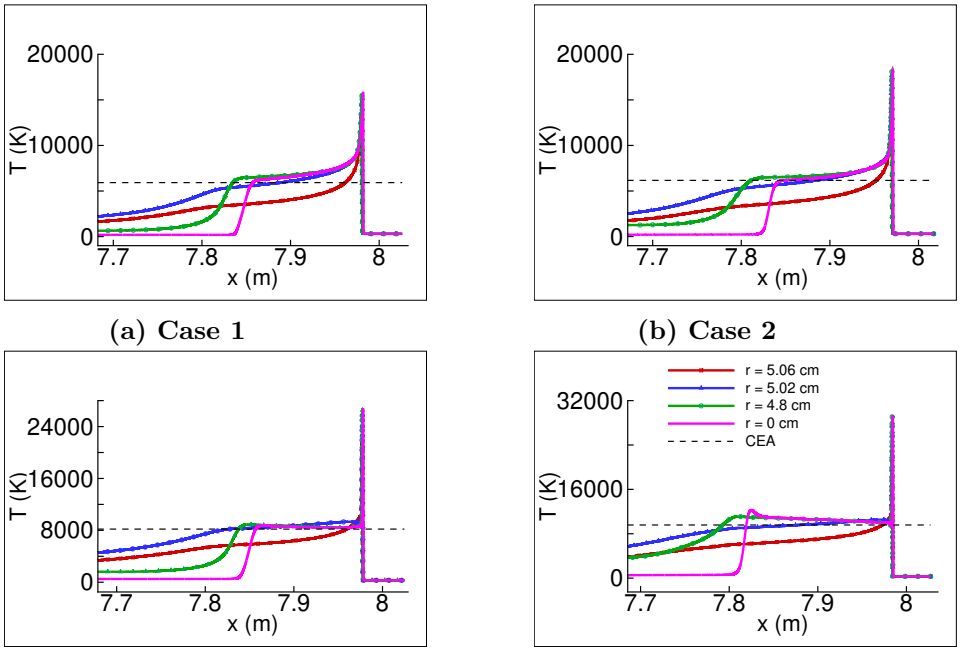

(a) Case 1 (b) Case 2

(c) Case 5 (d) Case 6

Figure 6.16: Translational temperature profiles, $x_s \approx 8$ m

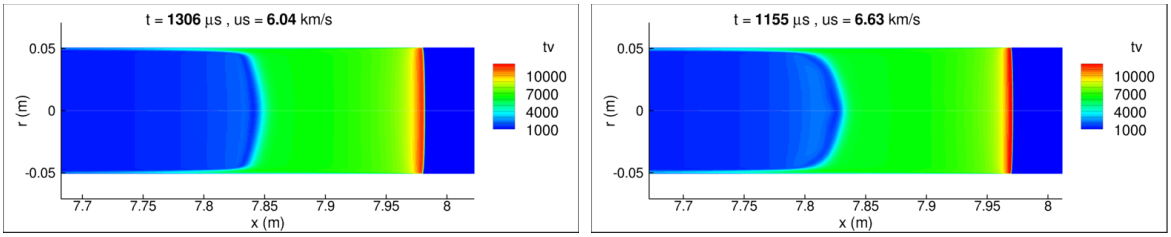

(a) Case 1 (b) Case 2

(c) Case 5 (d) Case 6

Figure 6.17: Vibrational-electronic temperature, $x_s \approx 8$ m (r = 0 is centerline, r = ± 5.08 cm represents tube-walls)

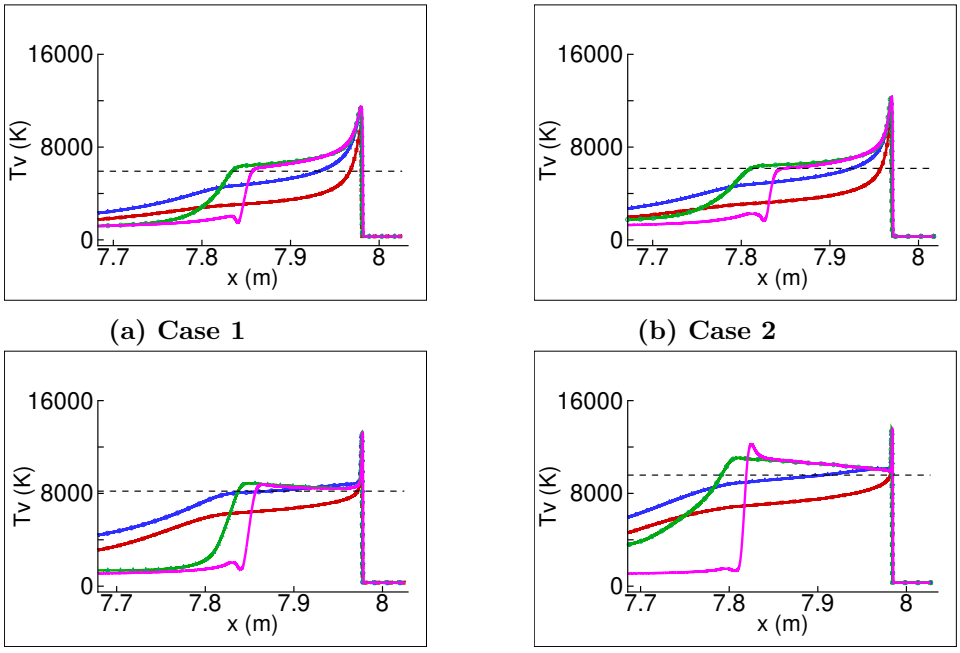

(a) Case 1 (b) Case 2

(c) Case 5 (d) Case 6

Figure 6.18: Vibrational-electronic temperature profiles, $x_s \approx 8$ m

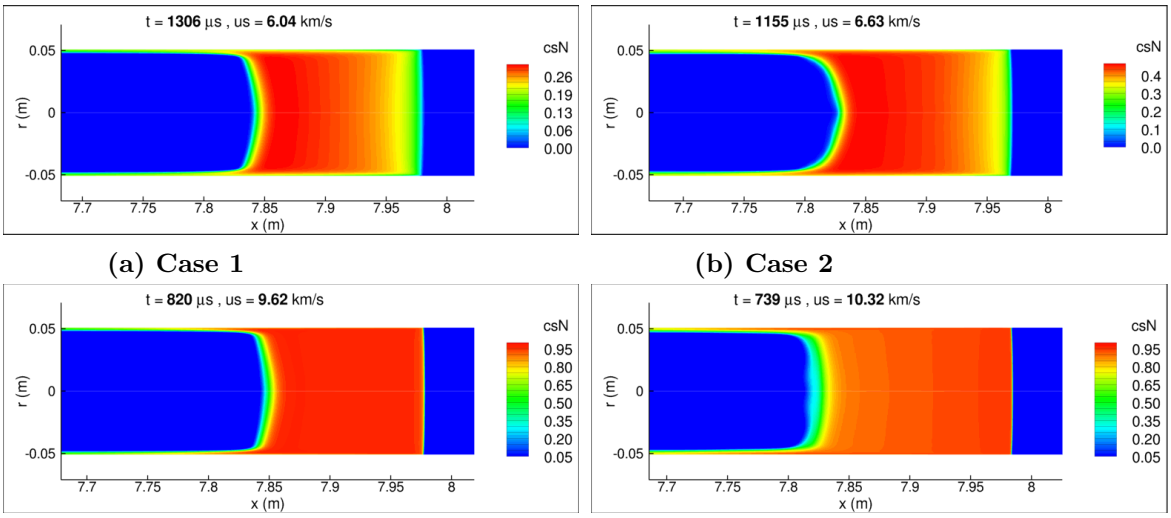

Figure 6.19: N mass-fraction, $x_s \approx 8$ m (r = 0 is centerline, r = ± 5.08 cm represents tube-walls)

10.32 km/s) there is a continuous drop in the mass-fraction of dissociated N atoms. At radial locations away from the centerline, both case 5 and 6, show decreasing rates of dissociation behind the shock. This behavior is a consequence of the gas temperature profiles. Since the gas temperatures are closer to that corresponding to the first ionization energy of nitrogen (≈ 10,000 K), the vibrational energy modes are fully excited (for temperatures > 8,000 K) in the entire shocked gas region, and any excessive energy of the gas mixture is used to excite the electronic energy modes. Hence, as the gas temperatures increase behind the shock, the ionization processes dominate. These observations are further investigated in the following section by analyzing the ionized species mass-fraction.

6.6.3 N^+ mass-fraction

The behavior of ionized species in the gas mixture is now studied. For all four test conditions considered here the diatomic ion N_2^+ is formed only in extreme nonequilibrium conditions at the shock front. It exists as an intermediate species and quickly disappears as the gas energy modes approach towards equilibrium just behind the shock front. Therefore, we focus our analysis on N^+ which is the only dominant ionic species in the gas mixture.

The N^+ mass-fraction contours and axial profiles are shown in Fig. 6.21 and 6.22 respectively. For low speeds, the formation of N^+ is maximum at the shock front and it slowly decreases behind the shock as the temperature is decreasing. For high speeds as mentioned in the previous section, the gas temperatures are significantly high in the entire shocked gas region leading to higher ionization rates. Thus, in the core flow region, the

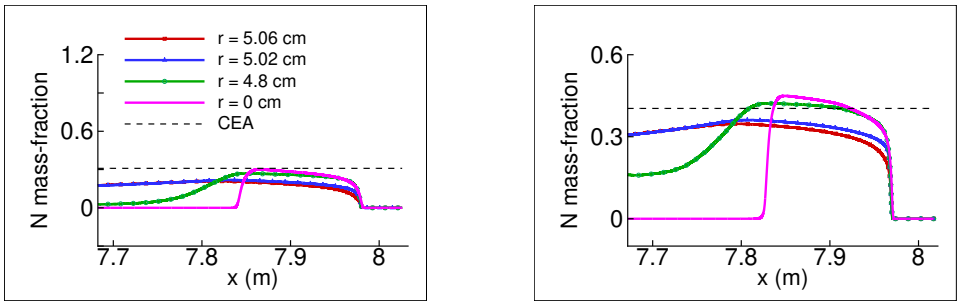

(a) Case 1 (b) Case 2

(c) Case 5 (d) Case 6

Figure 6.20: N mass-fraction profiles, $x_s \approx 8$ m

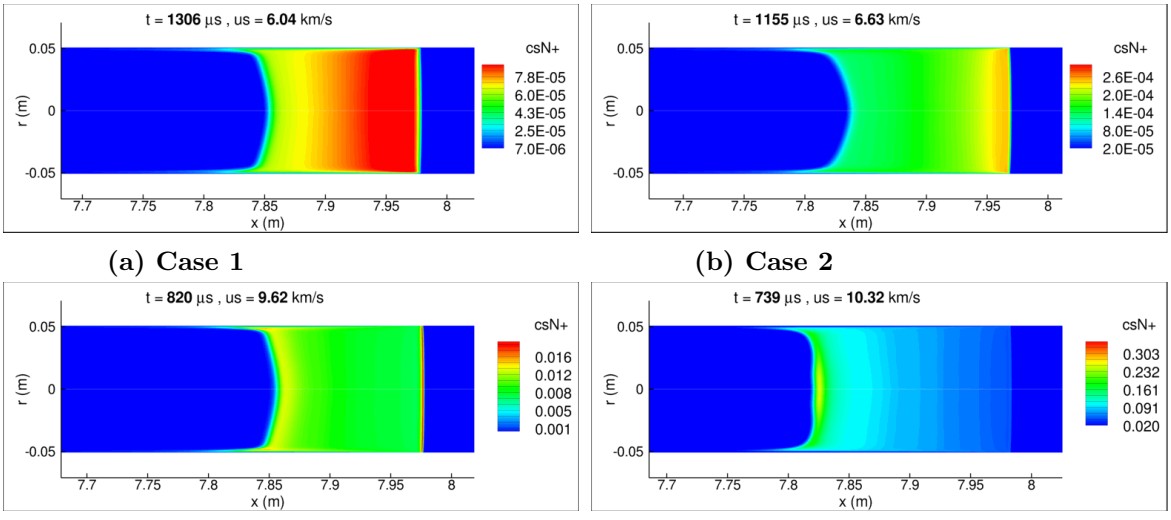

(a) Case 1 (b) Case 2

(c) Case 5 (d) Case 6

Figure 6.21: N^+ mass-fraction, $x_s \approx 8$ m (r = 0 is centerline, r = ± 5.08 cm represents tube-walls)

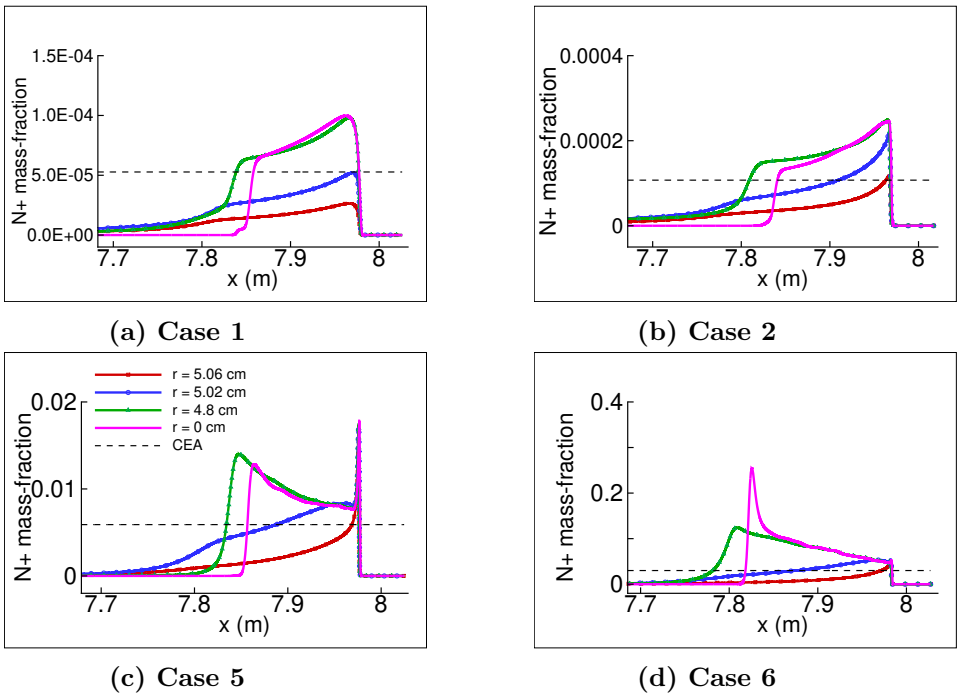

(a) Case 1 (b) Case 2

(c) Case 5 (d) Case 6

Figure 6.22: N^+ mass-fraction profiles, $x_s \approx 8$ m

N^+ mass-fractions increase behind the shock and reach their peak values near the contact front. Based on this analysis, the shocked gas dynamics is dominated by dissociation for speeds < 8 km/s whereas high speed conditions ($u_s > 8$ km/s) are dominated by ionization. The post-shock N^+ mass-fraction vary by about four orders of magnitude as the shock speed increases from 6.04 km/s (case 1) to 10.32 km/s (case 6). The number densities of free-electrons show a qualitatively similar trend which is discussed next.

6.6.4 Electron density

The electron number density (represented by N_e) is the most sensitive flow quantity to the variations in the gas temperatures (N_e varies as $\approx T^8$). The contour plots are shown in Fig. 6.23 followed by their axial profiles in Fig. 6.24 . The electron density profiles show a significant nonequilibrium behavior in the entire core flow region, in all four cases. For lower shock speeds, electron densities drop towards the contact front, whereas at high speeds, the peak electron densities are predicted near the contact front which are up to 40-50% higher than corresponding equilibrium values. This is consistent with the variations of post-shock gas temperatures in each case.

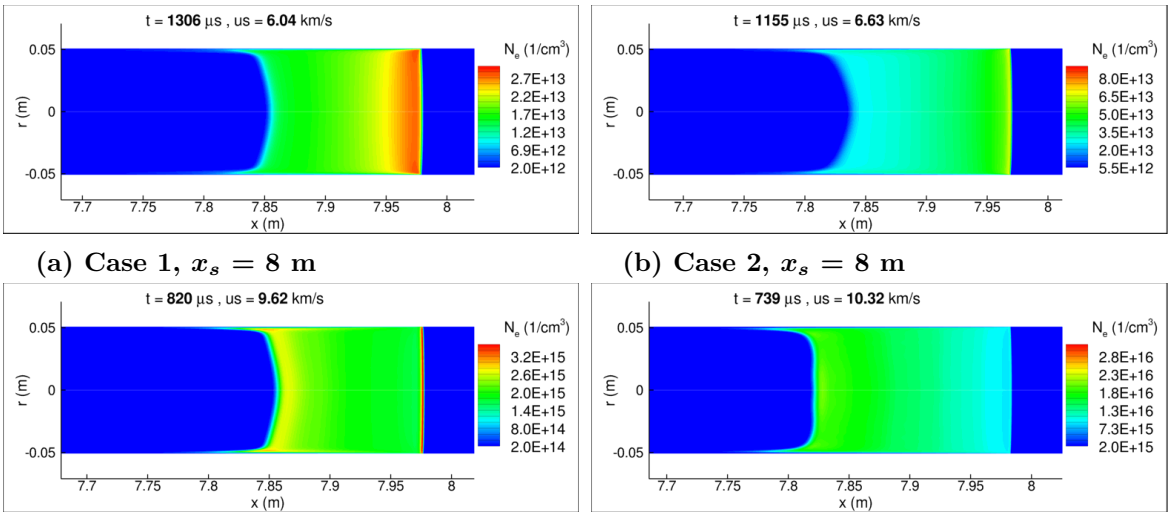

(a) Case 1, $x_s = 8$ m (b) Case 2, $x_s = 8$ m

(c) Case 5, $x_s = 8$ m (d) Case 6, $x_s = 8$ m

Figure 6.23: Electron density contours, $x_s \approx 8$ m, (r = 0 is centerline, r = ± 5.08 cm represents tube-walls)

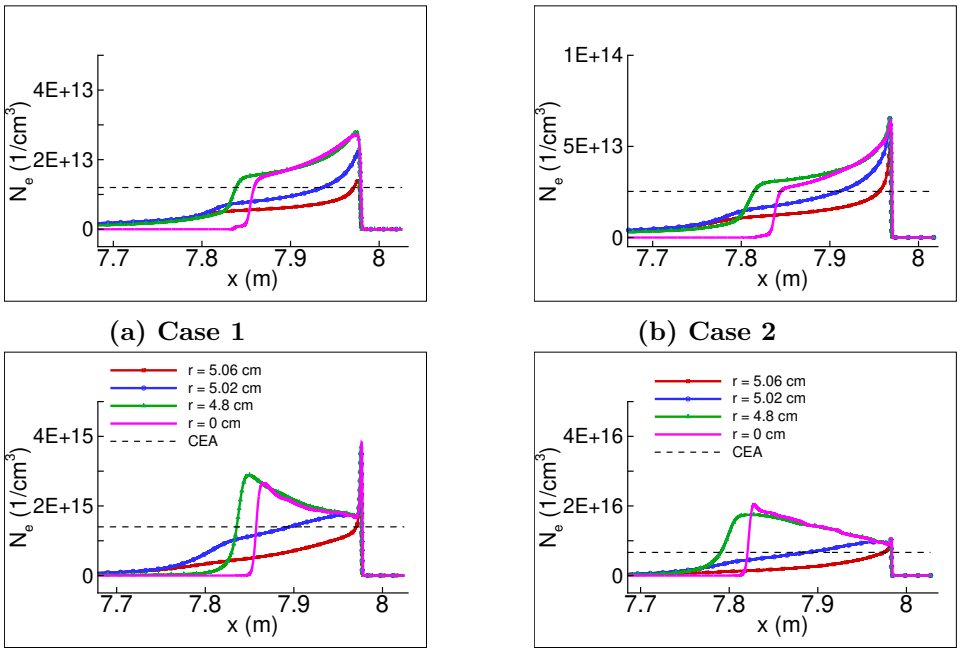

(a) Case 1 (b) Case 2

(c) Case 5 (d) Case 6

Figure 6.24: Electron density profiles, $x_s \approx 8$ m

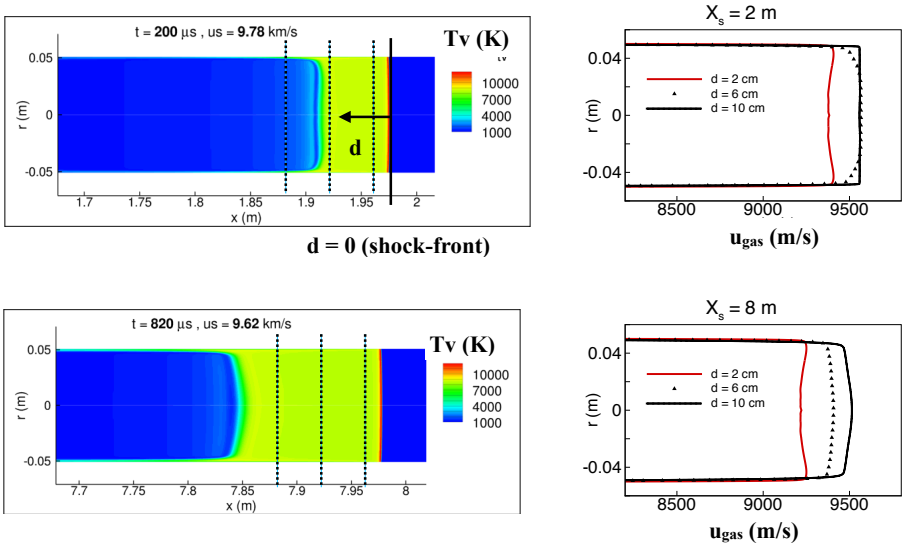

Figure 6.25: Gas profiles for 9.62 km/s shock, $d = 0$ represents the shock front location

6.6.5 Radial variation of gas speeds

The CFD data is further processed to understand the radial variation of gas properties. In this section, the gas velocity profiles are presented for cases 4 and 5, i.e., the 8.7 km/s and 9.62 km/s shocks, respectively. The radial data is extracted at different locations behind the shock as described in Fig. 6.25. The gas velocity profiles are shown at axial locations, d = 2, 6 and 10 cm behind the shock front. As the shock travels from 2 to 8 m, the gas velocity gradients are more diffused in the near wall region, progressing towards a fully developed flow. Due to boundary layer growing behind the shock, the gas speeds at the centerline increase with increasing distances from the shock front.

The gas behavior at the test-section is further analyzed by comparing the gas velocity profiles at different shock speeds. This is shown in Fig. 6.26. The radial data is extracted at the same axial locations behind the shock, represented by the parameter, d. The comparison is shown at axial locations, $d = 2$, 4 and 10 cm, behind the shock front. The inviscid core flow is significantly uniform in both cases (from $r = 0$ to $r \approx 4.8$ cm) while strong gas velocity gradients exist in the near-wall region. Gas velocities in the 9.62 km/s are more diffused, and the velocity profiles are closer to that in a fully developed shock tube flow.

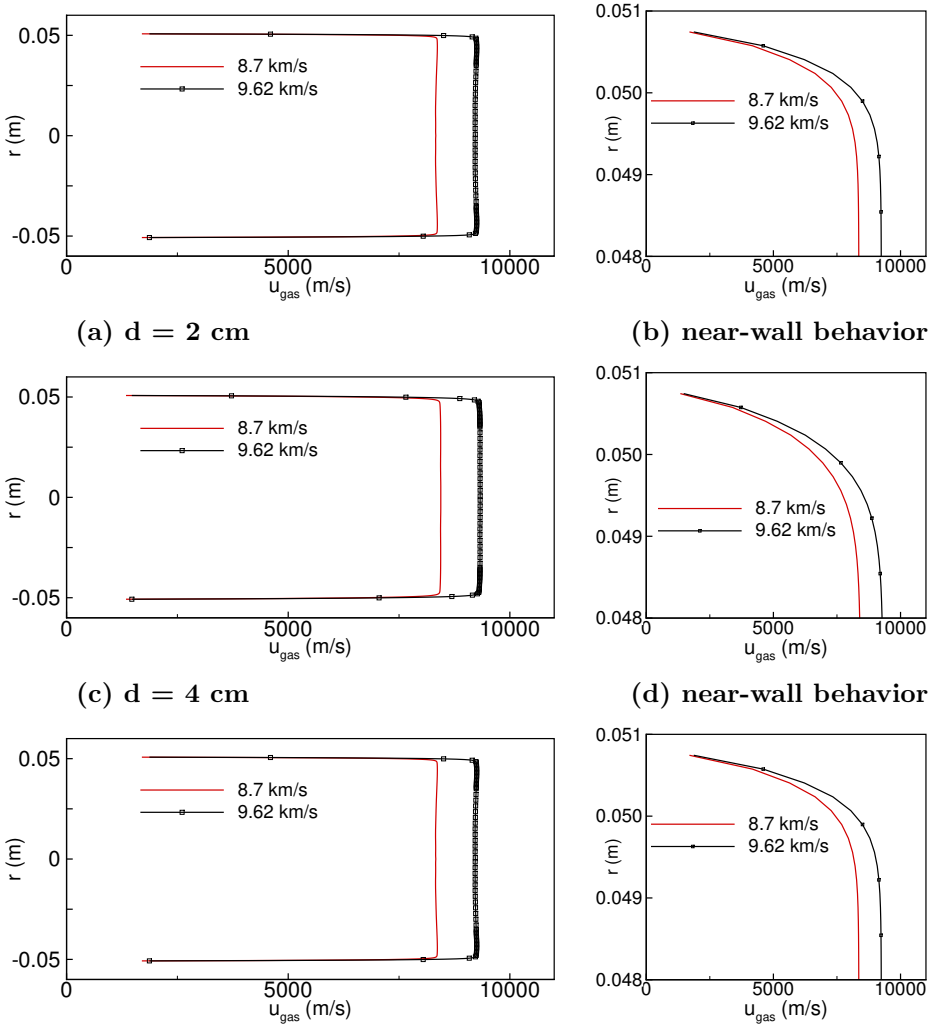

(a) d = 2 cm (b) near-wall behavior

(c) d = 4 cm (d) near-wall behavior

(e) d = 10 cm (f) near-wall behavior

Figure 6.26: Gas velocity profiles at different axial locations behind the shock, $d = 0$ represents the shock front location

6.7 Comparison with test

The next step is to analyze the EAST data at similar test conditions and compare the CFD predictions with the test data.

6.7.1 Shock speed

The variation of the shock speed along the tube for cases 1-6 is shown in Figs. 6.27 and 6.28. The shock speeds measured at discrete axial locations are shown by the square symbols on red lines and the shock speeds in CFD computed at same locations are shown by the circles on the black line. The test data for each case is taken from the benchmark EAST shots (more details in Ref. [1]) in which the measured shock speed at the test-section is closer to that computed by CFD. The plots on the right hand side show the shock speed variations in CFD vs. test near the test-section.

In all these cases, the CFD predicted shock deceleration is smaller than that measured in the experiments. This can be possibly attributed to following two factors: the simplifications of the experimental facility in the CFD simulations which may result in a lower viscous drag, and the deficiencies in the thermochemical modeling which may lead to significantly different reaction rates than in the experiments. A thorough investigation of these effects is important but is beyond the scope of current study. The shock deceleration in CFD shows different trends with varied shock speeds, i.e., for case 1, 3 and 4, the shock deceleration increases as the shock speeds at the test-section are 6.04 km/s, 7.68 km/s and 8.7 km/s, respectively. However, for the case 5 at 9.62 km/s, the shock deceleration is the smallest. This suggests that the CFD predicted evolution of the shocked gas state is significantly different at 9.62 km/s, than other three cases. Since EAST data is available for multiple shock speeds in 6-11 km/s, the shock deceleration at varied shock speeds can be studied. The shock deceleration in CFD compared to EAST experiments is shown in Fig. 6.30. The red squares represent the test data and the black circles show the shock deceleration values computed in CFD. The measured shock deceleration is higher at higher shock speeds, ranging from $\approx$ 2200 km/s^2 to 5000 km/s^2 as the shock speeds vary from 5.94 km/s to 9.62 km/s. CFD shows a slightly different trend, the shock deceleration at 9.62 km/s is the smallest. The shock deceleration values are shown in the Table 6.2. CFD predicted shock speed and deceleration at the test-section are tabulated, along with corresponding information from the EAST shots at a similar shock speed. The last row in the Table 6.2 represents the ratio of shock deceleration values in the tests vs. CFD. The shock deceleration in CFD is about 40-100 times smaller than that measured in EAST.

In order to further understand this behavior, the axial variation of gas velocities is compared for the 6.04 km/s and 9.62 km/s shocks. This is shown in Fig. 6.31. The dashed

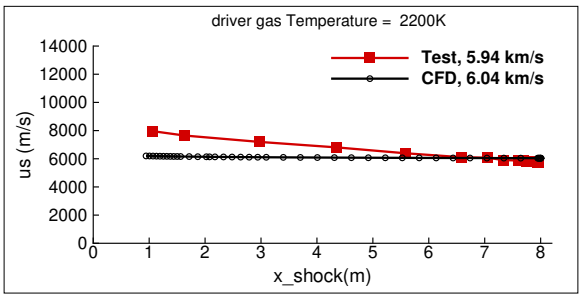

(a) Case 1, $x_s = 1$ to 8 m

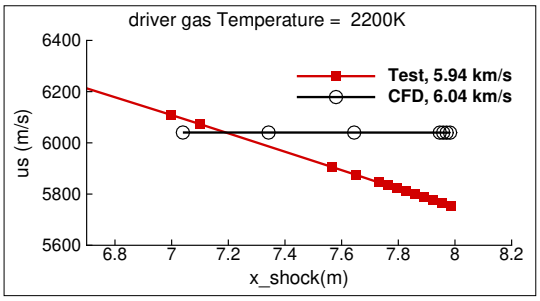

(b) Case 1, near test-section

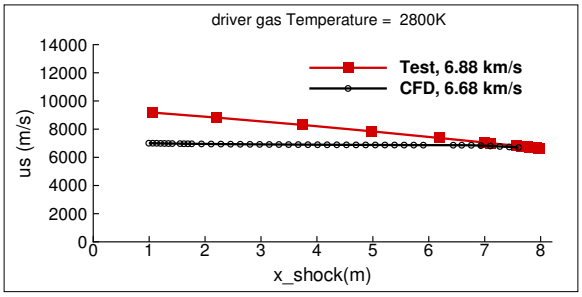

(c) Case 2, $x_s = 1$ to 8 m

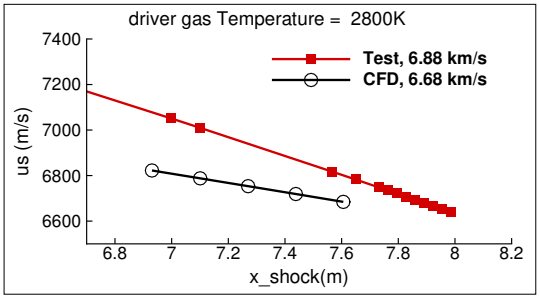

(d) Case 2, near test-section

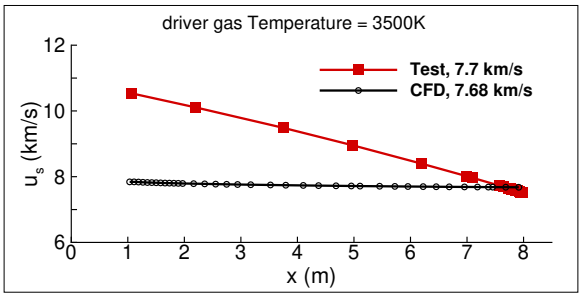

(e) Case 3, $x_s = 1$ to 8 m

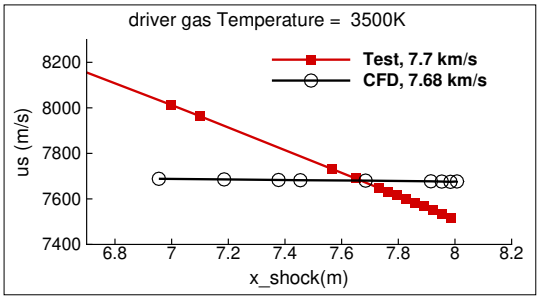

(f) Case 3, near test-section

Figure 6.27: Shock speed variation for 6-8 km/s shocks in nitrogen, CFD vs. EAST data

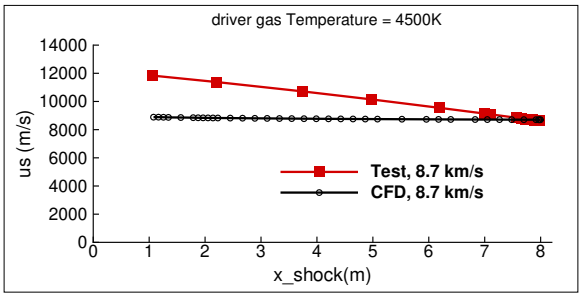

(a) Case 4, $x_s = 1$ to 8 m

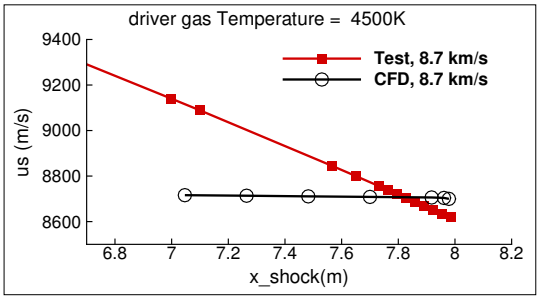

(b) Case 4, near test-section

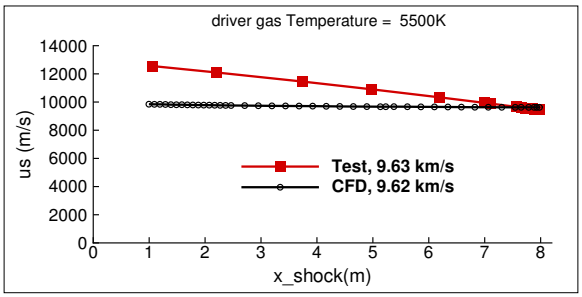

(c) Case 5, $x_s = 1$ to 8 m

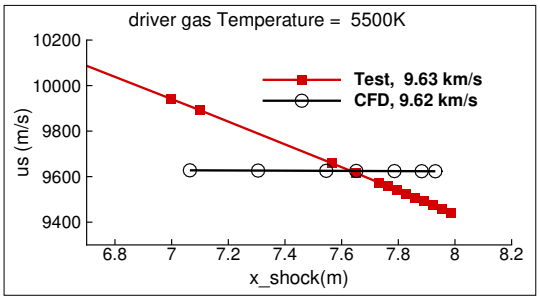

(d) Case 5, near test-section

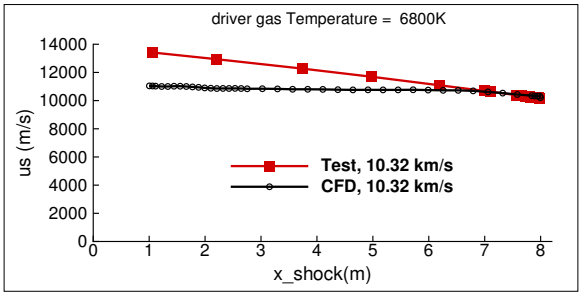

(e) Case 6, $x_s = 1$ to 8 m

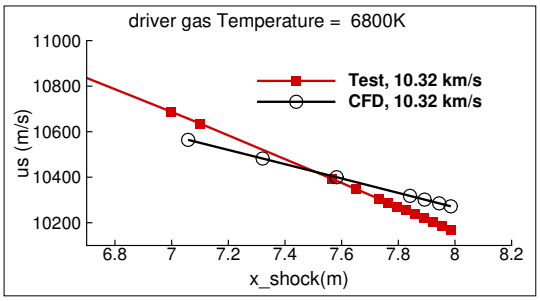

(f) Case 6, near test-section

Figure 6.28: Shock speed variation for 8-11 km/s shocks in nitrogen, CFD vs. EAST data

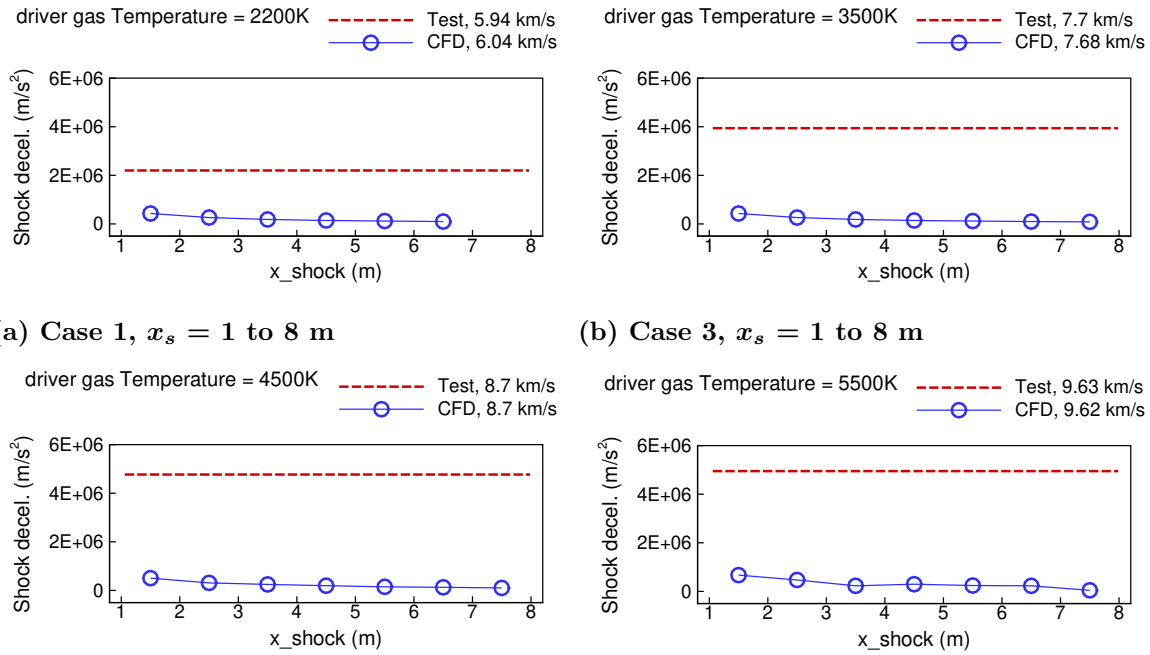

(a) Case 1, x_s = 1 to 8 m **(b) Case 3, x_s = 1 to 8 m**

(c) Case 4, x_s = 1 to 8 m **(d) Case 5, x_s = 1 to 8 m**

Figure 6.29: Shock deceleration along the tube, CFD vs. EAST data

lines represent the equilibrium values plotted with gas velocity profiles from CFD at four different radial locations. In both cases, the centerline gas velocities stay at a near-constant value within 2-3% of the equilibrium values, whereas the gas velocities towards the wall (i.e., at r = 5.02 cm and 5.06 cm) drop significantly behind the shock. Further analysis is required to understand the smallest shock deceleration observed for the 9.62 km/s shock in CFD.

Table 6.2: Shock-deceleration (km/s^2) at centerline

quantity	Case 1	Case 3	Case 4	Case 5
CFD u_s (km/s)	**6.04**	**7.7**	**8.7**	**9.62**
CFD decel. (km/s^2)	57	86	103	46
EAST shot no.	**62-42**	**62-16**	**62-6**	**62-5**
test u_s (km/s)	5.94	7.68	8.7	9.62
test decel. (km/s^2)	2196	3940	4770	4948
decel. ratio (test/CFD)	**38**	**46**	**46**	**108**

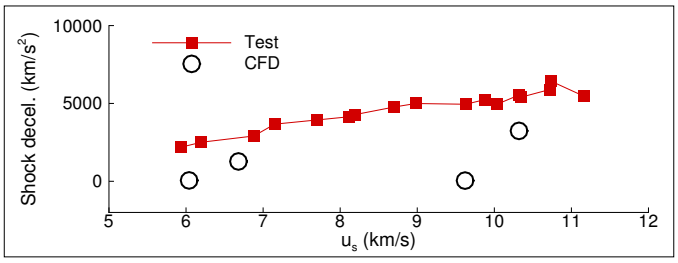

Figure 6.30: Shock deceleration at varied speeds, CFD vs. Test

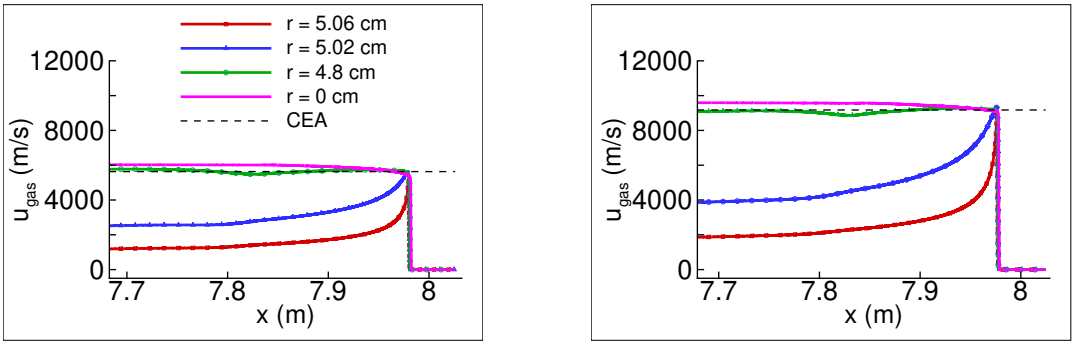

(a) Case 1, $x_s = 8$ m **(b) Case 5, $x_s = 8$ m**

Figure 6.31: Gas velocity profiles, $x_s \approx 8$ m

6.7.2 Electron density

The ionization properties of the shocked gas in CFD are now compared with the EAST measurements. For the shock speeds lower than 7 km/s, the electronic-electron energy modes of the gas are not appreciably excited. Due to the low degree of ionization ($< 5\%$) it is difficult to measure the electron densities. Therefore, EAST electron density data are available only for shock speeds > 7 km/s. A comparison between the test data and CFD predictions is shown in Fig. 6.32. The shock speeds in CFD are slightly lower than that in the available EAST shots. The focus is on the CFD predicted electron densities in the core flow region. The axial profiles are shown at the centerline ($r = 0$) and at $r = 4.8$ cm.

The variation of electron densities in CFD is qualitatively similar to the experiments, i.e., both CFD and experiments predict increasing electron densities behind the shock at the two shock speeds considered here. However, the incremental rates are quite different in both cases. Also, the experiment for case 6 shows below equilibrium electron densities away from the shock front. These discrepancies are expected since there are considerable differences between the actual flow physics in the experimental facility and its approximate numerical modeling in the CFD. The set of simulations presented in this work are the first step towards understanding the complicated gas dynamics in the shock tube flow and

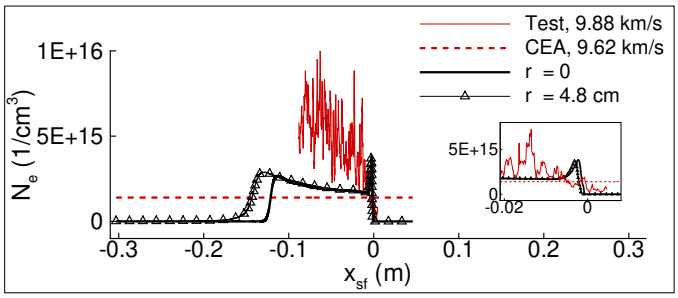

(a) Case 5, u_s = 9.62 km/s

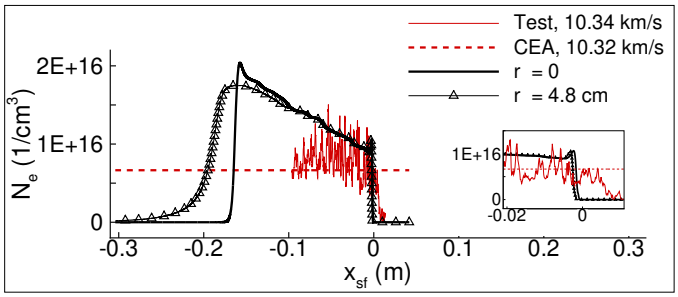

(b) Case 6, u_s = 10.32 km/s

Figure 6.32: Electron density, CFD vs. Test, $x_s \approx 8$ m

identifying the scope of further modeling improvements. It should also be noted that the electron density comparison presented here is not exact. This is because at a particular axial location, the test data represent an integrated value of electron densities averaged over the entire cross-section, whereas the CFD data shows the electron density value at a particular point. The test data are also averaged in the axial direction in the vicinity of the shock front. Thus, the CFD data should be processed by the spatial convolution function for a true quantitative comparison against the test data.

However, the current comparison is good for an understanding of the qualitative trend in CFD and tests. The test data shows two different trends as the shock speeds change from 9.88 km/s to 10.34 km/s. For 9.88 km/s, the measured electron densities increase from their equilibrium value by up to a factor of 4 within 3 cm behind the shock, and stay about 2-3 times higher than the equilibrium values, over the entire shocked gas region. This suggests a state of strong thermochemical nonequilibrium in the shocked gas. On the other hand, the electron density data at 10.34 km/s are within 5-7% of their equilibrium values in most of the shocked gas region, indicating a thermochemical equilibrium. Interestingly, CFD predicts a nonequilibrium behavior in both conditions, where the extent of nonequilibrium increases with increasing shock speed. This clearly shows that the gas kinetics in CFD is significantly different than that observed in tests, which can be attributed to the limitations in the modeling of various physical and thermochemical processes in the shock tube flow.

6.8 Flow-field evolution

Shock deceleration in CFD showed an unexplained trend with increasing shock speeds, also, the deceleration is much smaller than that observed in EAST. There are several possible loss mechanisms in the actual EAST flow, as were described in the Chapter 1, that can cause the shock to decelerate. However, in the CFD, the only mechanism which can dissipate the energy from the flow-field, is the growth of wall-boundary layer. In this section, the CFD data is further analyzed to study the time-evolution of boundary layer growth and gas ionization properties for cases 1, 3, 4 and 5.

6.8.1 Boundary layer growth

The boundary layer thicknesses, δ_{99}, are plotted after approximately 2, 4, 6 and 8 m of shock travel, as shown in Fig. 6.33. Here $xs = 0$ represents the location of the shock front. As the shock moves forward, the boundary layer grows behind the shock front from zero to its maximum value until the contact front. Beyond the contact front, the driver gas expands and gas speeds decrease. Hence, the boundary layer starts shrinking towards a value of zero at the expansion fan leading edge and beyond. After 2 m of shock travel, the 6.14 km/s shock (i.e., case 1, with the shock speed quoted at $\approx$ 2 m) shows a maximum boundary layer thickness of about 1.8 cm at about 6.5 cm behind the shock front. This also marks the approximate location of the contact front, and the boundary layer thickness decreases from 1.8 cm to zero in the region located from $\approx$ 6.5 cm to 8.5 cm behind the shock front. The maximum thickness for 9.78 km/s shock (i.e., case 5) is about 3.2 cm. The maximum boundary layer thickness is higher with higher shock speeds. As the shock travels towards the test-section, the post-shock flow relaxes and gas speeds decrease, hence, the maxmium boundary layer thickness decrease for higher shock speeds. However, the flow behind the lowest shock speed, case 1, is far from equilibrium even at the test-section (as shown in the previous sections). Therefore, the maximum boundary layer thickness does not change much, only the hot gas region becomes wider with time. The maximum boundary layer thickness at the test-section are about 2.7 cm, 2.5 cm, 2.3 cm and 1.7 cm, respectively, for shock speeds 9.63 km/s, 8.7 km/s, 7.7 km/s and 6.04 km/s. These were referred to as cases 5, 4, 3 and 1, respectively, in the previous sections. The width of the hot gas region is about 14 cm for higher shock speeds, and about 16 cm for 6.04 km/s shock. The 9.63 km/s shock shows a small region of nearly constant boundary layer thickness, from about 10.5 cm to 11.7 cm behind the shock front which is not observed for other cases. This can be an indicator of the fully developed tube flow in the case 5, and possibly a reason behind the smallest shock-deceleration at this shock speed. However, further analysis is required to fully understand and explain the gas behavior in CFD.

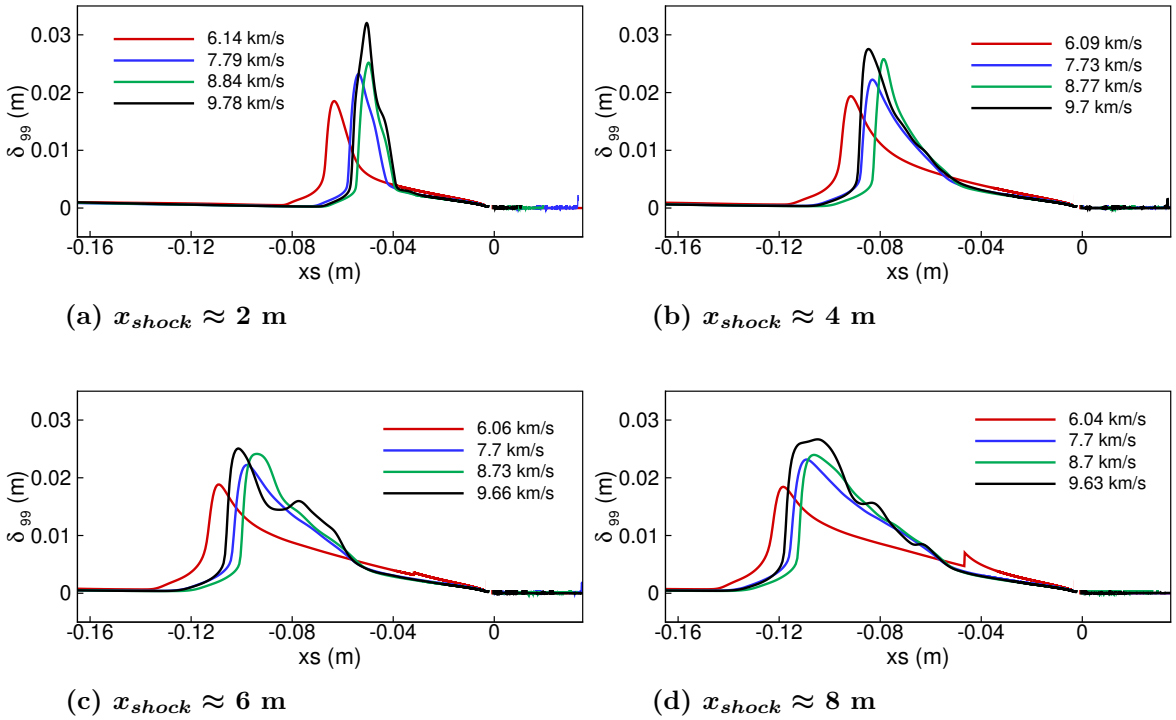

(a) $x_{shock} \approx 2$ m

(b) $x_{shock} \approx 4$ m

(c) $x_{shock} \approx 6$ m

(d) $x_{shock} \approx 8$ m

Figure 6.33: BL thickness (δ_{99}) behind the shock, $xs = 0$ represents the shock front location

6.9 Electron density profiles

Finally, the time-evolution of post-shock electron density profiles is studied to identify any abnormalities in the CFD predicted gas behavior for case 5, as compared to other cases 1, 3 or 4. The axial profiles of electron densities are plotted after 2, 4, 6 and 8 m of shock travel, as shown in Fig. 6.34. For simplicity, only case 1 and 5 are shown. The qualitative behavior of the electron density profiles stays similar during 2 to 8 m of shock travel, for both the cases.

6.10 Summary

High enthalpy gas dynamics in nitrogen is investigated at six different shock speeds via CFD simulations in conjuction with EAST data. The shocked gas region is dominated by dissociation at low speeds (i.e., < 8 km/s), whereas the high speed cases (> 8 km/s) show considerably high degrees of ionization (up to 10-15%). CFD predicted gas properties such as shock deceleration and post-shock electron number densities are compared with the test data. A good qualitative agreement is obtained between the two, while there are certain discrepancies due to various aspects of the numerical modeling. The shock deceleration in CFD is significantly lower than measured values, and the comparison of post-shock electron densities suggests that the rates of thermochemical excitation and relaxation processes are quite different in CFD vs. tests. The shock-formation process, boundary layer growth rate and radial variation of gas properties are analyzed. The test data show increasing shock deceleration at increasing shock speeds, whereas the CFD predicted deceleration is the smallest for the 9.62 km/s shock. This indicates a significantly different evolution of the shocked gas state in CFD relative to other test cases.

These CFD simulations provide an understanding of the gas kinetics at high enthalpy conditions based on existing physical and chemistry models, and the comparison with benchmark EAST data helps identifying the range of conditions where CFD predictions significantly differ from the test observations. The current CFD predictions provide a qualitative knowledge of the gas behavior at extreme conditions. Further analysis is required for a more complete understanding of the shocked gas dynamics over the entire range of entry conditions tested in EAST.

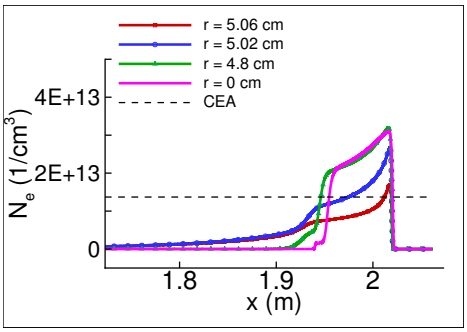

(a) Case 1, $x_s \approx 2$ m

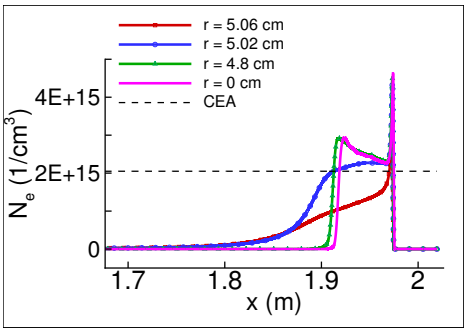

(b) Case 5, $x_s \approx 2$ m

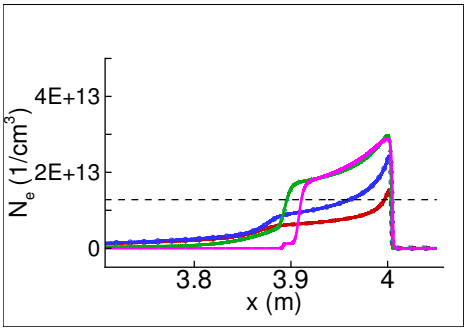

(c) Case 1, $x_s \approx 4$ m

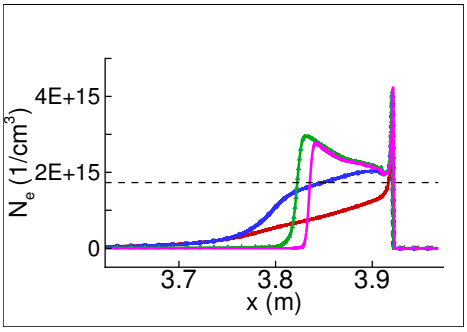

(d) Case 5, $x_s \approx 4$ m

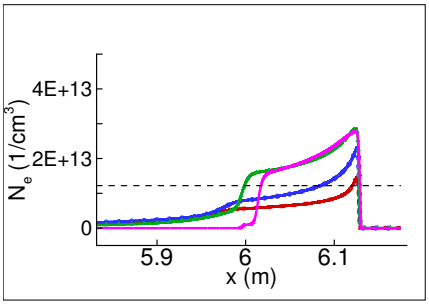

(e) Case 1, $x_s \approx 6$ m

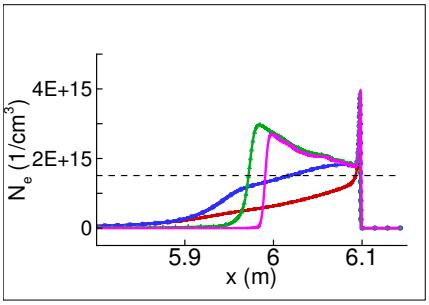

(f) Case 5, $x_s \approx 6$ m

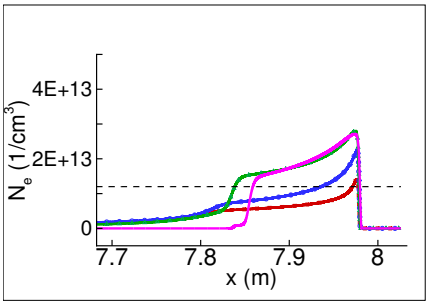

(g) Case 1, $x_s \approx 8$ m

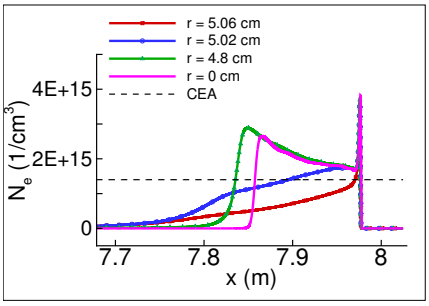

(h) Case 5, $x_s \approx 8$ m

Figure 6.34: Evolution of post-shock electron density profiles; $r = 0$ represents the shock tube centerline, dashed lines represent CEA equilibrium values

Chapter 7

Conclusions

Axisymmetric solutions of EAST shock tube flow are obtained by using an optimized simulation approach. The computational cost is reduced by approximately three orders of magnitude by solving the flow in a moving frame of reference with active-shock tracking, as compared to the calculations in a fixed frame of reference. The numerical methods are optimized for time-accurate predictions of high enthalpy, nonequilibrium evolution of the shock tube flow, and the simulation approach is validated against analytical solutions. Numerical simulations are performed for 10 km/s air shock, and 6-11 km/s shocks in nitrogen. The strong gradients at the shock front and within the boundary layer are fully resolved during the entire shock propagation. Time-accurate evolution of the shocked gas flow are hence obtained until the shock reaches the EAST test section. Since the diaphragm is assumed to be fully open at the beginning of the simulations, the numerically predicted shock starts at a large speed, and then quickly decelerates to a near-constant speed based on the excitation, interaction and relaxation of different energy modes of the gas.

A laminar boundary layer grows behind the shock front as it travels along the tube and the shocked gas is decelerated near the wall. The test gas behind the shock front first relaxes towards thermochemical equilibrium corresponding to the instantaneous shock speed, and then deviates from the equilibrium as it interacts with previously shocked downstream gas. This is demonstrated by the axial profiles of temperatures and electron density behind the shock. The maximum boundary layer thickness for 10 km/s air shock is 6 mm. High enthalpy nitrogen shocks are simulated with an improved ionization modeling, which significantly affects the numerically predicted gas behavior. The post-shock gas behind nitrogen shocks shows increasing nonequilibrium gas behavior with increasing shock speeds. The shock-formation process, the growth of wall-boundary layer growth and radial variation of gas properties are also studied. The maximum boundary layer thickness for nitrogen shocks are approximately 1.7 cm, 2.3 cm, 2.5 cm and 2.8 cm at shock speeds of 6.04 km/s, 7.7 km/s, 8.7 km/s and 9.63 km/s, respectively.

The CFD solutions obtained here are the *first-ever* numerically stable predictions of shocked gas behavior at the EAST test section, enabling for a detailed analysis of the shock tube flow physics. Numerical solutions predict a deceleration of the shock, and the shock front shape shows a curvature near the wall. Shock waves in CFD attain a near-constant speed after propagating 1-2 m (i.e., 10-20 tube-diameters) along the tube. Hot gases show dissociation dominated gas dynamics at shock speeds less than 8 km/s while a significant gas ionization is observed at higher speeds.

The fluid dynamic predictions are also compared with EAST experimental data. Overall, a good qualitative agreement is obtained between CFD predicted gas behavior and test observations. However, there are differences between the two which can be attributed to various assumptions and simplifications made in the CFD modeling. The shock-deceleration in CFD is about 40-100 times smaller than that reported in the experiments, and the post-shock gas shows increasing nonequilibrium behavior with increasing shock speeds whereas EAST data show a strong nonequilibrium gas behavior only for moderate shock speeds (8-10 km/s). However, the numerical predictions are extremely sensitivie to the numerical and thermochemical modeling.

The CFD simulations presented in this work provide an understanding of high enthalpy gas dynamics based on existing physical and chemistry models. The comparison with benchmark EAST data helps identifying the range of conditions where CFD predictions significantly differ from the test observations. The current CFD predictions enable for a qualitative knowledge of the gas behavior at extreme conditions during atmospheric entry. Further analysis is required for a more complete understanding of the shocked gas dynamics over the entire range of entry conditions tested in EAST. The numerical predictions are extremely sensitive numerical and thermochemical modeling. Sensitivity studies can be performed to assess the impact of gas kinetic and turbulence models on the numerically predicted gas behavior.

Bibliography

[1] Brandis, A. M., and Cruden, B. A., "Shock Tube Radiation Measurements in Nitrogen," *2018 Joint Thermophysics and Heat Transfer Conference*, 2018, p. 3437. doi:10.2514/6.2018-3437.

[2] Park, C., "Assessment of Two-Temperature Kinetic Model for Ionizing Air," *Journal of Thermophysics and Heat Transfer*, Vol. 3, No. 3, July 1989, pp. 233–244. doi:10.2514/6.1987-1574.

[3] Gnoffo, P. A., "Planetary-Entry Gas Dynamics," *Annual Review of Fluid Mechanics*, Vol. 31, No. 1, 1999, pp. 459–494. doi:10.1146/annurev.fluid.31.1.459.

[4] Gnoffo, P. A., Weilmuenster, K. J., Hamilton, H. H., Olynick, D. R., and Venkatapathy, E., "Computational aerothermodynamic design issues for hypersonic vehicles," *Journal of Spacecraft and Rockets*, Vol. 36, No. 1, 1999, pp. 21–43. doi:10.2514/2.3430.

[5] Hollis, B. R., "Blunt-body entry vehicle aerotherodynamics: Transition and turbulent heating," *Journal of Spacecraft and Rockets*, Vol. 49, No. 3, 2012, pp. 435–449. doi:10.2514/1.51864.

[6] Johnson, J. E., Starkey, R. P., and Lewis, M. J., "Aerothermodynamic optimization of reentry heat shield shapes for a crew exploration vehicle," *Journal of Spacecraft and Rockets*, Vol. 44, No. 4, 2007, pp. 849–859. doi:10.2514/1.27219.

[7] Hanley, G., and Korkan, K., "Apollo command module aerothermodynamic characteristics at hyperbolic Earth entry velocities," *Journal of Spacecraft and Rockets*, Vol. 3, No. 8, 1966, pp. 1274–1281. doi:10.2514/3.28639.

[8] Kontinos, D. A., and Wright, M. J., "Introduction: Atmospheric entry of the stardust sample return capsule," *Journal of Spacecraft and Rockets*, Vol. 47, No. 5, 2010, pp. 705–707. doi:10.2514/1.52887.

[9] Olynick, D., Chen, Y.-K., and Tauber, M. E., "Aerothermodynamics of the Stardust sample return capsule," *Journal of Spacecraft and Rockets*, Vol. 36, No. 3, 1999, pp. 442–462. doi:10.2514/2.3466.

[10] Suzuki, T., Fujita, K., Yamada, T., Inatani, Y., and Ishii, N., "Postflight thermal protection system analysis of hayabusa reentry capsule," *Journal of Spacecraft and Rockets*, Vol. 51, No. 1, 2013, pp. 96–105. doi:10.2514/1.A32549.

[11] Grinstead, J. H., Wilder, M. C., Reda, D. C., Cornelison, C. J., Cruden, B. A., and Bogdanoff, D. W., "Shock tube and ballistic range facilities at NASA ames research center," 2010. URL `https://ntrs.nasa.gov/archive/nasa/casi.ntrs.nasa.gov/20100027327.pdf`.

[12] Hollis, B. R., Berger, K. T., Berry, S. A., Brauckmann, G. J., Buck, G. M., DiFulvio, M., Horvath, T. J., Liechty, D. S., Merski, N. R., Murphy, K. J., et al., "Entry, descent and landing aerothermodynamics: Nasa langley experimental capabilities and contributions," *52nd Aerospace Sciences Meeting*, 2014, p. 1154. doi:10.2514/6.2014-1154.

[13] Hornung, H., Sturtevant, B., Belanger, J., Sanderson, S., Brouillette, M., and Jenkins, M., "Performance data of the new free-piston shock tunnel T5 at GALCIT," *Shock Waves*, Springer, 1992, pp. 603–610. doi:10.2514/6.1992-3943.

[14] Dufrene, A., MacLean, M., and Holden, M., "High enthalpy studies of capsule heating in an expansion tunnel facility," *43rd AIAA Thermophysics Conference*, 2012, p. 2998. doi:10.2514/6.2012-2998.

[15] MacLean, M., Dufrene, A., Wadhams, T., and Holden, M., "Numerical and experimental characterization of high enthalpy flow in an expansion tunnel facility," *48th AIAA aerospace sciences meeting including the new horizons forum and aerospace exposition*, 2010, p. 1562. doi:10.2514/6.2010-1562.

[16] Bottin, B., Chazot, O. P., Carbonaro, M., Haegen, V. V. D., and Paris, S., "The VKI Plasmatron Characteristics and Performance," 2000.

[17] Tanno, H., Komuro, T., Sato, K., Itoh, K., Arai, K., and Yamada, K., "Basic characteristics of the free-piston driven expansion tube JAXA HEK-X," *32nd AIAA Aerodynamic Measurement Technology and Ground Testing Conference*, 2016, p. 3817. doi:10.2514/6.2016-3817.

[18] McGilvray, M., Doherty, L. J., Morgan, R. G., Gildfind, D., Jacobs, P., and Ireland, P., "T6: The Oxford University Stalker Tunnel," *20th AIAA International Space Planes and Hypersonic Systems and Technologies Conference*, 2015, p. 3545. doi:10.2514/6.2015-3545.

[19] Jacobs, P., Morgan, R., Brandis, A., Buttsworth, D., Dann, A., D'Souza, M., Eichmann, T., Gildfind, D., Gollan, R., Jacobs, C., et al., "Design, operation and testing in expansion tube facilities for super-orbital re-entry," 2013. URL `https://espace.library.uq.edu.au/view/UQ:326742`.

[20] Splinter, S., Daryabeigi, K., Horvath, T., Mercer, C., Ghanbari, C., Ross, M., Tietjen, A., and Schwartz, R., "Solar Tower Experiments for Radiometric Calibration and Validation of Infrared Imaging Assets and Analysis Tools for Entry Aero-Heating Measurements," *40th Thermophysics Conference*, 2008, p. 4025. doi:10.2514/6.2008-4025.

[21] Bader, R., Levêque, G., Haussener, S., and Lipiński, W., "High-flux solar simulator technology," Optical Society of America, 2016. doi:10.1364/OSE.2016.SoM3C.3.

[22] Bogdanoff, D. W., "Shock Tube Experiments for Earth and Mars Entry Conditions," *Von Karman Institute Lecture Series*, 2008. doi:https://apps.dtic.mil/dtic/tr/fulltext/u2/a568019.pdf.

[23] Grinstead, J. H., Wilder, M. C., Olejniczak, J., Bogdanoff, D. W., Allen, G. A., Dang, K., and Forrest, M. J., "Shock-heated Air Radiation Measurements at Lunar Return Conditions," *AIAA Paper*, Jan. 2008. doi:10.2514/6.2008-1244.

[24] Brandis, A. M., Johnston, C. O., Cruden, B. A., Prabhu, D., and Bose, D., "Uncertainty Analysis and Validation of Radiation Measurement for Earth Reentry," *Journal of Thermophysics and Heat Transfer*, Vol. 29, No. 2, 2015. doi:10.2514/1.T4000.

[25] Brandis, A. M., Saunders, D. A., Johnston, C. O., Cruden, B. A., and White, T. R., "Radiative Heating on the After-Body of Martian Entry Vehicles," *AIAA Paper*, June 2015. doi:10.2514/6.2015-3111.

[26] Thomas K., W., Theisinger, J. E., Brune, A. J., and Johnston, C. O., "Backshell Radiative Heating on Human-Scale Mars Entry Vehicles," *AIAA Paper*, June 2017. doi:10.2514/6.2017-4532.

[27] Brandis, A., and Cruden, B. A., "Benchmark Shock Tube Experiments of Radiative Heating Relevant to Earth Re-entry," *AIAA Paper*, Jan. 2017. doi:10.2514/6.2017-1145.

[28] Hall, J. G., and Rathi, J. S., "Unsteady expansion waveforms generated by diaphragm rupture," *AIAA Journal*, Vol. 12, No. 5, 1974, pp. 724–726. doi:10.2514/3.49332.

[29] Sharma, S. P., and Park, C., "Operating characteristics of a 60-and 10-cm electric arc-driven shock tube. I-The driver. II-The driven section," *Journal of Thermophysics and Heat Transfer*, Vol. 4, No. 3, 1990, pp. 259–265. doi:10.2514/3.175.

[30] Sharma, S. P., and Park, C., "Operating Characteristics of a 60-and 10-cm Electric Arc-Driven Shock Tube-Part 11: The Driven Section," *Journal of thermophysics and heat transfer*, Vol. 4, No. 3, 1990, pp. 266–272. doi:10.2514/3.56243.

[31] Chien, K.-Y., and Compton, D. L., "Radiative cooling of shock-heated air in cylindrical shock tubes," *AIAA Journal*, Vol. 8, No. 10, 1970, pp. 1896–1898. doi:10.2514/3.6017.

[32] Cruden, B. A., "Electron Density Measurement in Reentry Shocks for Lunar Return," *Journal of Thermophysics and Heat Transfer*, Vol. 26, No. 2, June 2012. doi:10.2514/1.T3796.

[33] Brandis, A. M., Johnston, C. O., Cruden, B. A., and Prabhu, D., "Validation of High Speed Earth Atmospheric Entry Radiative Heating from 9.5 to 15.5 km/s," *AIAA Paper*, June 2012. doi:10.2514/6.2012-2865.

[34] Kitamura, K., and Shima, E., "Towards Shock-Stable and Accurate Hypersonic Heating Computations: A New Pressure Flux for AUSM-Family schemes," *Journal of Computational Physics*, Vol. 245, 2013, pp. 62–83. doi:10.1016/j.jcp.2013.02.046.

[35] Kitamura, K., Shima, E., Nakamura, Y., and Roe, P. L., "Evaluation of Euler Fluxes for Hypersonic Heating Computations," *AIAA Journal*, Vol. 48, No. 4, 2010, pp. 763–776. doi:10.2514/1.41605.

[36] Liou, M. S., and Steffen, C., "A New Flux Splitting Scheme," *Journal of Computational Physics*, Vol. 107, 1993, pp. 23–39. doi:10.1006/jcph.1993.1122.

[37] Wada, Y., and Liou, M.-S., "A flux splitting scheme with high-resolution and robustness for discontinuities," *32nd Aerospace Sciences Meeting and Exhibit*, 1994, p. 83. doi:10.2514/6.1994-83.

[38] Liou, M.-S., "Open Issues in Numerical Fluxes: Proposed Resolutions," *20th AIAA Computational Fluid Dynamics Conference*, 2011, p. 3055. doi:10.2514/6.2011-3055.

[39] MacCormack, R. W., "Carbuncle computational fluid dynamics problem for blunt-body flows," *Journal of Aerospace Information Systems*, Vol. 10, No. 5, 2013, pp. 229–239. doi:10.2514/1.53684.

[40] McCorkle, E. R., Hassan, H. A., Cruden, B. A., and Barnhardt, M. D., "Role of Viscous Effects on NEQAIR Predictions of EAST Measurements," *AIAA Paper*, Jan. 2010. doi:10.2514/6.2010-236.

[41] Wright, M. J., Candler, G. V., and Bose, D., "Data-Parallel Line Relaxation method for the Navier-Stokes equations," *AIAA Journal*, Vol. 36, No. 9, Sept. 1998. doi:10.2514/2.586.

[42] Yee, H. C., Kotov, D. V., Wang, W., and Shu, C. W., "Spurious Behaviour of Shock-Capturing Methods by the Fractional-step Approach: Problems Containing Stiff Source Terms and Discontinuities," *Journal of Computational Physics*, 2013. doi:10.1016/j.jcp.2013.01.028.

[43] Kotov, D. V., Yee, H. C., Wang, W., and Shu, C. W., "On Spurious Numerics in Solving Reactive Equations," *NASA Publications*, 2012. URL `http://digitalcommons.unl.edu/nasapub/247`.

[44] Kotov, D. V., Yee, H. C., Panesi, M., Prabhu, D. K., and Wray, A. A., "Computational Challenges for Simulation related to the NASA Electric Arc Shock Tube (EAST) Experiments," *Journal of Computational Physics*, Vol. 269, Jul. 2014, pp. 215–233. doi:10.1016/j.jcp.2014.03.021.

[45] Higdon, K., Goldstein, D., and Varghese, P., "DSMC simulation of a radiating hypersonic flow," *AIP Conference Proceedings*, Vol. 2132, AIP Publishing, 2019, p. 070014. doi:10.1063/1.5119568.

[46] Bensassi, K., and Brandis, A. M., "Time Accurate Simulation of Nonequilibrium Flow inside the NASA Ames Electric Arc Shock Tube," *AIAA Paper*, January 2019. doi:10.2514/6.2019-0798.

[47] Lani, A., Villedieu, N., Bensassi, K., Koloszar, L., Panesi, M., and Yalim, M. S., "COOLFluiD: an open computational platform for multi-physics simulation." 2013. doi:10.2514/6.2013-2589.

[48] Gupta, R. N., Yos, J. M., Thompson, R. A., and Lee, K.-P., "A Review of Reaction Rates and Thermodynamic and Transport Properties for an 11-Species Air Model for Chemical and Thermal Nonequilibrium Calculations to 30,000K," Tech. rep., NASA RP-1232, 08 1990. URL `https://ntrs.nasa.gov/archive/nasa/casi.ntrs.nasa.gov/19900017748.pdf`.

[49] Ramshaw, J. D., "Self-Consistent Effective Binary Diffusion in Multicomponent Gas Mixtures," *Journal of Non-Equilibrium Thermodynamics*, Vol. 15, No. 3, 1990, pp. 295–300. doi:10.1515/jnet.1990.15.3.295.

[50] Huo, W. M., "Electron-Impact Excitation and Ionization in Air," *AIAA Paper*, Jan. 2008. doi:10.2514/6.2008-1207.

[51] Panesi, M., and Lani, A., "Collisional radiative coarse-grain model for ionization in air," *Physics of Fluids*, Vol. 25, No. 5, 2013, p. 057101. doi:10.1063/1.4804388.

[52] Niu, Q., Yuan, Z., Dong, S., and Tan, H., "Assessment of nonequilibrium air-chemistry models on species formation in hypersonic shock layer," *International Journal of Heat and Mass Transfer*, Vol. 127, 2018, pp. 703–716. doi:10.1016/j.ijheatmasstransfer.2018.07.007.

[53] Singh, N., and Schwartzentruber, T., "Nonequilibrium internal energy distributions during dissociation," *Proceedings of the National Academy of Sciences*, Vol. 115, No. 1, 2018, pp. 47–52.

[54] Chaudhry, R. S., Bender, J. D., Schwartzentruber, T. E., and Candler, G. V., "Quasiclassical Trajectory Analysis of Nitrogen for High-Temperature Chemical Kinetics," *AIAA Journal of Thermophysics and Heat Transfer*, Vol. 32, No. 4, 2018, pp. 833–845. doi:10.2514/1.T5484.

[55] Gimelshein, S. F., and Wysong, I. J., "Nonequilibrium air flow predictions with a high-fidelity direct simulation Monte Carlo approach," *Physical Review Fluids*, Vol. 4, No. 3, 2019, p. 033405. doi:10.1103/PhysRevFluids.4.033405.

[56] Sharma Priyadarshini, M., Munafo, A., Brandis, A. M., Cruden, B. A., and Panesi, M., "One-dimensional modeling methodology for shock tubes: Application to the EAST facility," *2018 Joint Thermophysics and Heat Transfer Conference*, 2018, p. 4181. doi:10.2514/6.2018-4181.

[57] Nompelis, I., Drayna, T. W., and Candler, G. V., "A Parallel Unstructured Implicit Solver for Hypersonic Reacting Flow Simulation," *AIAA Paper*, June 2005. doi:10.2514/6.2005-4867.

[58] Nompelis, I., Wan, T., and Candler, G. V., "Performance Comparisons of Parallel Implicit Solvers for Hypersonic Flow Computations on Unstructured Meshes," *AIAA Paper*, June 2007. doi:10.2514/6.2007-4334.

[59] Nompelis, I., Bender, J. D., and Candler, G. V., "Implementation and Comparisons of Parallel Implicit Solvers for Hypersonic Flow Computations on Unstructured Meshes," *AIAA Paper*, June 2011. doi:10.2514/6.2011-3547.

[60] Park, C., "Review of Finite-Rate Chemistry Models for Air Dissociation and Ionization," *Molecular Physics and Hypersonic Flows*, NATO ASI Series (Series C: Mathematical and Physical Sciences), Vol. 482, edited by M. Capitelli, Kluwer Academic Publishers, Dordrecht, 1996, pp. 581–596. doi:10.1007/978-94-009-0267-1_39.

[61] Cruden, B. A., and Brandis, A. M., "Analysis of Shockwave Radiation Data in Nitrogen," *AIAA Aviation 2019 Forum*, 2019, p. 3359. doi:10.2514/6.2019-3359.

[62] Gnoffo, P. A., Gupta, R. N., and Shinn, J. L., "Conservation Equations and Physical Models for Hypersonic Air Flows in Thermal and Chemical Nonequilibrium," *NASA TP-2867*, 1989. URL `https://ntrs.nasa.gov/archive/nasa/casi.ntrs.nasa.gov/19890006744.pdf`.

[63] Gordon, S., and McBride, B. J., "Computer Program for Calculations of Complex Chemical Equilibrium Compositions and Applications: I, Analysis," Tech. rep., NASA RP-1311, 10 1994. URL `https://ntrs.nasa.gov/archive/nasa/casi.ntrs.nasa.gov/19950013764.pdf`.

[64] McBride, B. J., and Gordon, S., "Computer Program for Calculation of Complex Chemical Equilibrium Compositions and Applications, 2. Users Manual and Program Description," Tech. Rep. RP-1331-2, NASA, June 1996. URL `https://www.grc.nasa.gov/WWW/CEAWeb/RP-1311-P2.pdf`.

[65] Huo, W. M., Liu, Y., Panesi, M., Munafo, A., Wray, A. A., and Carbon, D. F., "Electron-Impact Excitation Cross Sections for Modeling Non-Equilibrium Gas," *AIAA Paper*, Jan. 2015. doi:10.2514/6.2015-1896.

[66] Steger, J. L., and Warming, R., "Flux vector splitting of the inviscid gasdynamic equations with application to finite-difference methods," *Journal of computational physics*, Vol. 40, No. 2, 1981, pp. 263–293. URL `https://ntrs.nasa.gov/archive/nasa/casi.ntrs.nasa.gov/19790020779.pdf`.

[67] Hirsch, C., *Numerical Computation of Internal and External Flows*, Vol. 2, John Wiley & Sons, Inc., New York, 1990. doi:10.1016/B978-0-7506-6594-0.X5037-1.

[68] Dinzl, D., "Analysis of Stationary Crossflow Instability on HIFiRE-5 Using Direct Numerical Simulation," Ph.D. thesis, University of Minnesota, 2016. doi:http://hdl.handle.net/11299/178967.

[69] Druguet, M. C., Candler, G. V., and Nompelis, I., "Effects of Numerics on Navier-Stokes Computations of Hypersonic Double-Cone Flows," *AIAA Journal*, Vol. 43, No. 3, 2005. doi:10.2514/1.6190.

[70] MacCormack, R. W., "Current Status of Numerical Solutions of the Navier-Stokes Equations," *AIAA Paper*, , No. 1985-32, 1985. doi:10.2514/6.1985-32.

[71] MacCormack, R. W., and Candler, G. V., "The solution of the Navier-Stokes Equations Using Gauss-Siedel Line-Relaxation," *Computers and Fluids*, Vol. 17, No. 1, 1989, pp. 135–150. doi:10.1016/0045-7930(89)90012-1.

[72] Subbareddy, P. K., and Candler, G. V., "A fully discrete, kinetic energy consistent finite-volume scheme for compressible flows," *Journal of Computational Physics*, Vol. 228, No. 5, 2009, pp. 1347–1364. doi:10.1016/j.jcp.2008.10.026.

[73] Wright, M. J., Candler, G. V., and Prompolini, M., "Data-Parallel Lower-Upper Relaxation Method for the Navier-Stokes equations," *AIAA*, Vol. 34, No. 7, 1996. doi:10.2514/3.13242.

[74] Steger, J. L., and Warming, R. F., "Flux vector splitting of the inviscid gas dynamics equations with applications to finite-difference methods," *Journal of Computational Physics*, Vol. 40, 1981, pp. 263–293. doi:10.1016/0021-9991(81)90210-2.

[75] Chandel, D., Nompelis, I., and Candler, G. V., "Computations of High Enthalpy Shock-waves in Electric Arc Shock-Tube (EAST) at NASA Ames," *AIAA Paper*, Jan. 2018. doi:10.2514/6.2018-1722.

[76] Chandel, D., Nompelis, I., and Candler, G. V., "Numerical Simulation of Propagation of Strong Shock Waves," *AIAA Paper*, Jan. 2017. doi:10.2514/6.2017-0744.

Appendix A

Tables

There are total 18 pizoelectric sensors placed along the tube walls to detect the shock. The shock time of arrival data for nitorgen shocks are presented in Table A.1. The values listed from 1.060 m to 6.186 m are the raw time of arrival inferred from the pressure rise detected at respective PCB locations whereas the values quoted at sensor locations from 6.999 m to 7.985 m are based on a quadratic fit on the raw data. This is done to obtain a smooth variation of shock speed within the limits of measurement errors. More details can be found in Brandis and Cruden [1].

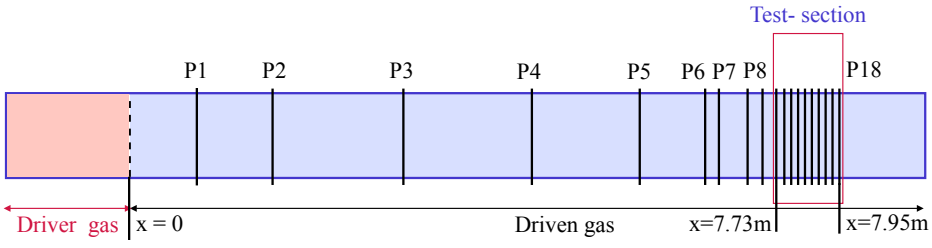

Figure A.1: Pressure sensor locations along EAST shock tube

Table A.1: Shock arrival-times for nitrogen [1]

sensor no.	Distance (m)	Shock arrival-times (μs)			
EAST shot no.→		62-5	62-6	62-16	62-42
Shock speed (km/s) →		**9.63**	**8.7**	**7.7**	**5.94**
P1	1.060	176.5	191.1	217.1	288.9
P2	2.203	268.4	286.9	326.5	430.9
P3	3.748	399.2	426.7	483.4	637.6
P4	4.967	508.9	544.7	617.1	815.2
P5	6.186	624.5	670.8	758.8	1003.5
P6	6.999	704.6	756.8	857.2	1132.4
P7	7.101	714.7	767.7	869.8	1148.8
P8	7.566	761.7	818.7	928.5	1224.9
P9	7.649	770.2	828.0	939.0	1238.6
P10	7.731	778.8	837.3	949.7	1252.4
P11	7.763	782.1	840.9	953.8	1257.7
P12	7.795	785.4	844.5	957.9	1263.0
P13	7.826	788.8	848.1	962.0	1268.3
P14	7.858	792.1	851.7	966.1	1273.6
P15	7.890	795.5	855.4	970.2	1279.0
P16	7.922	798.8	859.0	974.4	1284.3
P17	7.953	802.2	862.7	978.5	1289.7
P18	7.985	805.5	866.3	982.7	1295.0

Table A.2: Reaction rate parameters from Park [2]

Reaction	$A_{f,r}$ (mole/m^3 s)	η	θ (K)	collision partners	T$_a$
$N_2 + M = N + N + M$	7.0E+18	-1.6	113,200	M = N_2, O_2, NO, NO^+, N_2^+, O_2^+	$\sqrt{TT_v}$
$N_2 + M = N + N + M$	3.0E+19	-1.6	113,200	M = N, O, N_+, O_+	$\sqrt{TT_v}$
$N_2 + M = N + N + M$	3.0E+21	-1.6	113,200	M = e^-	$\sqrt{TT_v}$
$O_2 + M = O + O + M$	2.0E+18	-1.5	59,500	M = N_2, O_2, NO, NO^+, N_2^+, O_2^+	$\sqrt{TT_v}$
$O_2 + M = O + O + M$	1.0E+19	-1.5	59,500	M = N, O, N_+, O_+	$\sqrt{TT_v}$
$NO + M = N + O + M$	5.0E+12	0	75,500	M = N_2, O_2, NO, NO^+, N_2^+, O_2^+	$\sqrt{TT_v}$
$NO + M = N + O + M$	1.1E+14	0	75,500	M = N, O, N_+, O_+	$\sqrt{TT_v}$
$N + e^- = N^+ + e^- + e^-$	4.46E+26	-2.64	168,730	based on Huo et al.[65]	$\sqrt{TT_v}$
$O + e^- = O^+ + e^- + e^-$	7.136E+22	-1.88	155,510	based on Huo et al.[65]	$\sqrt{TT_v}$
$N_2 + O = NO + N$	6.4E+14	-1.0	38,400		T
$NO + O = O_2 + N$	8.4E+09	0	19,400		T
$N + O = NO^+ + e^-$	5.3E+09	0	31,900		T
$N + N = N_2^+ + e^-$	2.0E+10	0	67,500		T
$O + O = O_2^+ + e^-$	1.1E+10	0	80,600		T
$O^+ + N_2 = N_2^+ + O$	9.1E+08	0.36	22,800		T
$O^+ + NO = N^+ + O_2$	1.4E+02	1.9	15,300		T
$NO^+ + O_2 = O_2^+ + NO$	2.4E+10	0.41	32,600		T
$NO^+ + N = N_2^+ + O$	7.2E+10	0	35,500		T
$NO^+ + O = N^+ + O_2$	1.0E+09	0.5	77,200		T
$O_2^+ + N = N^+ + O_2$	8.7E+10	0.14	28,600		T
$O_2^+ + N_2 = N_2^+ + O_2$	9.9E+09	0	40,700		T
$NO^+ + N = O^+ + N_2$	3.4E+10	-1.08	12,800		T
$NO^+ + O = O_2^+ + N$	7.2E+09	0.29	48,600		T